symmetry

IMPACT FACTOR 2.2

CITESCORE 5.4

Article

Nuclear-Spin-Dependent Chirogenesis: Hidden Symmetry Breaking of Poly(di-*n*-butylsilane) in *n*-Alkanes

Michiya Fujiki, Takashi Mori, Julian R. Koe and Mohamed Mehawed Abdellatif

Special Issue

Chemistry: Symmetry/Asymmetry—Feature Papers and Reviews

Edited by

Prof. Dr. György Keglevich

MDPI

https://doi.org/10.3390/sym17030433

symmetry

MDPI

Article

Nuclear-Spin-Dependent Chirogenesis: Hidden Symmetry Breaking of Poly(di-*n*-butylsilane) in *n*-Alkanes

Michiya Fujiki [1,*], Takashi Mori [1], Julian R. Koe [2] and Mohamed Mehawed Abdellatif [3,4]

[1] Graduate School of Advanced Science and Technology, Nara Institute of Science and Technology (NAIST), 8916-5 Takayama, Ikoma 630-0192, Nara, Japan; mori.takashi02@ms.naist.jp
[2] Department of Natural Sciences, International Christian University (ICU), 3-10-2 Osawa, Mitaka 181-8585, Tokyo, Japan; koe@icu.ac.jp
[3] Department of Chemistry, Graduate School of Science, Tokyo Metropolitan University (TMU), 1-1 Minami-Osawa, Hachioji 192-0397, Tokyo, Japan; mohamed-soliman@tmu.ac.jp
[4] Chemistry of Tanning Materials and Leather Technology Department, Chemical Industries Research Institute, National Research Centre (NRC), 33 El Buhouth St., Dokki, Giza 12622, BP, Egypt
* Correspondence: fujiki.michiya@naist.ac.jp

Abstract: Since the 1960s, theorists have claimed that the electroweak force, which unifies parity-conserving electromagnetic and parity-violating weak nuclear forces, induces tiny parity-violating energy differences (10^{-10}–10^{-21} eV) between mirror-image molecules. This study reports the dual mirror-symmetry-breaking and second-order phase transition characteristics of mirror-symmetric 7_3-helical poly(di-*n*-butylsilane) in *n*-alkanes under static (non-stirring) conditions. In particular, *n*-dodecane-h_{26} significantly enhances the circular dichroism (CD) and circularly polarized luminescence (CPL) spectra. A new (−)-CD band emerges at 299 nm below T_{C1} ~ 105 °C, with a helix–helix transition at T_{C2} ~ 28 °C, and exhibits g_{abs} = +1.3 × 10^{-2} at −10 °C. Synchronously, the CPL band at 340 nm exhibiting g_{lum} = −0.7 × 10^{-2} at 60 °C inverts to g_{lum} = +2.0 × 10^{-2} at 0 °C. Interestingly, clockwise and counterclockwise stirring of the mixture induced non-mirror-image CD spectra. *n*-Dodecane-d_{26} weakens the g_{abs} values by an order of magnitude, and oppositely signed CD and a lower T_{C1} of ~45 °C are observed. The notable H/D isotope effect suggests that the CH_3 termini of the polysilane and *n*-dodecane-h_{26}, which comprise a three identical nuclear spin-1/2 system in a triple-well potential, effectively work as unidirectional hindered rotors due to the handedness of nuclear-spin-dependent parity-violating universal forces. This is supported by the (−)-sign vibrational CD bands in the symmetric and asymmetric bending modes of the CH_3 group in *n*-dodecane-h_{26}.

Keywords: parity violation; triple-well potential; circular dichroism; circularly polarized luminescence; Salam's hypothesis; phase transition; tunneling; isotope effect; hindered rotor; superposition

Academic Editor: György Keglevich

Received: 3 February 2025
Revised: 3 March 2025
Accepted: 5 March 2025
Published: 13 March 2025

Citation: Fujiki, M.; Mori, T.; Koe, J.R.; Abdellatif, M.M. Nuclear-Spin-Dependent Chirogenesis: Hidden Symmetry Breaking of Poly(di-*n*-butylsilane) in *n*-Alkanes. *Symmetry* **2025**, *17*, 433. https://doi.org/10.3390/sym17030433

1. Introduction

1.1. Hierarchy in Broken Symmetries

All hierarchical structures of nature are governed by four fundamental physical forces: the infinite range gravitational force (GF), the infinite range electromagnetic force (EMF), the ultrashort range (~10^{-9} nm) weak nuclear force (WF), and the ultrashort range (~10^{-6} nm) strong nuclear force (SF) [1–33]. Relative to the SF, the magnitudes of the GF, EMF, and WF are 10^{-43}, 10^{-2}, and 10^{-6}, respectively [9,31]. The four forces are mediated by force-carrying vectoral bosons with integer spins: GF: the hypothetical massless graviton *G* (spin-2);

WF: the massive charged $W^{\pm}$ (spin-1, 80.4 GeV) and neutral Z^0 bosons (spin-1, 91.2 GeV); EMF: the massless photon γ (spin-1); and SF: the massless eight gluons (spin-1) [31–33]. Aiming at a deeper understanding of hierarchical structures, it has been theoretically and experimentally investigated whether the seven symmetries—parity (*P*), charge conjugation (*C*), time reversal (*T*), and their combinations, *CP*, *PT*, *CT*, and *CPT*—are rigorously conserved in the four forces [1–27,31–33]. *P*- and *CP*-symmetry breaking has been investigated in particle (neutrinos) and subatomic (*K*- and *B*-mesons) physics. *P*-symmetry breaking has been established in nuclear and atomic physics but not in chemistry, bioscience, or materials science.

Recently, *P*-symmetry breaking became a hot topic in cosmology [24–30]. In 2020, astrophysicists reported hidden handedness imprinted in the cosmic microwave background (CMB) at 2.73 K. The sign and magnitude of the birefringent rotation from an observer were evaluated to be $\beta_{\mathrm{CMB}} = +0.35 \pm 0.14^{\circ}$ [28,29], corresponding to a Kuhn dissymmetry ratio, g_{em} of +2.0 ($\pm$0.8) $\times$ 10^{-3}. Our life, biomolecules, biopolymers, and chemical reactions may thus experience a cosmological dextrorotatory force ranging from 0.3 to 630 GHz (0.01–21 cm^{-1}) with a peak of 160 GHz (5.35 cm^{-1}). The $W^{\pm}$ bosons carry the handedness of the weak charged current (WCC) and permit exchange between quarks (fermions with spin-1/2), i.e., left-hand (LH) up quark (*u*, 2.2 MeV, charge +2/3) and LH down quark (*d*, 4.7 MeV, charge $-1/3$). However, interaction with right-hand (RH) *u* and RH *d* is not permitted [9,31–33]. Likewise, W^+ and W^-, respectively, transform between leptons (spin-1/2) from LH electron (e^-, 0.51 MeV, charge -1) to LH electron-neutrino ($\nu_{\mathrm{e}} < 2.2 \times 10^{-6}$ MeV, charge 0) and from LH ν_{e} to LH e^- [9,31,32]. The W^--WCC in $^{60}\mathrm{Co} \rightarrow {}^{60}\mathrm{Ni}$ and W^+-WCC in $^{58}\mathrm{Co} \rightarrow {}^{58}\mathrm{Fe}$ nuclear fissions [4,5,33], as well as other $\beta^{\mp}$ decays of radiomarkers, i.e., $^{11}\mathrm{C}$, $^{13}\mathrm{N}$, $^{15}\mathrm{O}$, $^{18}\mathrm{F}$, $^{32}\mathrm{P}$, are detectable as the opposite handedness of e^- and its anti-matter positron, e^+ [33,34].

1.2. Atomic Parity Violation—Theories and Experiments

Inspired by parity-violation (*PV*) in the $\beta^{\mp}$-decays [33], Weinberg, Glashow, and Salam in the 1960s proposed electroweak force (EWF) theory involving the Z^0 boson to unify *PV*-WF and *P*-symmetry conserving (*PC*)-EMF. The EWF theory makes all of Z^0, $W^{\pm}$, and γ possible in a massless family above ~10^2 GeV (~10^{15} K) [31,32]. In 1973, the detection of weak neutral current (WNC) and WCC by an elastic ν_e–anti-ν_e scattering using a liquid bubble chamber detector (called Gargamelle) filled with CF_3Br (possibly, $C^{19}F_3{}^{79/81}Br$) at Conseil Européen pour la Recherche Nucléaire (CERN) was reported, followed by, in 1983, the detection of the Z^0 as a production of an e^-e^+ pair using the proton (*p*)-anti-*p* collider (Super Proton Synchrotron, SPS) at CERN [35–39]. By combining the SF theory and the Higgs scalar boson (spin-0, 125.1 GeV), the EWF theory became the standard model of particle physics [31,32]. Also, around that time, theorists further hypothesized atomic parity violation (APV) and molecular parity violation (MPV) induced by the handedness of the WNC mediated by the Z^0-boson. Probing the APV hypothesis of stable atoms met difficulties due to the absence of chemical chirality [40–61]. Although the APV of $^1\mathrm{H}$ was computationally visualized as a handed spiral torus of e^- trajectory around *p* by admixing *P*-even 2*s* and *P*-odd $2p_{1/2}$ states, its APV magnitude was far from a detectable level [50]. Theoretical predictions to amplify APV $\propto Z^3$ (*Z*: atomic number) for non-relativistic atoms and APV $\propto Z^5$ for relativistic atoms [46–49] led to the successful detection of weak APV effects on the order of $g \sim 10^{-7}$ at forbidden electronic transitions for several high-*Z* atoms, including $^{133}\mathrm{Cs}$, $^{209}\mathrm{Bi}$, $^{208}\mathrm{Pb}$, $^{205}\mathrm{Tl}$, and $^{174}\mathrm{Yb}$, in a collision-free gas state using high-resolution optical rotatory dispersion spectroscopy (ORD), fluorescence-detective circular dichroism spectroscopy, and dc-Stark interferometer [9,49,51–55].

In 1964 Michel [43], followed by Stodolsky in 1974 and 1982 [44,45], predicted the use of neutron optical activity to detect APV effects. Actually, in recent years, spin-polarized neutron resonance scattering (SPNRS) has been used experimentally and detected clear APV effects. Almost a dozen half-integer nuclear spin (HINS) high-*Z* isotopes (spin number, *I*) as solids, i.e., ^{81}Br ($I = 3/2$), ^{93}Nb ($I = 9/2$), ^{103}Rh ($I = 7/2$), ^{105}Pd ($I = 5/2$), ^{107}Ag ($I = 1/2$), ^{111}Cd ($I = 1/2$), ^{115}In ($I = 9/2$), ^{117}Sn ($I = 1/2$), ^{127}I ($I = 5/2$), ^{139}La ($I = 7/2$), and integer nuclear spin (INS) radioisotope, ^{238}U ($I = 0$), revealed huge APV effects on the order of $g \sim 10^{-3}$–10^{-2} at resonance transitions by SPNRS experiments in the energy range of 0.5 to 1100 eV [56–61]. Among these HINS isotopes, ^{139}La shows a particularly large g value of $\sim 2 \times 10^{-1}$ at 0.734 eV [58]. On the other hand, the INS isotopes, i.e., ^{82}Br ($I = 5$), ^{112}Cd ($I = 0$), ^{118}Sn ($I = 0$), ^{140}La ($I = 3$), showed greatly reduced APV effects even by the SPNRS [56,57]. These experiments strongly indicate the importance of HINS isotopes at the resonant transitions, enabling great amplification of APV effects, which is presumably also applicable to the nuclear-spin-dependent and/or the nuclear-spin-induced MPV effects.

1.3. Molecular Parity Violation—Theories and Experiments

In the 1960s and 1970s, MPV theorists estimated the order of magnitude of the parity-violating energy difference (PVED) between mirror-image molecules due to handed electron–nuclei interactions by admixing Z^0-WNC to *PC*-EMF [62–68]. Comprehensive reviews covering those experiments, including the self-disproportionation of enantiomers (known as SDE), were published [69]. From the 1980s onward [4–8,10,16–20,68,70–90], sophisticated theories of electroweak quantum chemistry facilitated the rigorous prediction of the sign and magnitude of PVED for mirror-image molecules in mostly double-well potential (DWP) with rotational and/or inversion barriers (E_B). Because of the *P*-odd characteristics in the DWP, the potential energy for one mirror-image molecule is raised by E_{PV}; conversely, the other is pushed down by E_{PV}, similar to a seesaw. Therefore, the PVED is equal to $2E_{PV} = +E_{PV} - (-E_{PV})$. The magnitude of PVED for isolated molecules, however, is too small to detect, being on the order of 10^{-10}–10^{-21} eV (cf. 0.026 eV at 300 K), corresponding to 10^{-6}–10^{-17} cm^{-1} and 10^{4}–10^{-7} Hz [18,19,84–88].

The MPV hypothesis is in sharp contrast to the accepted concepts of enantiomerism, diastereomerism, and racemism in modern stereochemistry based on *PC*-EMF theory [91–94]. Conventional stereochemical theory is predicated upon the rigorous preservation of energetic equality between mirror-image molecules, supramolecules, macromolecules, micelles, colloids, aggregates, gels, liquid crystals, and crystals. Chiroptical spectroscopic techniques [91–94], including electronic circular dichroism (CD), vibrational circular dichroism (VCD), Raman optical activity (ROA), and ORD, which detect the ground state chirality, and circularly polarized luminescence (CPL) to measure photoexcited chirality should therefore afford absolutely ideal mirror-image chiroptical spectra between the mirror-image substances, exhibiting identical magnitudes with opposite chiroptical signs at the same wavelengths and wavenumbers to at least three significant figures. A few researchers appear to be aware that the experimental results do not rigorously obey conventional stereochemical theory, as evidenced by differences in the chiroptical spectra, physicochemical properties, chemical reactions, and other aspects between supposed mirror-image molecules, oligomers, polymers, colloids, and crystals, as discussed in Section 3.9 [12,21–24,66,69,78,89,90,95–115].

Detecting MPV effects is therefore important in elucidating the missing link between the handedness of matter at all hierarchical levels of the matter world and the anti-matter world, ranging from LH-ν_e, LH-quarks, APV, L-amino acids and proteins, D-ribose and DNA/RNA, artificial molecules, and macromolecules; the homochiral living world, including helical bacteria, plants, and seashells; and the cosmological dextrorota-

tory rotation [1,3,8,12,13,18–33,49,55,60,62,70–72,74,82,86,95–115]. Aiming at amplifying the tiny PVED to detectable levels, six theoretical scenarios have so far been proposed, as described below.

- Scenario A. An accumulation model, often called a linear amplification model, was proposed in 1966 by Yamagata [62]. The overall PVED is proportional to repeat unit number (N), yielding $N \times E_{PV}$ in the systems. The idea is applicable to N-mer systems, i.e., macromolecules, supramolecules, micelles, colloids, micelles, colloids, aggregates, molecular liquids, liquid crystals, and crystals [12,66,71,78,95–106].
- Scenario B. $E_{PV} \propto Z^5$ is possible for high-Z atoms, while Z^2 and Z^3, respectively, arise from spin-orbit-coupling (SOC, ξ) of constituents and the PV-WNC [5,6,67,70,73,75], which is similar to the Z^3- and Z^5-dependence of APV [42,46–49]. The idea is applicable to experiments using molecules involving high-Z atoms such as I, W, Re, Pb, Ir, Ru, and Os in periods 5 and 6 [17,18,69,73,75–79,95].
- Scenario C. In the early 1990s, a nonlinearly amplified MPV theory in a condensed phase was hypothesized by Salam based on Cooper $e^-(\uparrow)$-$e^-(\downarrow)$ pairs (I = 0) in the Bardeen–Cooper–Schrieffer (BCS) theory of superconductivity and the ^{3}He($\uparrow$)-^{3}He($\uparrow$) pair (I = 1) and Bose–Einstein condensate (BEC) theory of superfluidity [107,108]. The hypothesis predicts that an L–D mixture of amino acids transforms into a single enantiomer at a critical temperature (T_c) by cooperative e^-–n interactions. This cooperativity results in an entropy-driven, second-order phase transition detectable by emerging chiroptical signals and a jump of specific heat capacity [107,110–112]. Although $T_c \sim 2.7$ K was numerically obtained, a higher $T_c \sim 250$ K is optimistically conceivable [107]. However, because the rigid configuration of D-α-amino acids is unable to invert to L-configurations [96,97], non-rigid molecular rotamers in the absence of point chirality are suitable to validate the MPV hypothesis [18,19,67,109–115]. Similar phase transition models including mirror symmetric and dissymmetric bifurcations were proposed by Goldanskii et al. [2,3]. The selection between LH and RH at the bifurcation point is hypersensitive to external and internal fluctuations relative to the advantageous factors (rate constants in asymmetric chemical reactions) of chemical and physical chirality.
- Scenario D. The interplay between a smaller quantum tunneling splitting with an opposite parity, $\Delta E_{\pm}$, in a DWP with a larger E_B and tiny P-odd E_{PV} leads to the resonant amplification of the MPV effect when satisfying $\Delta E_{\pm} \sim E_{PV}$. In the cases where $E_{PV} \ll \Delta E_{\pm}$ or $E_{PV} \gg \Delta E_{\pm}$, there is no detectable amplification [16–19,67,80,81,84–88]. Modulating the E_B vs. $\Delta E_{\pm}$, kT, and E_{PV} causes a significant transition from coherence (oscillation) to decoherence (non-oscillation) due to environmental effects, leading to detectable MPV effects using steady-state and time-resolved chiroptical spectroscopy in a condensed phase [21–24,67,80,81,84–88,106,113–115].
- Scenario E. $E_{PV} \propto (E_0 - E_T)^{-1} = \Delta E_{ST}$, where E_0 and E_T are the ground singlet (S_0) and photoexcited triplet (T_1) states [5,6], respectively, as confirmed by the direct $S_0 \rightarrow T_1$ and $T_1 \rightarrow S_0$ transition [116,117]. ΔE_{ST} is the difference in energy between the first excited (S_1) and T_1 states. Although the ^{1}H atom has the weakest ξ of 0.45 cm^{-1} (5.5×10^{-5} eV, 1.3×10^{-3} kcal mol^{-1}), several light- and medium-Z number atoms have significant ξ in cm^{-1}: e.g., C (29), N (42), O (57), F (75), Si (211), P (247), S (288), Ge (1450), and Sn (4090) [118]. Molecules and polymers containing larger ξ atoms were found suitable for testing the MPV hypothesis. In particular, chain-like polysilanes consisting of Si–Si main chains with organic pendant side chains are one of the best candidates because summing up the SOCs amplifies the ξ of Si (211 cm^{-1}) $\times$ N-mer (Scenario A). This ξ can be further enhanced by HINS ^{29}Si (I = 1/2, natural abundance 4.7%, negative value of nuclear magnetic moment, $\mu_N = -0.55$) [119]. For comparison,

^{13}C (I = 1/2, natural abundance 1.1%, μ_N = +0.70), ^{1}H (I = 1/2, natural abundance 99.99%, μ_N = +2.79), and ^{2}H (I = 1, μ_N = +0.86), respectively, have positive values of μ_N. The sign and magnitude of μ_N and I should contribute differently to the observable MPV effects.

- Scenario F. Most APV and MPV theories neglect the contribution of the nuclear spins, although advanced APV and MPV theories involving the nuclear spin effect have also been proposed. The anapole moment (AM) of the HINS ^{1}H atom was hypothesized in the late 1950s by Zel'dovich to account for *PV* $\beta^{\pm}$-decays [40–42]. The first *PV* molecular anapole moment (MAM) of diatomic molecules was theoretically discussed in the 1980s by Flambaun and Khriplovich, who suggested that the *PV*-MAM may be detectable by optical activity [120–124]. In 1997, the first *PV* atomic anapole moment (AAM) of ^{133}Cs vapor was detected using the dc-Stark technique [125,126]. So far, several hypothetical and realistic molecules and nanostructures [120–146], e.g., organometallic molecules involving ^{195}Pt and ^{207}Pb, [127] M^{19}F (M = $^{203/205}$Tl, ^{38}Ba, ^{223}Ra) [121–123,128–130], ^{9}Be(NC)$_2$ and ^{25}Mg(NC)$_2$ [131], H_2X_2 (X = ^{17}O, ^{33}S, ^{77}Se, ^{125}Te, ^{209}Po) [132–134], chiral fluorooxirane and CHFClBr [135–137], and others [89,90,138–146] have been theoretically and experimentally investigated. The simplest experiment to validate nuclear-spin-dependent MPV and MAM is to compare HINS and INS isotopomers, that is, ordinary organic substances and their fully or partly deuterated analogs.

For almost 130 years, starting with Kipping and Pope in 1897 and 1898 [147,148], the chiroptical and physicochemical properties and solid-state structures of LH and RH molecules in crystals, biological oligomers, micelles, aggregates, synthetic polymers, and systems have been investigated and statistical analyses carried out [21–24,69,78,95–106,109–115,148]. However, most of these experimental results, including our previous polysilanes bearing (*S*)- and (*R*)-3,7-dimethyloctyl pendants with 96% *ee* [21–24] and (*S*)- and (*R*)-2-methylbutyl pendants with 99% *ee* (Scenarios A, B, C, and E) [24,106], remain a matter of debate because of non-100% *ee* sources, unresolved impurities and chiral dust, differences in the crystal sizes and molecular weights of polymers, the action of directionally opposite Coriolis forces in the northern and southern hemispheres, and non-natural materials.

Recently, the present authors reported clear MPV-related (−)-sign CPL spectra (g_{lum} ~ –2 × 10^{-3}) at 25 °C from nearly 70 kinds of mirror-symmetric π-conjugated molecular rotamers without point chirality in achiral solvents under static conditions (Scenarios A, C, and D) [113–115]. The rotamers possess small hindered barriers of E_B ~ 1 kcal mol^{-1} along the C–C, C–N, C–O, and C–S single bonds (for example, refs. [113–115] Aiming at approaching the condition $\Delta E_{\pm} \sim E_{PV}$, it was effectively possible to increase E_B [113] by increasing the viscosity of the solvents (an environmental effect). The (−)-sign CPL spectra result from the S_1-state of metastable chiral rotamers with handedness. Among these rotamers, two pyrromethenes, 546 and 597, carrying multiple methyl groups as hindered rotors (Chart S1, Supplementary Materials (SM)), coumarin 6, coumarin 545, and rhodamine B revealed clear (−)-CD spectra ($g_{abs} \sim -10^{-5}$) [114]. Additionally, Fujiki, Imai, and coworkers reported that a HINS molecular system, $^{151/153}$Eu(β-diketonate)$_3$, involving six C$^{19}F_3$ groups coordinated with ^{31}P-containing enantiomeric ligands, reveals *P*-odd (−)-sign CPL spectra at $^{5}D_0 \rightarrow {}^{4}F_J$ (J = 3 at 650 nm and J = 4 at 700 nm) transitions [149]. This suggests nuclear-spin-induced MPV and/or *PV*-MAM effects (Scenario F) [150,151].

1.4. Our Experimental Approaches Toward Validation of Molecular Parity Violation Hypothesis

With the above six MPV scenarios in mind, our findings stimulated us to experimentally investigate the variable temperature (VT) CD and CPL spectral characteristics of rigid rod-like poly(di-*n*-butylsilane) (PDBS, Chart S1, Supplementary Materials) having

a large characteristic ratio, C_∞ = 42.3, in *n*-hexane (Θ solvent) at 19.1 °C, to validate the MPV hypothesis [152,153]. PDBS is well-known to adopt mirror-symmetric 7_3-helices with λ_{max} = 319 nm in *n*-hexane and at λ_{max} 313–320 nm in the solid state, although it possesses no chiral centers [152–156]. The family of poly(dialkylsilane)s including PDBS are acknowledged to be excellent examples of helical polymers because they exhibit narrow phonon-side-band-free absorption and photoluminescence (PL) in the near-UV region and show quasi-one-dimensional Wannier-like exciton behavior, characteristic of a Si quantum wire [157–163]. The nature of the exciton is extremely sensitive to the helicity of the wire [152–168].

The present study focuses on PDBS in medium-length *n*-alkane solvents using VT CD/UV and CPL/PL spectroscopy, ranging from −10 °C to 110 °C. Herein, we report the dual mirror-symmetry breaking second-order phase transitions (chiroptical generation and chiroptical inversion) of PDBS in a range of longer chain solvents: *n*-$C_{11}H_{24}$, *n*-$C_{12}H_{26}$, *n*-$C_{13}H_{28}$, *n*-$C_{14}H_{30}$, and *n*-$C_{16}H_{34}$ under static conditions. Similar, though less obvious, effects were found in shorter chain solvents: *n*-C_8H_{18}, *n*-$C_{10}H_{22}$, and isooctane. In particular, very large amplitude effects in the CD and CPL spectra of PDBS were induced in *n*-$C_{12}H_{26}$. A new (−)-sign CD band emerges at λ_{max} 300 nm below T_{C1} ~ 105 °C, followed by a switch from (−)- to (+)-sign CD bands due to a helix–helix transition at T_{C2} ~ 28 °C, reaching g_{abs} = +1.3 × 10^{-2} at −10 °C. Synchronously, the (−)-sign CPL band at 60 °C exhibited g_{lum} = –0.7 × 10^{-2} at λ_{em} 340 nm and inverted to (+)-sign CPL with g_{lum} = +2.0 × 10^{-2} at 0 °C. The signs and magnitudes of g_{lum} at T_{C2} show a large fluctuation between +2.0 × 10^{-2} and −1.0 × 10^{-2}. Notably, in *n*-$C_{12}D_{26}$, these g_{abs} values were an order of magnitude weaker, with opposite CD signs and a lower T_{C1} of ~45 °C. Unexpectedly, clockwise (CW) and counterclockwise (CCW) stirring of PDBS in *n*-alkanes at 0, 20, and 40 °C did not result in mirror-image CD spectra. The notable H/D isotope effect allows us to propose that the three-fold symmetric CH_3 group, which is representative of three identical HINS systems (I = 3/2 (A) and 1/2 (E_a and E_b)) in a triple-well potential (TWP), works as a unidirectional hindered rotor, supporting several (−)-sign vibrational CD bands: symmetric bending (umbrella) at 1382 cm^{-1}, asymmetric bending at 1455 cm^{-1}, and other vibrational modes.

2. Results

2.1. Protocols for Reproducible Chiroptical Measurements of MPV Effects

To arrive at several protocols for testing for MPV effects, PDBS-H and PDBS-L were examined as homogeneous solutions in several *n*-alkanes and isooctane. The synthesis and characterization of PDBS–H and –L were reported in Section S2 and Figures S1 and S2 in the Supplementary Materials. PDBS-H has a higher number-average molecular weight (M_n) and weight-average molecular weight (M_w), and PDBS-L has lower M_n and M_w, while both have a similar polydispersity index (*PDI*): PDBS-H; M_n = 6.15 × 10^4, M_w = 11.6 × 10^4, *PDI* = 1.89 and PDBS-L; M_n = 4.55 × 10^4, M_w = 8.28 × 10^4, *PDI* = 1.82.

Furthermore, to validate a generality of MPV effects, poly{bis-(*p*-*t*-butylphenyl)silane), poly(*n*-hexyl-2-ethylbutylsilane), poly(methyl-*n*-propylsilane), poly(*n*-pentyl-*n*-propylsilane), poly(di-*n*-pentylsilane), poly(di-*n*-hexylsilane), and permethyldecasilane were examined (Chart S1, Supplementary Materials). The synthesis and characterization of the oligo- and polysilanes were mentioned in Section S2.4 and Figures S3 and S4 (Supplementary Materials). The MPV testing results are discussed in Section 3.8.

A prolonged search was carried out for a suitable system providing reproducible chiroptical measurements, the details of which are described in the experimental Section S2.2 in the Supplementary Materials. The protocol is briefly described below.

To exclude undesirable chiroptical effects induced by hydrodynamic lamellar/vortex/turbulent flow [169–175], the authors verified whether CW/CCW stirring, which mimics

the *P*-symmetric Coriolis force in the northern and southern hemispheres resulting from the GF, and for comparison, static conditions, affects the resulting CD and UV spectra at 0, 20, and 40 °C. Although stirring direction-dependent CD spectra were obtained, it is still not yet clear why CW and CCW motions at the same stirring speeds did not induce mirror-symmetric CD spectra of PDBS-L and PDBS-H in *n*-$C_{12}H_{26}$, *n*-$C_{13}H_{28}$, *n*-$C_{14}H_{28}$, and *n*-$C_{16}H_{34}$. However, no obvious CD spectra of PDBS-L and PDBS-H in isooctane, *n*-C_6H_{14}, *n*-C_8H_{18}, and *n*-$C_{10}H_{22}$ under static and CW and CCW stirring conditions were induced. These unexpected results led to our adoption of static conditions to measure all the CD/UV spectra of the sample solutions and solvents at given temperatures. The anomaly in the effects of hydrodynamic flow on the CD spectral shapes and their chiroptical signs are described and discussed in Sections 2.7 and 3.10 in the main text and Sections S3.7 and S3.8 in the Supplementary Materials.

More importantly, prior to the heating and cooling runs of the chiroptical experiments at a given temperature under static conditions, preliminary annealing at 60 °C for at least 15 min under static conditions was carried out to reorganize the *n*-butyl side chains and Si–Si main chains from their disordered conformations. The details are described in Section S3.1 of the Supplementary Materials.

2.2. Effects of n-Alkane Chain Length and Temperature on CD-UV Characteristics of PDBS-L

To clarify the carbon number dependence of the *n*-alkanes, the VT-CD/UV spectra of PDBS-L in isotropic dilute solutions of *n*-C_8H_{18}, *n*-$C_{10}H_{22}$, *n*-$C_{12}H_{26}$, *n*-$C_{13}H_{28}$, *n*-$C_{14}H_{30}$, *n*-$C_{16}H_{34}$, and isooctane were measured under static conditions at 40, 20, and 0 °C for both heating and cooling runs, starting from 60 °C.

The CD and UV spectra of PDBS-L in isooctane and *n*-C_8H_{18}, *n*-$C_{10}H_{22}$, *n*-$C_{12}H_{26}$, and *n*-$C_{13}H_{28}$ at 0, 20, and 40 °C are shown in Figure S5a–c (Supplementary Materials). Cotton CD spectra emerging at ~300 nm in *n*-$C_{12}H_{26}$ and *n*-$C_{13}H_{28}$ were generated at 0, 20, and 40 °C, and *n*-$C_{16}H_{34}$ at 20 °C and 40 °C: (+)-sign at 0 °C, but (−)-sign at 20 °C and 40 °C. Less obvious CD spectra were recorded for the lower viscosity solvents isooctane, *n*-C_8H_{18}, and *n*-$C_{10}H_{22}$ at these temperatures.

When solutions of PDBS-L in *n*-$C_{12}H_{26}$, *n*-$C_{13}H_{28}$, *n*-$C_{14}H_{30}$, and *n*-$C_{16}H_{34}$ were cooled from 40 °C to 0 °C, the broader UV band at approximately 315 nm abruptly blueshifted to a narrower UV band at 299–302 nm. Such a blueshift has not yet been reported for this polymer. According to previous studies upon cooling of PDBS in *n*-hexane [152–156], the UV band around λ_{max} 320 nm at 22 °C undergoes an abrupt redshift around −35 °C, revealing a UV band at 355–360 nm at temperatures below −40 °C due to a change in conformation from the 7_3-helix of the Si main chain (dihedral angle (DH) ~ 150°) to other helices, e.g., 15_7-helix (~165°) and transoid 9_4-helix (~170°) [152–160].

The g_{abs} values of the bands around 300 nm at 0, 20, and 40 °C as a function of the *n*-alkane carbon number are plotted in Figure S5d (Supplementary Materials): g_{abs} = +6 × 10^{-4} in *n*-$C_{12}H_{26}$ at 0 °C was rather weak but fully recognizable. Importantly, the CD band at 299–302 nm emerges only when the corresponding UV band at 299–302 nm is the shorter tail of the 315 nm UV band, largely depending on the carbon number of *n*-alkanes and temperature. The sign of the CD band inverted between 0 °C and 20/40 °C, indicating the occurrence of a helix–helix transition. From the potential energy surfaces (PESs) of di-*n*-butyl 14-mer [152], diethyl-silane 4-mer [166], and diethylsilane 13-mer (discussed in Section 3.1), the 300 nm UV/CD band presumably derives from the DH 140–145° (and 220–225°) of the Si main chain as one of the local minima. These preliminary results encouraged a detailed investigation of the MPV effects of PDBS-H.

2.3. *n*-Alkane Carbon Number Dependence of CD-UV Characteristics of PDBS-H

The CD and UV spectra of PDBS-H in *n*-$C_{12}H_{26}$ and *n*-$C_{13}H_{28}$ over several temperatures are shown in Figure 1. For clarity, the corresponding raw CD and UV spectra of *n*-$C_{12}H_{26}$ are shown in Figure S6a–d, Supplementary Materials. The representative weaker CD and UV spectra of *n*-$C_{11}H_{24}$ and *n*-$C_{14}H_{30}$ are shown in Figure S7 (Supplementary Materials).

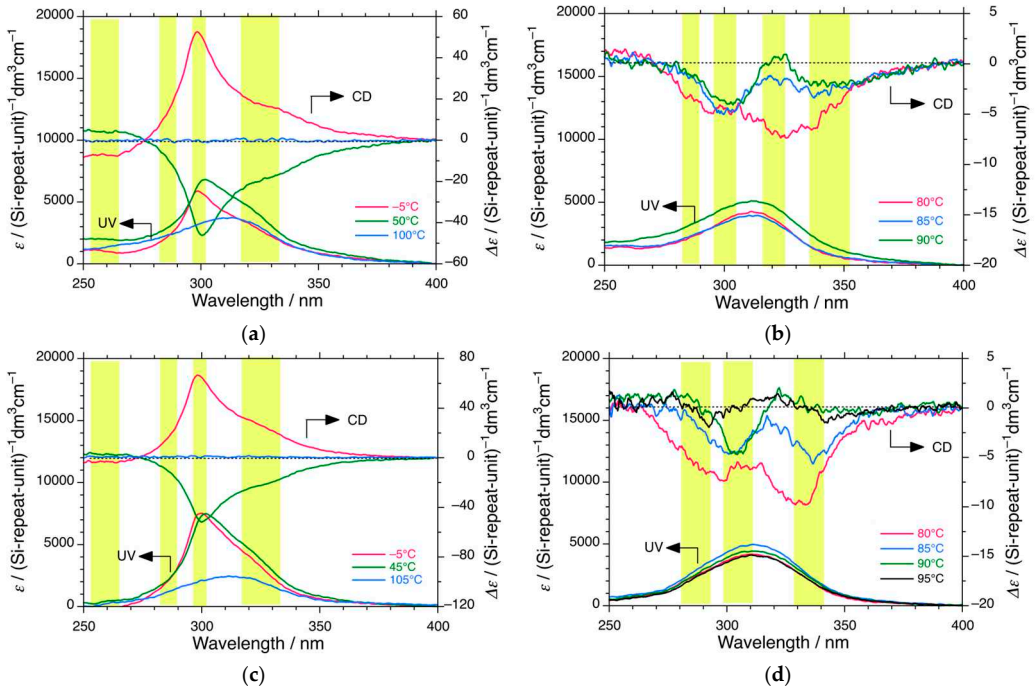

Figure 1. Changes in the CD and UV spectra of PDBS-H in (**a**) *n*-$C_{12}H_{26}$ at −5 °C (red), 50 °C (green), and 100 °C (blue), (**b**) *n*-$C_{12}H_{26}$ at 80 °C (red), 85 °C (blue), and 90 °C (green), (**c**) *n*-$C_{13}H_{26}$ at −5 °C (red), 45 °C (green), and 105 °C (blue), and (**d**) *n*-$C_{13}H_{26}$ at 80 °C (red), 85 °C (blue), 90 °C (green), and 95 °C (black). Conditions: $[Conc]_0 = 1.0 \times 10^{-5}$ M per Si-repeating unit, corresponding to $[Polymer]_0 = 5.2 \times 10^{-8}$ M as the polymer chain. The path length is 1.0 cm under static conditions. The dashed lines in (**a**–**d**) indicate baselines of CD spectra at the right side of the ordinate. The yellow areas in (**a**–**d**) suggest chiroptical generation, inversion, and disappearance of the handed helices at ~260 nm, ~285 nm, ~300 nm, ~325 nm, ~335, and ~345 nm.

Clearly, PDBS-H in *n*-$C_{12}H_{26}$ reveals a (+)-sign 300 nm CD spectrum at the corresponding 300 nm UV band at −5 °C, and conversely, a (−)-sign 300 nm CD spectrum at the corresponding 300 nm UV band at 50 °C. The (+)/(−) 300 nm CD effects completely disappeared at 105 °C, coincident with a marked broadening of the UV band and bathochromic shift to 315 nm. Similarly, PDBS-H in *n*-$C_{13}H_{28}$ shows a (+)-300 nm CD band with coincident 300 nm UV absorption at −5 °C but a (−)-300 nm CD band and 300 nm UV absorption at 45 °C (Figure 1a,c).

The g_{abs} value of PDBS-H reaches $+1.3 \times 10^{-2}$ in *n*-$C_{12}H_{26}$ at 0 °C and $+0.9 \times 10^{-2}$ in *n*-$C_{13}H_{28}$ at −5 °C but inverts to -0.8×10^{-2} in *n*-$C_{12}H_{26}$ at 50 °C and -0.7×10^{-2} in *n*-$C_{13}H_{28}$ at 45 °C. The 300 nm CD band with (+) and (−)-signs disappeared at 105 °C, coincident with a marked broadening of the UV band and bathochromic shift to 315 nm. PDBS adopts equal fractions of RH and LH 7_3-helices at 105 °C, resulting in a CD-silent racemic mixture of helices. PDBS-H in *n*-$C_{12}H_{26}$ and *n*-$C_{13}H_{28}$ at −5 °C additionally has three broad CD bands: (+)-CD at ~325 nm, (−)-CD at ~260 nm, and less obvious (+)-CD in the tail of the 300 nm CD at ~285 nm. However, the CD signals of the three additional bands were inverted at 50 °C.

When PDBS-H is in *n*-$C_{12}H_{26}$ and *n*-$C_{13}H_{28}$ at elevated temperatures in the range of 80–95 °C, three or four additional (−)-CD bands at ~285, ~305, ~320, and ~335 nm are

commonly observed (Figure 1b,d), indicating the generation of three or four intermediate helices in hot solutions. The magnitudes of the 300 nm CD spectra in *n*-$C_{11}H_{24}$ and *n*-$C_{14}H_{30}$ were much weaker (Figure S7, Supplementary Materials). The 300 nm CD signals in *n*-$C_{11}H_{24}$ emerge below 40 °C as a shoulder of the broader main UV band at 315 nm due to the 7_3-helix.

The g_{abs} values at the 300 nm CD bands of PDBS-H in *n*-$C_{11}H_{24}$, *n*-$C_{12}H_{26}$, *n*-$C_{13}H_{28}$, and *n*-$C_{14}H_{30}$ as a function of temperature are plotted in Figure 2. The temperature dependence of the g_{abs} curves reveals marked cooperativity which does not obey the Arrhenius law of thermal activation. As shown in Figure 2a,b, the (−)-CD 300 nm-CD bands in *n*-$C_{12}H_{26}$ and *n*-$C_{13}H_{28}$ were evident below 100–105 °C, diminished at ~28 °C, and inverted to (+)-sign g_{abs} below ~28 °C. The first critical temperature, T_{C1} (100–105 °C), relates to the second-order phase transition from mirror-symmetric 7_3-helices to the 300 nm CD helix with handedness. The second critical temperature, T_{C2} (~28 °C) relates to the second-order helix–helix transition of the 300 nm CD helix. From the temperature-independent g_{abs} values between −10 °C and T_{C2} and between T_{C2} and ~50 °C, the transition characteristics result from quantum tunneling between the RH and LH helices responsible for the 300 nm CD/UV band. The 300 nm CD/UV band at T_{C2} indicates a superposition of the RH/LH helices with 50/50 populations. Similar quantum tunneling helix–helix transitions were reported for rigid rodlike polysilanes bearing (*S*)-3-methylpentyl and (*R*)-3,7-dimethyl-octyl co-pendants [21–24,167,168].

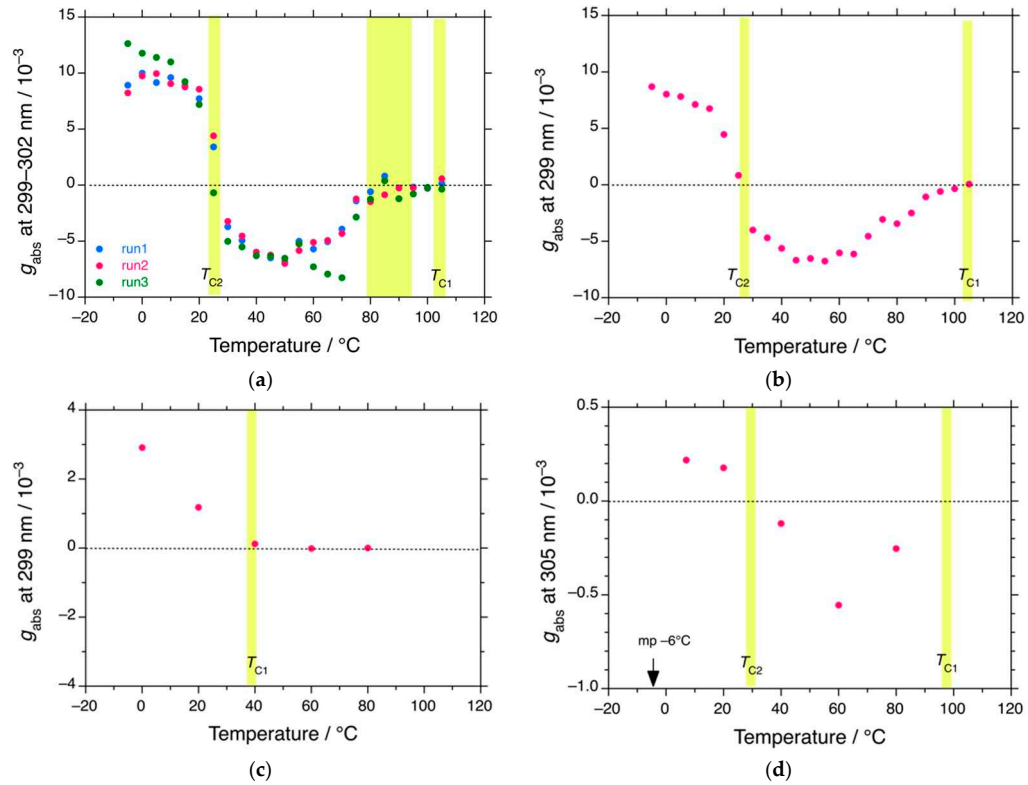

Figure 2. Changes in the g_{abs} values at 299–305 nm of PDBS-H in (**a**) *n*-$C_{12}H_{26}$ (runs 1,2, and 3), (**b**) *n*-$C_{13}H_{28}$, (**c**) *n*-$C_{11}H_{24}$, and (**d**) *n*-$C_{14}H_{30}$ as a function of temperature. Conditions: $[Conc]_0 = 1.0 \times 10^{-5}$ M per Si-repeating unit. The path length is 1.0 cm under static conditions. The yellow areas in (**a**–**d**) indicate the second-order helix-helix transitions at T_{C1} and T_{C2}. The dashed lines in (**a**–**d**) are a baseline of g_{abs} at the left side of the ordinate.

As shown in Figure 2c, the T_{C1} value of PDBS-H in *n*-$C_{11}H_{24}$ decreased to 40 °C, and the T_{C2} value could not be observed. As shown in Figure 2d, although the T_{C1} and T_{C2} values in *n*-$C_{14}H_{30}$ are nearly identical to those in *n*-$C_{12}H_{26}$ and *n*-$C_{13}H_{28}$, the absolute

magnitude of g_{abs} over the entire temperature range is weaker by an order of magnitude. Thus, for PDBS-H, the values of g_{abs}, T_{C1}, and T_{C2}, associated with the emergence and disappearance of the 300 nm CD and UV bands, are very susceptible to the temperature and carbon number of the *n*-alkane solvent.

Interestingly, less obvious alterations in the physicochemical properties of *n*-$C_{12}H_{26}$ are evident as a jump in specific volume ($cm^3 \cdot g^{-1}$, inverse of density) around 25 °C from an expected straight line of specific volume–temperature relationship (Figure S8 in Supplementary Materials) [176] and as a step-like increase in polarizability (dipole moment) of the CH_3 group at 1 THz (33 cm^{-1}, 4 × 10^{-3} eV) above 30 °C by VT-terahertz (THz) spectroscopy [177]. The occurrence of phase transitions due to change in the free-volume of *n*-$C_{12}H_{26}$ is weakly seen at ~30 °C, ~35 °C, and above 60 °C by the VT *ortho*-positronium (*o*-Ps) experiment [178]. These subtle transitions are reflected in T_{C2} (24–30 °C) of PDBS-H in *n*-$C_{12}H_{26}$, *n*-$C_{13}H_{28}$, *n*-$C_{14}H_{30}$, and *n*-$C_{12}D_{26}$, as discussed in Section 2.5.

2.4. Noticeable H/D Isotope Effects in n-Dodecane

The MPV theory (Scenario C) relies on the BCS theory of superconductivity. To solve such fundamental problems, it is important to test the substances in condensed phases rather than just as isolated collision-free species, as Philip Anderson discussed in a 1972 essay titled "More is different: Broken symmetry and the nature of the hierarchical structure of science" [179].

According to the BCS theory, a Cooper pair (a singlet boson, ↑↓) is formed by an attractive force between two repulsive fermions, $e^-(\uparrow)$ and $e^-(\downarrow)$, by indirect interactions between electrons and phonons (lattice vibrations) [180,181]. In an analogy of why a hydrogen molecule is spontaneously produced by two hydrogen atoms, roughly speaking, the Cooper pair constitutes a very weak chemical bond to bind two unpaired $e^-(\uparrow)$ and $e^-(\downarrow)$, due to the Pauli exclusion principle, and dissociates at T_c. The Debye frequency (θ_D) connecting $\theta_D \propto T_c$ is chosen from the highest frequency of the phonon vibrations. Historically, from clear experimental evidence, the product $m^{1/2} \cdot T_c$ is a constant for isotope effects of ^{198}Hg and ^{202}Hg and other metals (e.g., Sn, Pb, and Tl). θ_D is proportional to $m^{-1/2}$, while m is the mass of metal isotopes [182–184]. In chemistry, θ_D is chosen from the reduced mass (μ_m) between ^{12}C, ^{1}H, and ^{2}H, in the general form $\mu_m = (m_1 \cdot m_2)/(m_1 + m_2)$. In the present study, the highest θ_D values were obtained from the specific optically active vibrations of liquid *n*-$C_{12}H_{26}$ and *n*-$C_{12}D_{26}$, which involve stretching (symmetric and asymmetric), scissoring and rocking, wagging, twisting, and torsion modes of the methyl and methylene groups. In particular, chiral asymmetric stretching, rocking, and twisting phonons of *n*-alkanes are crucial for inducing handed helicity in PDBS. It is thus anticipated that the smaller θ_D values of *n*-$C_{12}D_{26}$ make T_{C1} and T_{C2} significantly lower than those in *n*-$C_{12}H_{26}$.

The CD and UV spectra of PDBS-H in *n*-$C_{12}D_{26}$ were measured as a function of temperature. Representative CD and UV spectra are shown in Figure 3a, although UV signals shorter than 280 nm were not clearly subtracted. A (−)-CD band emerged at −5 °C, whereas a (+)-CD band emerged at 40 °C; these CD bands completely disappeared at 55 °C. The g_{abs} value of the 300 nm CD band in *n*-$C_{12}D_{26}$ as a function of temperature is plotted in Figure 3b. The absolute g_{abs} values of PDBS-H in *n*-$C_{12}D_{26}$ were clearly an order of magnitude weaker compared with those in *n*-$C_{12}H_{26}$. T_{C1} decreased to ~42 °C, whereas T_{C2} at ~25 °C remained nearly unchanged. Interestingly, the signs of the CD signals in *n*-$C_{12}D_{26}$ below T_{C1} and T_{C2} are opposite to those in *n*-$C_{12}H_{26}$. This notable H/D isotope effect of *n*-dodecane suggests that the helix–helix transition characteristics at T_{C2} originate from PDBS-H itself since the difference in PES between *n*-$C_{12}H_{26}$ and *n*-$C_{12}D_{26}$ is almost negligible due to the bond length of C–D being only ~0.005 Å shorter than that of C–H [185].

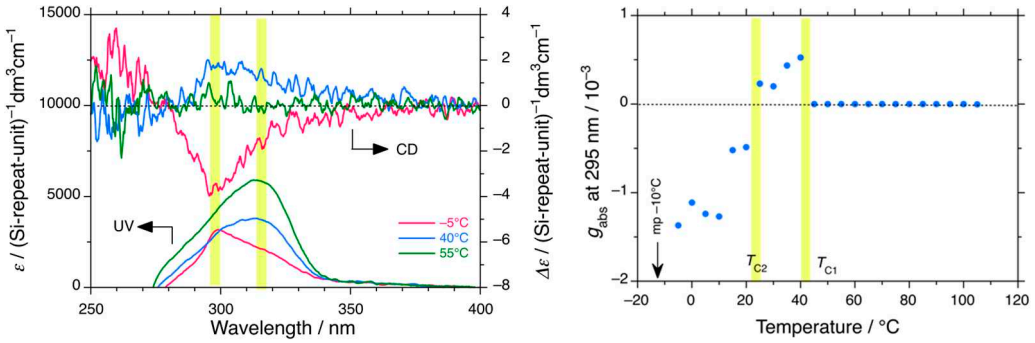

Figure 3. (**a**) Changes in the CD and UV spectra of PDBS-H in *n*-$C_{12}D_{26}$ at −5 °C (red), 40 °C (blue), and 55 °C (green) and (**b**) the g_{abs} values at 295 nm of the 300 nm CD band as a function of temperature. Conditions: $[Conc]_0 = 2.0 \times 10^{-4}$ M^{-1} per Si-repeating unit. Path length is 0.2 cm under static conditions. The dashed lines in (**a**) and (**b**) are baselines of CD spectra at the right side of the ordinate and g_{abs} at the left side of the ordinate, respectively. The yellow areas in (**a**) indicate chiroptical generation of the handed helices at ~295 nm and at ~315 nm. The yellow areas in (**b**) indicate two types of second-order helix-helix transitions at T_{C1} and T_{C2}.

2.5. Effects of Carbon Number and H/D Isotopes in n-Alkanes

To summarize the VT-CD/UV spectral characteristics described above, the g_{abs} values at the 300 nm CD band of PDBS-H at 0 and 20 °C as a function of the carbon number in *n*-alkanes are plotted in Figure 4a. The values of T_{C1} and T_{C2} as functions of the carbon number in *n*-alkanes are plotted in Figure 4b. A small difference in M_n and M_w between PDBS-H and PDBS-L resulted in a large difference in the MPV effects (Figure 4a and Figure S5, Supplementary Materials). According to Scenario A, there exist certain thresholds in DP_n and DP_w to cooperatively and nonlinearly elucidate the hidden MPV effects: PDBS-H (DP_n = 194, DP_w = 367) and PDBS-L (DP_n = 143, DP_w = 260).

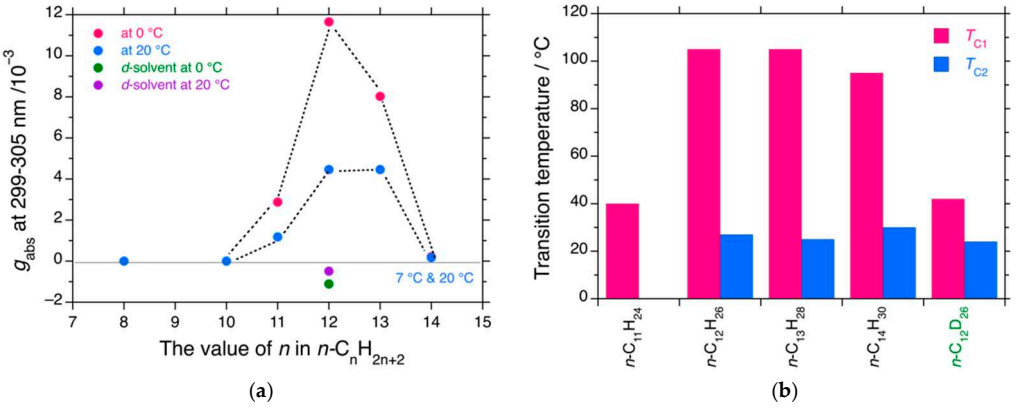

Figure 4. (**a**) Changes in the g_{abs} values at 299–305 nm at 0 °C and 20 °C as a function of chain length of *n*-alkanes, while for *n*-$C_{14}H_{30}$, g_{abs} are taken at 7 °C and 20 °C. (**b**) Changes in T_{C1} and T_{C2} vs. chain length of *n*-alkanes. The thin solid line in (**a**) is a baseline of g_{abs} at the left side of the ordinate.

Among the five medium-length *n*-alkane solvents, *n*-$C_{12}H_{26}$ exhibited the greatest MPV effects, accompanied by dual second-order phase transitions at T_{C1} and T_{C2} (Figure 4a). Similarly, *n*-$C_{13}H_{28}$ exhibited greater MPV effects, but the absolute g_{abs} values were somewhat weaker than those of *n*-$C_{12}H_{26}$. However, no odd–even effect of the carbon number in *n*-alkanes is observed. The absolute g_{abs} value of *n*-$C_{12}D_{26}$ was an order of magnitude lower than those of *n*-$C_{12}H_{26}$ and *n*-$C_{13}H_{28}$. As summarized in Figure 4b, *n*-$C_{12}H_{26}$, *n*-$C_{13}H_{28}$, and *n*-$C_{14}H_{28}$ had nearly identical T_{C1} values of 100–105 °C, whereas *n*-$C_{11}H_{24}$ had a markedly lower T_{C1} of 40 °C. All four of *n*-$C_{12}H_{26}$, *n*-$C_{13}H_{28}$, *n*-$C_{14}H_{28}$,

and *n*-$C_{12}D_{26}$ showed nearly identical T_{C2} values of 25–28 °C, although T_{C2} in the shorter *n*-$C_{11}H_{24}$ should be observed below −10 °C.

2.6. Temperature Dependent CPL and CD Characteristics of PDBS-H in n-$C_{12}H_{26}$

The normalized CPL/PL and CD/UV spectra of PDBS-H in *n*-$C_{12}H_{26}$ at −5, 25, and 60 °C are compared in Figure 5a–d. For clarity, the normalized CD/UV and CPL/PL spectra at −5 °C as functions of photon energy (in eV) and wavenumbers (in cm^{-1}) are shown in Figure 5e,f.

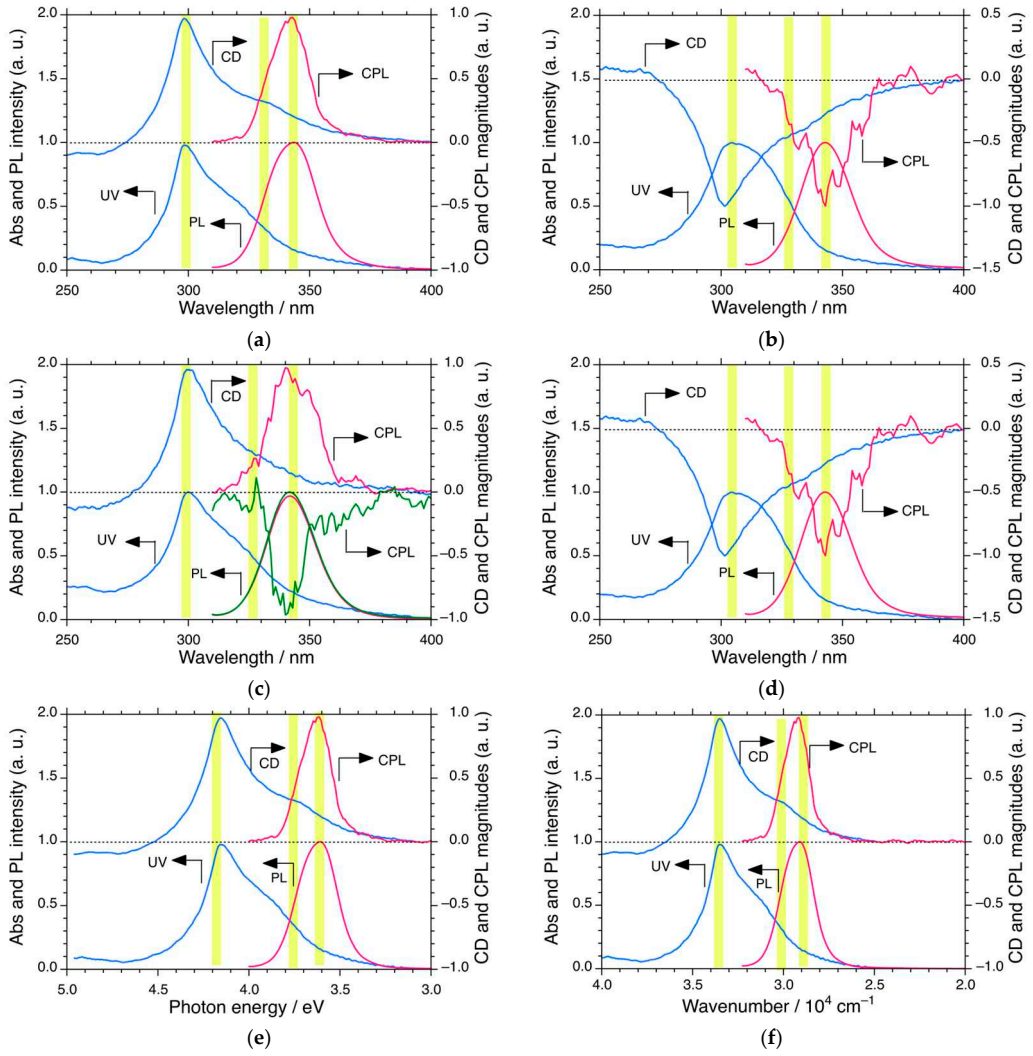

Figure 5. Normalized CD/UV (blue lines) and CPL/PL (red lines and red/green lines) spectra excited at 290 nm of PDBS-H in *n*-$C_{12}H_{26}$ as a function of wavelength at (**a**) −5 °C, (**b**) 60 °C, and (**c**) 25 °C. (**d**) CPL/PL spectra excited at 290 nm as a function of the wavelength (nm) at 25 °C. Normalized CD/UV (blue lines) and CPL/PL (red lines) spectra of PDBS-H in *n*-$C_{12}H_{26}$ at −5 °C as functions of (**e**) photon energy in eV and (**f**) wavenumbers in cm^{-1}. Data are taken from (**a**). The dashed lines in (**a**–**f**) are baselines of normalized CD and CPL magnitudes at the right side of the ordinate. The yellow areas in (**a**–**d**) suggest chiroptical generation and inversion of the handed helices at ~298 nm and ~328 nm in the ground state and the handed helix at ~ 340 nm in the photoexcited state.

At −5 °C below T_{C2}, the (+)-sign CPL spectrum affords g_{lum} (= $\Delta I/I$) = +1.9 × 10^{-2} at ~340 nm, while the corresponding CD spectrum shows g_{abs} = +1.3 × 10^{-2} at 300 nm with an apparent Stokes' shift of 4033 cm^{-1} (0.50 eV). Similarly, at 60 °C, between T_{C2} and T_{C1}, the (−)-sign CPL spectrum affords g_{lum} = −0.7 × 10^{-2} at ~340 nm, whereas the corresponding CD spectrum has g_{abs} = –0.5 × 10^{-2} at 300 nm with a similar Stokes

shift at −5 °C. Interestingly, the CPL spectra at 25 °C near T_{C2} greatly fluctuate between g_{lum} = +2.0 × 10^{-2} and −1.0 × 10^{-2}, as shown in Figure 5c,d.

The g_{abs} values as a function of temperature and the g_{lum} value at the three temperatures are plotted in Figure 6. The spectra of PDBS at T_{C2} show no bands due to the superposition of LH and RH helicities. The histograms of eight and four independent CPL measurements at 25 and 60 °C, respectively, are shown in Figure S9 (Supplementary Materials). The eight g_{lum} values at 25 °C are likely to obey a stochastic resonance rather than a sinusoidal function with time, implying that CPL in the S_1 state is hypersensitive to selection between RH and LH helicity due to the PVED-driven force to overcome fluctuations at 25 °C, whereas the four g_{lum} values at 60 °C are insensitive to fluctuations over time. In contrast, the results for the temperature region 25 °C ~ T_{C2} are indicative of bifurcation for selection between the LH and RH helicities in the S_1 state of PDBS. The LH- or RH-helicity in the S_1 state was not determined prior to the CPL measurement because of quantum entanglement between the LH- and RH-helicities.

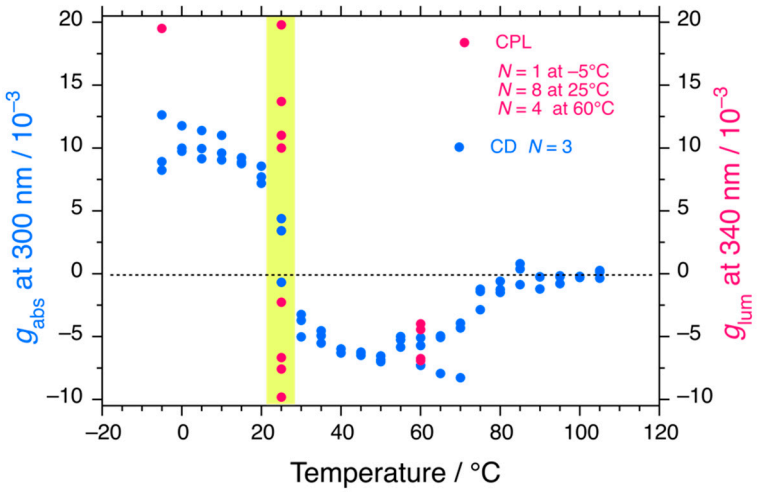

Figure 6. Changes in the g_{abs} values at the 300 nm CD/UV bands of PDBS-H in *n*-$C_{12}H_{26}$ (blue circles, N = 3 (runs 1, 2, and 3), data taken from Figure 2a) as a function of temperature and the corresponding g_{lum} values at 340 nm (red circles) at −5 °C, 25 °C, and 60 °C upon excitation at 290 nm. The yellow area indicates the second-order helix-helix transition at T_{C2} in the ground state of PDBS-H.

2.7. Non-Mirror-Symmetric CD Spectra of PDBS Under CW and CCW Stirring Directions

CD/UV spectra were recorded at 0 °C, 20 °C, and 40 °C for PDBS-L in *n*-$C_{12}H_{26}$, *n*-$C_{13}H_{28}$, *n*-$C_{14}H_{30}$, and *n*-$C_{16}H_{34}$ under static conditions and CW and CCW stirring at 100, 400, 600, and 800 rpm using a PTFE-coated cylindrical magnetic stir bar (2 mm in diameter × 7 mm in length) in a rectangular cuvette (10 mm path length and 35 mm in height) and the changes and differences are shown in Figure 7a–c and Figure S10a–h, Supplementary Materials, respectively. The changes in the CD/UV spectra of PDBS-H in *n*-$C_{12}H_{26}$ at 0 °C, 20 °C, and 40 °C under static and CW and CCW conditions at 1200 rpm are displayed in Figure S11 (Supplementary Materials).

Hydrodynamic flow in CW and CCW directions is recognized to induce mirror-image CD and CPL spectra from achiral chromophores/luminophores during aggregation by the removal of solvent and by gelation upon cooling achiral chromophores [169–175]. The chiroptical signs and product chirality are determined by the CW and CCW directions. Actually, in 1989, Goldanskii et al. pointed out that rotational hydrodynamic flow causes local *P*-symmetry breaking as a *PC*-EMF event [3].

Evidently, the non-mirror-image CD spectra under the CW and CCW flows of PDBS-L and PDBS-H in *n*-$C_{12}H_{26}$, *n*-$C_{13}H_{28}$, *n*-$C_{14}H_{30}$, and *n*-$C_{16}H_{34}$ below and above T_{C2} and at ~T_{C2} indicate the occurrence of a mechanism other than local *P*-symmetry breaking.

Under gentle stirring at 100, 400, and 600 rpm at 20 °C, PDBS-L in *n*-alkanes experienced an un-identified *PV*-related force (Figure S10a,b, Supplementary Materials). The hydrodynamic CW and CCW flow under the GF is no longer the local *P*-symmetry breaking force and becomes a global *PV* force, as discussed in Sections 3.9 and 3.10.

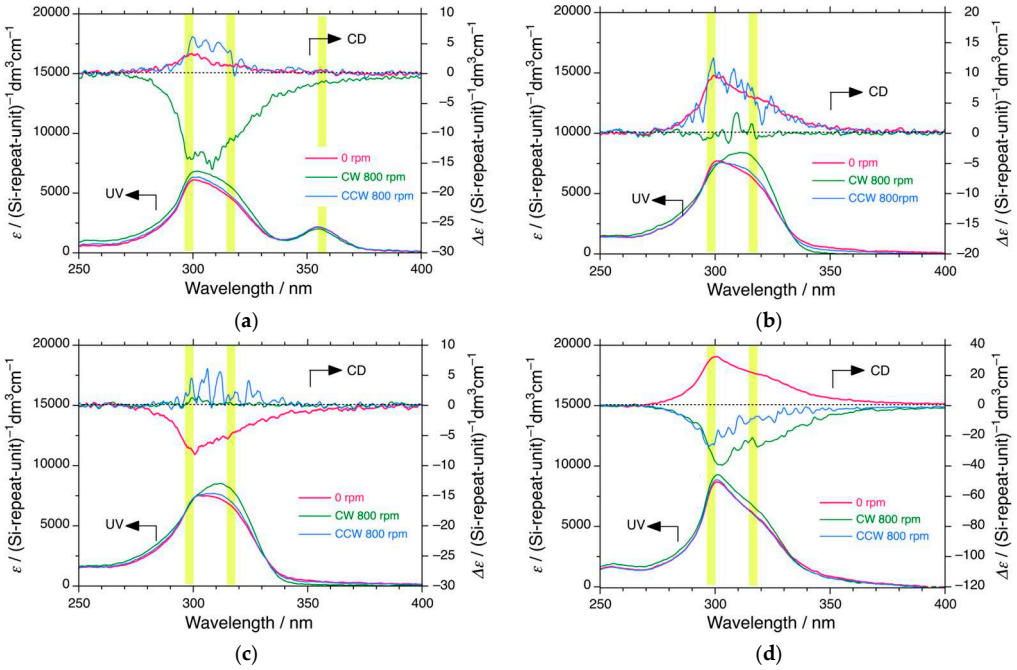

Figure 7. Changes in CD/UV spectra of PDBS-L in *n*-$C_{12}H_{26}$ at (**a**) 0 °C, (**b**) 20 °C, and (**c**) 40 °C and (**d**) PDBS-H in *n*-$C_{12}H_{26}$ at 0 °C under static (red), CW (green), and CCW (blue) stirring at 800 rpm. In this experiment, a PTFE-coated cylindrical magnetic stir bar (2 mm diameter × 7 mm length) was placed in a rectangular cuvette (10 mm path length and 35 mm height). The dashed lines in (**a**–**d**) are baselines of CD spectra at the right side of the ordinate. The yellow areas (**a**–**d**) suggest chiroptical generation, inversion, and disappearance of the handed helices at ~ 295 nm and ~ 318 nm.

3. Discussion

3.1. Potential Energy Surfaces at the Ground and Photoexcited States of PDBS

A primary question is the helical structure of PDBS in *n*-alkane solvents. The new helix responsible for the 300 nm CD and UV bands in a family of poly(di-*n*-alkylsilane)s and other poly(diorganosilane)s is yet not reported experimentally or theoretically [152–163]. Potential energy surfaces (PESs) at the ground and photoexcited states of Et-$(Et_2Si)_{13}$-Et (DES13) as a model of PDBS (Chart S2, Supplementary Materials) were calculated by semi-empirical PM3MM, DFT (B3LYP/6-31Gd), and TD-DFT, including three singlet and three triplet states (B3LYP/6-31Gd) using Gaussian 09 [186]. It is noted that the di-*n*-butylsilane 13-mer and its shorter 6-mer did not converge to optimized structures at the PM3MM level. The two PESs (PM3MM and DFT) normalized by 10 DH (dihedral angle) sets of the Si main chain as a function of DH are shown in Figure 8a,b. The photoexcitation energy (in nm) and oscillator strength (*f*) at the S_1 state as a function of DH are shown in Figures 8c and 8d, respectively. The magnitudes of UV (ε) and CD ($\Delta\varepsilon$) obtained with a full-width-at-half-maximum (*fwhm*) of 0.333 eV, and their g_{abs} values as a function of DH are depicted in Figures 8e and 8f, respectively.

As shown in Figure 8a,b, DES13 possesses five minima at 170° (gray), 155° (red), 140° (blue), 130° (green), and 100° (yellow) in the Si main chain. The helix at 155° is the global minimum. The first metastable helix at 140° was connected to the deviant ($D_{\pm}$) helix of Et-$(Et_2Si)_4$-Et [166]. The 140°-helix is ascribed to the 300 nm CD/UV bands discussed in this work, presumably the 8_3-helix, while other local minima at 130° are likely to be 11_4-helices

with λ_{max} 280 nm. The 170°- and 155°-helices correspond to the 15_7-helix (λ_{max} 355 nm) and 7_3-helix λ_{max} 315–320 nm), respectively [152–156]. The CD/UV bands due to the 130°-helix can be weakly observed as the tail of the 300 nm CD/UV bands (Figure 1). The 100°-helix is experimentally observable as weak (−)-CD and broad UV bands around λ_{max} 255–265 nm compared to the 300 nm (+)-CD band (Figure 1) because the chiroptical signs in the CD bands between 70° < DH < 100° and 100° < DH < 170° are theoretically opposite (Figure 8e).

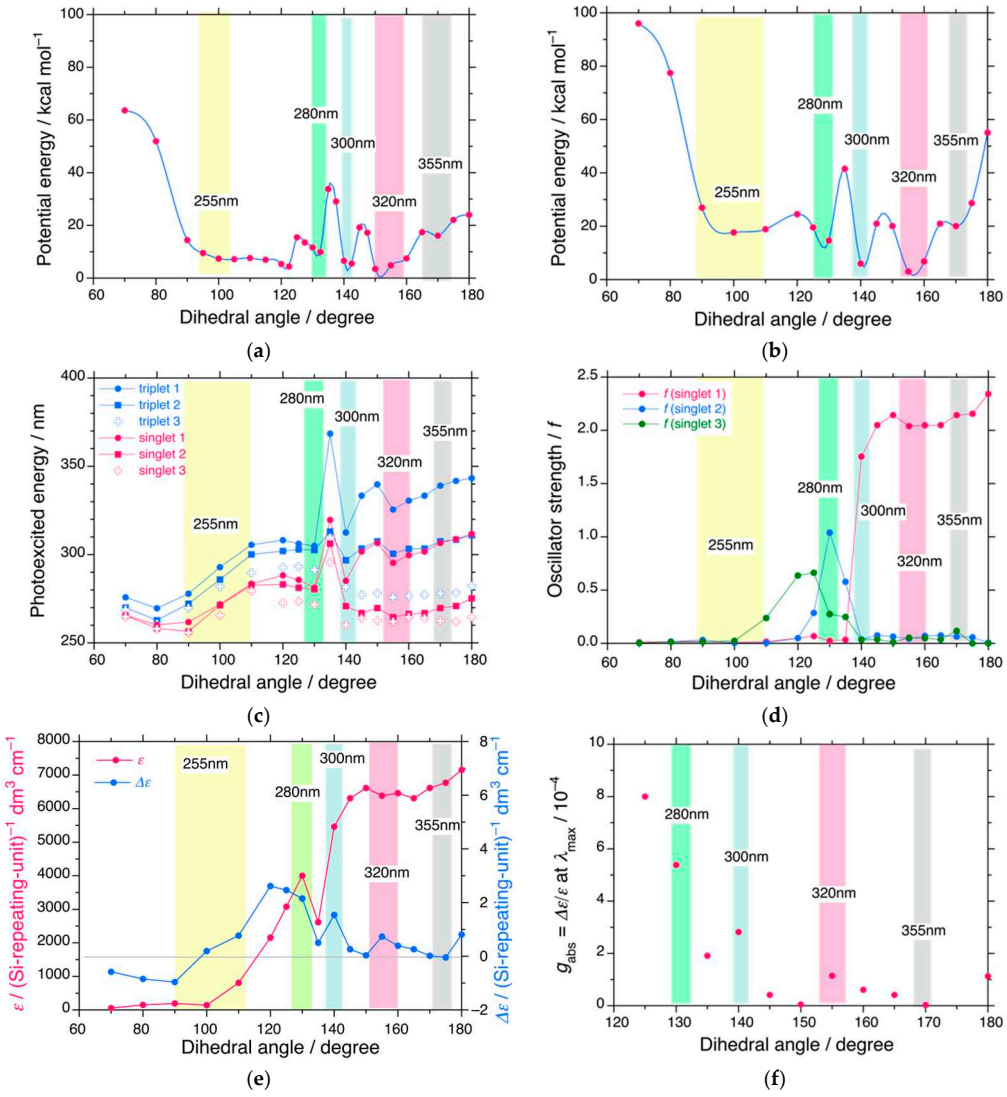

Figure 8. (**a**) Potential energy (red spline curve) of Et-$(Et_2Si)_{13}$-Et vs. the dihedral angle (DH) of Si main chain obtained with PM3MM. (**b**) Potential energy (red circles with spline blue curve) of Et-$(Et_2Si)_{13}$-Et vs. the Si dihedral angle obtained using DFT (B3LYP with 6-31Gd basis set) based on the optimized models by PM3MM. (**c**) Photoexcitation energies (nm) of three triplets, T_1 (blue circles), T_2 (blue squares), T_3 (blue cross), and three singlets, S_1 (red circles), S_2 (red squares), S_3 (red crosses) vs. the Si dihedral angle obtained with TD-DFT (B3LYP with 6-31Gd basis set). (**d**) Oscillator strengths, *f*, at S_1 (red), S_2 (blue), and S_3 (green) states vs. Si dihedral angle. (**e**) Magnitudes in UV, ε (red filled circles) and CD, Δε (blue filled circles) at λ_{max} of Et-$(Et_2Si)_{13}$-Et obtained with *fwhm* 0.333 eV vs. Si dihedral angle. (f) g_{abs} value at λ_{max} vs. Si dihedral angle, with data taken from Figure 8e. The energies in (**a**) and (**b**) are normalized by 10 Si dihedral sets, whereas, in (**e**), the ε and Δε values are normalized by 13 Si repeating units. The thin solid line in (e) is a baseline of CD magnitude at the right side of the ordinate. The yellow, green, blue, red, and gray areas in (**a**–**f**), respectively, indicate the helices that afford the corresponding UV–CD spectra at 255 nm, 280 nm, 300 nm, 320 nm, and 355 nm.

The helix–helix transition capability between the four steep wells at ±140° and ±155°, associated with larger E_B values, plays a key role in observable MPV effects. The E_B between 140° and 150° was ~20 kcal mol^{-1} by PM3MM and ~25 kcal mol^{-1} by DFT. Similarly, the E_B between 150° and 210° was ~25 kcal mol^{-1} by PM3MM and ~55 kcal mol^{-1} by DFT. Chiroptical generation and inversion between RH and LH helices from the most stable +155° helix to the other +140°, −140°, and −155° helices are unlikely to occur easily because of the large E_B values.

The photoexcited energies (expressed in nm) at the S_1, S_2, and S_3 states (marked in red) and T_1, T_2, and T_3 states (marked in blue) significantly change as a function of DH due to the decrease in σ-conjugation of the Si wire (Figure 8c). The photoexcited energies at S_1, S_2, and S_3 tended to progressively blueshift when the DH changed from 180° to 80°, except for 145–150° and 135° located at barriers between 140° and 155° and between 130° and 140°. The UV/CD bands in the S_2 and S_3 states can be observed experimentally at wavelengths shorter than 280 nm and partly overlap with the UV/CD bands of the 100°-helix, whereas the UV/CD bands in the S_1 state appeared at wavelengths longer than 280 nm. The DH dependence of the photoexcited energies in the T_1, T_2, and T_3 states was nearly identical to those in the S_1, S_2, and S_3 states (Figure 8c). Their UV absorptions were experimentally less obvious because their f values (oscillator strengths) were theoretically zero.

It is noteworthy that when DH changes from 180° to 155°, the transition energy curve at the S_1 state approaches the curve at the T_2 state, and the curve at 140° is close to that of the T_3 state (Figure 8c). These situations led to mixing between the S_1, T_2, and T_3 states, resulting in a marked decrease in the e value, accompanied by an increase in De at 140°. Additionally, from $E_{PV} \propto \Delta E_{ST}$ (Scenario E), a smaller S_0–T_1 transition energy at three energy minima, 130°, 140°, and 155°, in the range of 3.81 eV (325 nm) and 4.13 eV (300 nm) effectively contributes to amplify E_{PV} in the S_0 state because the T_1 is partly mixed with the S_1 and T_2 states.

The f values in the S_1, S_2, and S_3 states were altered by the DH (Figure 8d). When the DH decreases from 170° to 70°, f in the S_1 state progressively decreases from ~2.2 at 170° to ~0.0 at 130°. Conversely, f in the S_2 state increases from ~0.1 at 170° to 0.7–1.0 at 130–135°. Likewise, f in the S_3 state increases from ~0.1 at 170° to 0.7 at 120–125°. Consequently, when the DH changed from 180° to 125°, $\Delta\varepsilon$ increased; conversely, ε decreased (Figure 8e), leading to an increase in g_{abs} (= $\Delta\varepsilon/\varepsilon$) (Figure 8e,f). Focusing on the three helices with DHs of 155°, 140°, and 130°, the UV/CD bands at 280 nm and 320 nm mainly arose from the S_1 state, while the UV/CD bands at 300 nm were mainly from the S_2 state (Figure 8d). The g_{abs} at 300 nm were approximately three times larger than those at 320 nm. This idea partly accounts for the reason why $|g_{abs}|$ at 300 nm reaches ~10^{-2} compared to $|g_{abs}|$ at 320 nm of ~10^{-4} [22,23,159,160].

A considerably large E_B ranging from 15 to 50 kcal mol^{-1} is crucial to largely suppress $\Delta E_{\pm}$ in multiple-well systems [113,187–189], leading to the emergence of observable MPV effects. These E_B values are intermediate in racemization processes between temperature-independent quantum tunneling and classical temperature-dependent Arrhenius law mechanisms [189]. From $\Delta E_{\pm} = 1/(2\sqrt{\pi})\cdot(h\nu\cdot E_B)^{1/2}\cdot\exp(-E_B/h\nu)$, where h is the Planck constant, and ν is the frequency of vibration in a single well, tunnel-driven dynamic racemization is expressed as $T_{rac} = h/\Delta E_{\pm}$ [10,113,187,189]. For comparison, in the case of the quantum tunneling inversion of ammonia in a DWP, H_3N: ⇄ :NH_3, an E_B of 5 kcal mol^{-1} at ν = 950 cm^{-1} leads to a very fast T_{rac} ~ 10^{-11} s, while the tunneling inversion of phosphine in a DWP, H_3P: ⇄ :PH_3, an E_B of 37 kcal mol^{-1} at ν = 991 cm^{-1} results in a very slow T_{rac} ~ 10^7 s [10,113,189]. By placing two adjustable parameters in the above $\Delta E_{\pm}$ and T_{rac} equations, the T_{rac} values (in sec) as a function of E_B (kcal mol^{-1}) in the three cases of tunneling, Arrhenius law mechanisms, and their intermediate, are illustrated

in Figure S12 (Supplementary Materials) [113,189]. The estimated E_B (PM3MM) of DES13 with two E_B ranges of ~20 kcal mol^{-1} and ~25 kcal mol^{-1} indicate an intermediate region, except for ~55 kcal mol^{-1} (DFT) around DH 180° (Figure 8b) [189].

Qualitatively, a larger E_B in a DWP makes $\Delta E_{\pm}$ exponentially smaller, thereby satisfying the $\Delta E_{\pm} \sim E_{PV}$ condition, whereas a tiny E_{PV} is nearly unchanged around 10^{-10} eV. Experimentally, by increasing E_B, it is, in principle, possible to achieve $\Delta E_{\pm} \sim 10^{-10}$ eV by (i) increasing the viscosity of the solvents, (ii) increasing the steric hindrance between the side chains of chromophores, and (iii) cooling to a lower temperature. The cooperativity in the second-order phase transition originates from a continuous decrease from disordered to ordered states at low temperatures, i.e., superconductivity and BEC of HINS isotopes such as ^{87}Rb, ^{23}Na, ^{7}Li, and ^{1}H [190].

3.2. Potential Energy Surfaces of H-(H$_2$Si)$_{13}$-H, Me-(Me$_2$Si)$_{13}$-Me, and Et-(Et$_2$Ge)$_{13}$-Et

The other PESs of H-(SiH_2)$_{13}$-H, Me-($SiMe_2$)$_{13}$-Me, and Et-($GeEt_2$)$_{13}$-Et (Chart S2 (Supplementary Materials)) obtained using PM3MM and DFT (B3LYP-631Gd) are compared in Figure S13 (Supplementary Materials). The global and local minima of H-(SiH_2)$_{13}$-H exist at 180° (*trans-planar* (*TP*)) and 60–70° (*gauche helical* (*GH*)), respectively, and the E_B values between *TP* and *GH* are as small as 0.6 kcal mol^{-1} (PM3MM) and 0.8 kcal mol^{-1} (DFT), respectively (Figure S13a,b, Supplementary Materials). However, the PES of Me-($SiMe_2$)$_{13}$-Me suggests that the global and local minima are located at 180° (*TP*) and 90° (*ortho helical* (*OH*)), while the E_B values between the *TP* and *OH* conformers are 12 kcal mol^{-1} (PM3MM) and 25 kcal mol^{-1} (DFT), respectively (Figure S13c,d, Supplementary Materials). Similarly, the shallow energy levels at the two minima with lower E_B (indicated by yellow and gray) suggest a high susceptibility to fluctuations.

Similarly, the PES in hypothetical Et-($GeEt_2$)$_{13}$-Et has two minima at ~155° and ~90°. Because of the similar shallow energy levels, the preference in the LH and RH helicity is rapidly lost owing to thermal fluctuations, as indicated by the blue, pink, and gray bars (Figure S13e,f, Supplementary Materials). Significant differences in local and global minima and their E_B values between Et-($SiEt_2$)$_{13}$-Et and Et-($GeEt_2$)$_{13}$-Et are largely ascribed to a subtle difference in bond lengths between Si–Si (2.10 Å) and Ge–Ge (2.22 Å) [185]: a shorter bond length results in a stronger steric repulsive force (Pauli exclusion principle) between bulkier pendant groups.

3.3. Potential Energy Surface with PVED of n-Alkanes

In principle, *GH* in *n*-alkanes can result in a metastable rotamer. Kikuchi et al. calculated the E_{PV} in a series of hypothetical *GH* *n*-alkanes [191,192]. The RH-*GH* of *n*-$C_{11}H_{24}$ is more stable by -5×10^{-18} kcal mol^{-1}. The E_{PV} of RH-*GH* linearly increases in proportion to the carbon number of *n*-alkanes (Scenario A) [191,192]. From studies of Raman, FT-IR, and theoretical simulations, the difference in energy between *trans* (*t*)- and *gauche* (*g*)-bonds per C–C bond, ΔE_{tg}, is 0.65–0.90 kcal mol^{-1} in a series of *n*-alkanes from *n*-C_4H_{10} to *n*-$C_{16}H_{34}$ [193–198]. DFT (B3LYP/6-311g**) calculations indicated that the E_B from *t*- to *g*-bonds is commonly ~3 kcal mol^{-1} in a series of *n*-C_4H_{10} to *n*-$C_{10}H_{22}$ [199,200]. In a series of carbon numbers from *n*-C_5H_{12} to *n*-$C_{14}H_{30}$, liquid *n*-alkanes contain in total 34–41% as polar *g*-bonds, including one *g*-, two *g*-, and three *g*-sets, resulting in a weak dipole moment of 0.09 Debye [177,199–209]. Although *n*-C_4H_{10} adopts ~16% *g*-bond, *n*-C_5H_{12} and *n*-$C_{11}H_{24}$ contain ~25% *g*-bonds, and *n*-$C_{16}H_{34}$ is ~35% *g*-bonds [195,201–206]. According to a recent MM3 calculation of *n*-$C_{12}H_{26}$, the most dominant *TP*-conformer among the possible 7838 conformers is only ~15%, while five non-*TP* conformers, including one and two *g*-bonds, are ~15%, and other non-*TP* conformers are 70% [198]. On the other hand,

Monte Carlo simulation indicates that *TP*-conformer content ranges from ~75% to ~85% for carbon numbers 6 to 12 in *n*-alkanes [197].

To confirm these results, we calculated two PESs of *n*-$C_{12}H_{26}$ as a function of DH 40–180° obtained using PM3MM and DFT (B3LYP/6-31Gd) (Figure S13g,h, Supplementary Materials). In both calculations, the PESs suggested a global minimum at 180° (*TP*) and a local minimum at 80° (*OH*), with an E_B of ~5 kcal mol^{-1}. The UV/CD spectra (*fwhm* 0.20 eV, TD-DFT) for several rotamers of *n*-$C_{12}H_{26}$ are summarized in Figure S14 (Supplementary Materials). Comparisons of the relative energy, dipole moments (μ, in Debye), and CD sign at λ_{ext} for 10 rotamers, including g^+ ~ 60–80° (9 DH sets of C–C bonds), are listed in Table S1, Supplementary Materials. These data were sorted by the relative energy against *TP* [$(t)_9$], as shown in Figure S14 (Supplementary Materials).

The first metastable rotamer is the g^+ rotamer [$(g^+)_1$-$(t)_8$], which is unstable by 3.24 kcal mol^{-1} relative to [$(t)_9$]. The value semi-quantitatively agrees well with the previous calculations [193–200]. The second metastable rotamers are a two g^+ rotamer, [$(g^+)_2$-$(t)_7$], and a one g^+ rotamer, [$(t)_1$-(g^+)-$(t)_7$], which are unstable by 4.23–4.45 kcal mol^{-1}. The third metastable rotamer is a one g^+ rotamer, [$(t)_2$-(g^+)-$(t)_6$], which is unstable by 5.74 kcal mol^{-1}. Interestingly, [(g^+)-$(t)_9$] showed (+)-sign CD; conversely, [$(g^+)_2$-$(t)_7$] and [(t)-(g^+)-$(t)_7$] showed (−)-sign CD. Although the μ-value of *TP* is nearly zero, the other five rotamers, [$(g^+)_9$], [$(g^+)_1$-$(t)_8$], [$(g^+)_2$-$(t)_7$], [$(t)_2$-(g^+)-$(t)_6$], and [$(t)_4$-(g^+)-$(t)_4$], show fairly large μ values ranging from 0.049 to 0.087 Debye. The other four g^+-containing rotamers, [$(t)_1$-(g^+)-$(t)_7$], [$(g^+)_3$-$(t)_6$], [$(g^+)_4$-$(t)_5$], and [$(t)_3$-(g^+)-$(t)_5$], had smaller μ values (0.015 and 0.029 Debye). Liquid *n*-$C_{12}H_{26}$ and other *n*-alkanes are thus likely to contain a considerable amount of polar one- and two-g^+ and/or g^- bonds and kinks (g^+-*t*-g^- and g^--$(t)_n$-g^+) [201–209]. The [$(g^+)_1$-$(t)_8$], well-known as end-g^+, is easily formed compared to interior g^+-bonds, such as [$(t)_1$-(g^+)-$(t)_7$], [$(t)_2$-(g^+)-$(t)_6$], and [$(t)_4$-(g^+)-$(t)_4$]. The fractions of the *g*-bonds increase as the temperature increases [201–206].

3.4. Electroweak Charges at Isotopes of PDBS and n-Alkanes

The electroweak charge, Q_W, is an important parameter in the Z^0-force origin MPV theories [5,6,18,19,70,73–77,83]. Q_W is regarded as a naturally occurring additional charge on each spherical atom to afford the north and south poles induced by the handed WNC.

$$H_{PV} = -\Gamma/2 \sum\sum Q_W\{\boldsymbol{p}_i\cdot\boldsymbol{\sigma}_i, \Delta^3(\boldsymbol{r}_i - \boldsymbol{r}_a)\}_+, \quad (1)$$

$$\Gamma = G_F/(2\sqrt{2}\cdot m_e\cdot c) = 5.731 \times 10^{-17} \text{ a.u. equivalent to } 1.559 \times 10^{-15} \text{ eV}. \quad (2)$$

$$Q_W = N_a - (1 - 4\cdot\sin^2\theta_w)\cdot Z_a \quad (3)$$

Herein, the H_{PV} (*PV*-potential) is reduced by adding H_{PV}(e^--e^-), H_{PV}(e^--*p*), and H_{PV}(e^--*n*) terms when e^-–e^-, e^-–*p*, and e^-–*n* interactions between e^-, *n*, and *p* are considered. Additionally, $\{\}_+$ denotes an anticommutator. Γ combines the Fermi weak coupling constant G_F with the electron mass m_e and speed of light *c*. Each electron *i* has a charge density at each atomic nucleus, which is represented by a three-dimensional Dirac delta function, $\Delta^3(\boldsymbol{r}_i - \boldsymbol{r}_a)$. In addition, $\boldsymbol{p}_i$ and $\boldsymbol{\sigma}_i$ are the electron momentum and Pauli spin-matrix operators, respectively. N_a and Z_a (=*Z*, mentioned above), respectively, are numbers of *n* and *p* of each atomic nucleus *a* in a molecule, and θ_w is the Weinberg mixing angle between *W* and Z^0 bosons.

Using the recent value of $\sin^2\theta_w = 0.223$ [210], it can be shown that for ^{1}H, $Q_W = -0.108$; for ^{2}H (D), $Q_W = +0.892$; for ^{13}C (NA 1.1%), +6.352; for ^{12}C (NA 98.9%), +5.352; for ^{29}Si (NA 4.7%), +13.488; for ^{28}Si (NA 92.2%), +12.488; and for ^{30}Si (NA 3.1%), +15.849, where NA is the natural abundance of stable isotopes. Only the ^{1}H atom has a small (−)-sign Q_W. In contrast, ^{2}H and other HINS and INS isotopes have a large (+)-Q_W. A large quantity

of solvent organic molecules with multiple (−)-Q_W ^{1}H atoms surround the PDBS. The opposite sign in the Q_W between ^{1}H and ^{2}H is related to the opposite CD sign characteristics between *n*-$C_{12}H_{26}$ and *n*-$C_{12}D_{26}$ and PDBS below T_{C1} and T_{C2} (Figures 2a and 3b). In addition, (+)-Q_W HINS ^{29}Si can contribute to an MPV-causing "sergeant" to cooperatively align in a handed helical geometry of ^{28}Si and ^{30}Si as "soldiers" in the Si main chain, leading to the weaker MPV effect of PDBS observed in *n*-$C_{12}D_{26}$ [107].

3.5. CH_3 Hindered Rotor—Three Identical Nuclear Spin-1/2 System in a Triple-Well Potential

3.5.1. Ortho- and Para-Water to Account for the MPV-Experiment of L- and D-Oligopeptides

In 2006, Shinitzky et al. investigated the first-order α-helix-coil transition characteristics of an enantiomeric pair of L- and D-glutamic acid 24-mers [100]. They noticed subtle differences in the CD spectra between their random coils in H_2O at pH 10.5; however, no such difference was observed in the D_2O: H_2O (4:1) cosolvent. Isothermal titration calorimetry detected subtle differences in $\Delta H \sim -0.14$ kcal per residue between the L- and D-oligopeptides in H_2O but did not show such ΔH in the D_2O: H_2O 4:1 mix. Based on the fact that H_2O consists of two nuclear spin isomers, *para* (↑↓, $I = 0$) and *ortho* (↑↑, $I = 1$) in 1:3 ratio, *ortho*-H_2O is assumed to solvate the L-oligopeptides preferentially over the D-oligopeptides [100]. The *ortho*- and *para*-spins in CH_2 moieties are applicable to *n*-alkanes and the *n*-butyl pendants of PDBS, although their total I values are perpetually 0 and 1, respectively.

3.5.2. Bi-Directional CH_3 Rotor by Tunneling and Non-Arrhenius Law Hopping

Based on the *ortho-para* spin states of H_2O, the nuclear spin states of CH_3 termini in *n*-alkanes and *n*-butyl pendants were first considered. A naive question is how three identical HINS atomic systems conserve *P*-symmetry, because even-number nuclear spin states ($I = 0,1,2$) are impossible. When considering a plausible explanation for the mechanism(s) of the observed MPV effects, the authors were aware of the uniqueness of the CH_3 group. Historically, in 1940, Koehler and Dennison were the first to argue theoretically regarding hindered and free rotations of the OH group in methanol using the energy potential $V = 1/2 \cdot H \cdot (1 - \cos 3\theta)$ and energy splitting [211]. In the 1960s, Hilt and Hubbard [212] and, independently, Runnels [213] theoretically treated how a three identical nuclear spin-1/2 system relaxes along the three-fold hindered rotation axis. These old questions can nowadays be reduced to a geometrical frustration, i.e., spin frustration and degeneracy of HINS in odd-number rings including triangular lattices in condensed matter physics and topological material science [214–219].

From the notable HINS isotope effects to the APV and *PV*-MAM hypotheses (Scenario F), the present study highlights three-fold symmetric CH_3 and CD_3 groups as a fundamental issue in soft condensed matter. Thus far, it has been more-or-less established over the last four decades that CH_3 and CD_3 groups act as hindered rotors in a TWP owing to temperature-dependent quantum tunneling and non-Arrhenius law hopping mechanisms in the framework of *PC*-EMF [220–244]. Rotating the symmetry-top CH_4, NH_4^+, and CH_3-group in a broad range of molecular crystals [220–239] and non-crystalline polymers [240–244] between 1 K and 390 K are elucidated by many theories and various measurements; i.e., inelastic neutron scattering (IENS), quasielastic neutron scattering (QENS), several ^{1}H-NMR techniques (i.e., spin lattice relaxation (T_1), low-magnetic-field, high-field to zero-field cycling, level crossing), ^{2}H-NMR, electron nuclear double resonance (ENDOR), IR and Raman, microwave, viscoelastic relaxation, and photochemical hole burning [220]. The CH_3 group possesses a perpetual $I = 3/2$ (↑↑↑, ↓↓↓, *A*-state) and $I = 1/2$ (↑↓↑ and ↑↓↓, *E*-state). Contrarily, the CD_3 group of three identical ^{2}H isotopes generates $I = 0,1,3$ (*A*-state) and

I = 1,2 (E-state) [235–239]. However, theoretical and experimental investigations involving the nuclear spin-dependent MPV hypothesis have not yet been reported.

In 1991, Clough pointed out that the origins of CH_3 and CD_3 rotating motions in a TWP remain unanswered questions regarding the four symmetry breakings: geometrical, T-reversal, rotational, and permutational symmetries [227]. These issues can be reduced to the superposition of three identical 1/2-nuclear spin states among three indistinguishable ^{1}H atoms that split into four A-sublevels and two sets of E_a-/E_b-sublevels under a non-zero external magnetic field in NMR. The A- and E-states contradict the Pauli exclusion principle. Zero-field NMR spectroscopy and sophisticated chiroptical spectroscopy can be used to answer these questions [90]. In addition, the CH_3 rotating trajectory can be regarded as a set of helices in which the rotation is linked with environmental forces because the rotor acts as a clock and pendulum in the curvature of the space-time world [227]. However, no study has experimentally validated the four-symmetry breakings of CH_3 and CD_3 rotors.

The CH_3 and CD_3 hindered rotors can generate several g-bonds in liquid n-alkanes and n-butyl pendants due to the similar E_B values in non-deuterated and deuterated polymers [240–244]. Their quantum tunneling and non-Arrhenius law hopping characteristics are significantly different due to the inherent moment of inertia (I_{rot}) and rotational constant (B), $B = \hbar^2/(2I_R)$ when considered as rigid rotors: for CH_3, B = 0.655 meV ($I_{rot} = 0.535 \times 10^{-46}$ kg m^{-2}) and for CD_3, B = 0.328 meV ($I_{rot} = 1.069 \times 10^{-46}$ kg m^{-2}) [220,222,238]. In fact, the differences in the B and I_R of CD_3 result in the marked suppression of tunneling splitting ($E_{A–E}$) and tunneling frequency by one or two orders of magnitude [220,222,238]. The reduced tunneling frequency of the CD_3 rotor causes inefficient intra- and intermolecular chirality transfers.

By considering several graphical explanations for the permutational quantum tunneling of the CH_3 rotor in TWP [220–227,240–244], Figure 9a reproduces the hypothetical potential energy $E(\theta)$ as a function of CH_3 rotation angle (θ); $E(\theta) = V_3/2 \cdot \{1 - \cos(3\theta)\}$, $V_3 \simeq E_B$ = 25.2 meV (1.1 kcal mol^{-1}) while the V_3 is taken from CH_3NO_2 [221,224,225]. $E(\theta)$ exhibited three global minima at $\theta = \pm 120°$ and 0°. The $E(\theta)$ at each well (1, 2, 3) splits into A- and E_a-/E_b-states owing to quantum tunneling, whereas E_a and E_b have equal energies owing to degeneracy. The relative stability between A- and E_a/E_b-states alternatively changes with v = 0, 1, 2 [222]. Representative IENS spectra at cryogenic temperatures revealed two well-resolved $A \rightarrow E_a/E_b$ and $E_a \rightarrow E_b/E_b \rightarrow E_a$ transitions at zero frequency [221,227]. With an increase of temperature, tunneling splitting energy, $E_{A–E}$ (in eV, cm^{-1}, Hz), exponentially decreases, approaching the zero-frequency. When $E_a = E_b$, a pair of CW and CCW rotations between three potential wells—well 1, well 2, and well 3—occurs equally, leading to a random hopping of bi-directional rotations resulting in the lack of macroscopic level optical activity.

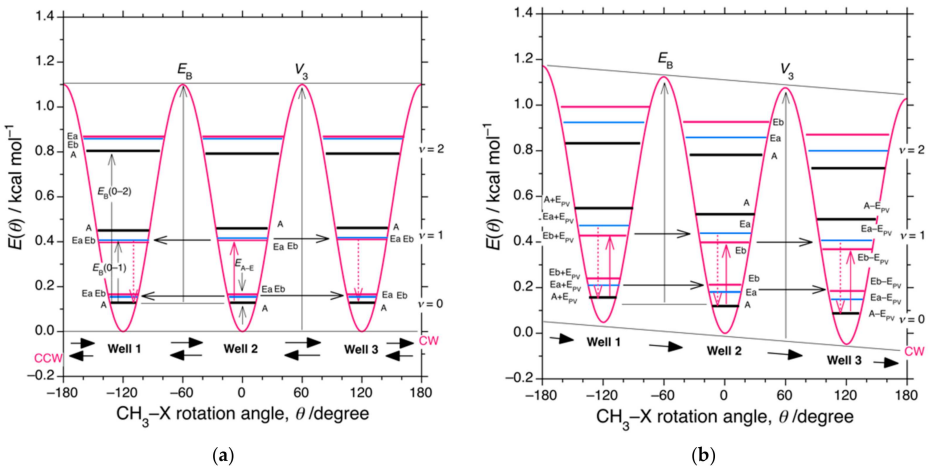

Figure 9. *Cont.*

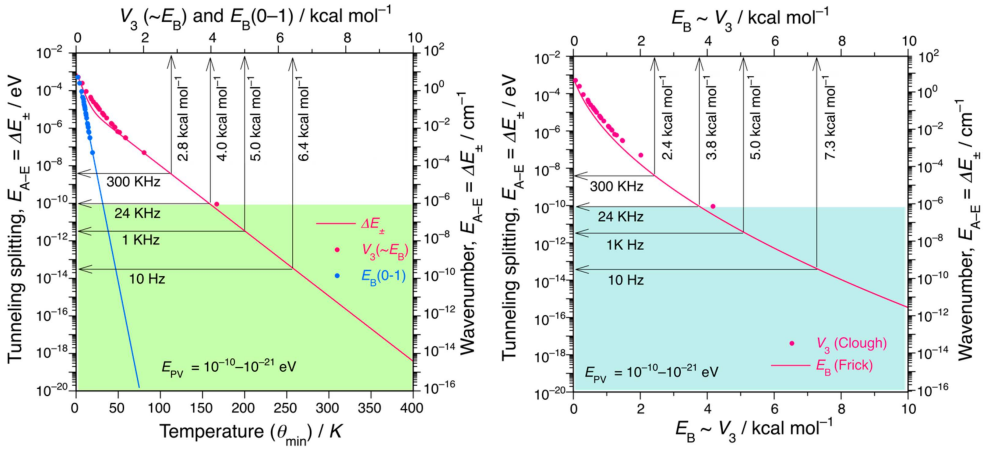

Figure 9. (**a**) Symmetrical potential energy curves as functions of CH_3 rotor angle (θ). $E(\theta) = V_3/2 \cdot \{1 - \cos(3\theta)\}$, $V_3 \simeq E_B$ = 25.2 meV (1.1 kcal mol^{-1}). V_3 data were obtained from nitromethane (CH_3NO_2) [221]. (**b**) Asymmetrical potential energy curve as a function of θ by adding $\pm E_{PV}$ to the A, E_a, and E_b levels. When the E_{PV} term is added and subtracted from the E_a and E_b levels, $E_a \neq E_b$, resulting in several VCD modes of *n*-alkanes. (**c**) A universal correlation curve for CH_3 rotation in coherent tunneling, E_{A-E} (= $\Delta E_\pm$) (in eV), and thermally activated incoherent non-Arrhenius hopping mechanisms as functions of θ_{min} (in K) and $V_3 \simeq E_B$ (in kcal mol^{-1}). Here, E_B (red circles) is the rotational barrier height of CH_3 in the ground state ($v = 0$) and V_3 (blue circles) is the rotational barrier height from the bottom of the wells. θ_{min} was obtained at a reorientation rate of 2×10^8 s^{-1}. An empirical equation, E_{A-E} (in μeV) = $30 \cdot \exp(-0.08 \cdot \theta_{min}) + 10^3 \cdot \exp(-0.28 \cdot \theta_{min})$, was obtained from the analysis of the crystalline molecular solids [221–227]. For readability, $V_3 \sim E_B$ in X_2-axis is added. A similar correlation between E_{A-E} as a function of E_B (in kJ mol^{-1}) has been reported [222,228]. (**d**) Another universal correlation curve of E_{A-E} (= $\Delta E_\pm$) as a function of E_B (kcal mol^{-1}) by analyzing INS spectroscopy in non-crystalline polymers: E_{A-E} (in μeV) = $a \cdot (E_B/b)^{0.75} \cdot \exp[-(E_B/b)^{0.5}]$, a = 1.23 meV, b = 4.30 K [242]. For clarity, red circles are identical to those in (**c**). The green and blue areas in (**c**) and (**d**) suggest the CH_3 rotations due to non-Arrhenius law hopping mechanism, respectively.

3.5.3. Unidirectional CH_3 Rotor Induced by E_{PV}

To address the four symmetry questions raised by Clough [227], the authors would like to mention a toy model of unidirectional CW (or CCW) rotation at a macroscopic level as a low-entropy state. The E_a–E_b degeneracy is "lifted" by an external magnetic field (Zeeman effect), an external electric field (Stark effect), a built-in internal electric field (dipole moment), and possibly Z^0-WNC. When the $E_{A-E} \sim E_{PV}$ condition is satisfied (Scenario D), a handed CH_3 rotating action becomes possible. First, A, E_a, and E_b at well 2, biased by $-E_{PV}$, were postulated. At well 3, $A^*(3) = A - E_{PV}$, $E_a^*(3) = E_a - E_{PV}$, and $E_b^*(3) = E_b - E_{PV}$; conversely, at well 1 biased by $+E_{PV}$, $A^*(1) = A + E_{PV}$, $E_a^*(1) = E_a + E_{PV}$, and $E_b^*(1) = E_b + E_{PV}$.

Figure 9b illustrates the modified potential energy $E(\theta)$ biased by $\pm E_{PV}$ as a function of θ. Because $A(2) \neq A^*(1) \neq A^*(3)$, $E_a(2) \neq E_a^*(1) \neq E_a^*(3)$, and $E_b(2) \neq E_b^*(1) \neq E_b^*(3)$ at ν = 0,1,2.., there is unequal permutational tunneling between three potential wells—well 1, well 2, and well 3—with CW rotation, [well(2) $\rightarrow$ well (3) $\rightarrow$ well(1) $\rightarrow$]$_n$, leading to handed CH_3 rotation at low temperatures. When E_a in well 2 (ν = 0) is coincident with $E_b + E_{PV}$ in well 3 (ν = 0), resonant tunneling endowed with several chiral phonon modes occurs at ν = 0. Similarly, E_b in well 2 (ν = 1) is coincident with $E_a + E_{PV}$ in well 3 (ν = 1), and resonant tunneling with the help of several chiral phonons (from ν = 0 to ν = 1) is possible. Even if non-Arrhenius law hopping is dominant at higher temperatures, handed permutational rotation is likely to occur with a small probability because of the high cooperativity in the condensed phase to minimize the entropy at the macroscopic level.

This assumption can be confirmed by the emergence of several (−)-sign vibrational circular dichroism (VCD) signals at the corresponding IR bands, characteristic of CH_3 rotors and CH_2 skeletal *g*-bonds in several liquid *n*-alkanes, as discussed in Section 3.6.

To determine the relationship between the E_B dependence of the tunneling splitting/frequency ($E_{A–E}$) with a small E_{PV}, two universal correlation curves of $E_{A–E}$ in CH_3 rotation at vibrational quantum number $\nu = 0$ as functions of barrier heights, $V_3 \simeq E_B$ (in kcal·mol^{-1}), E_B (from $\nu = 0$ to $\nu = 1$), and re-orientational temperature, θ_{min} (in K) are compared [222,224–228]. Here, θ_{min} determined by the T_1 measurement of ^{1}H-NMR is a crossover temperature between temperature-dependent quantum tunneling and non-Arrhenius law hopping processes, although the transition appears to be continuous.

Figure 9c shows the $E_{A–E}$ in molecular crystals as functions of θ_{min}, $V_3 \simeq E_B$ (red circles and red line), and E_B(0–1) (blue circles and blue line) [222,224–227], while Figure 9d plots the $E_{A–E}$ obtained in non-crystalline polymers as a function of E_B (red line) [240–244], with red circles taken from Figure 9c [224–226]. The two $E_{A–E}$ vs. E_B correlation curves are very similar, regardless of whether considering crystalline molecular or non-crystalline polymer solids. When the E_B of the CH_3 rotor, $E_B(CH_3)$, varies slightly from 2 to 7 kcal mol^{-1}, the $E_{A–E}$ decreases exponentially from 10^{-7} to 10^{-14} eV, corresponding to 10^{-3} to 10^{-10} cm^{-1} (3×10^7 to 3×10^1 Hz). Consequently, $E_{A–E}$ becomes comparable to the theoretical E_{PV}, and as a result, the $E_{A–E}$ (= $\Delta E_{\pm}$) ~ E_{PV} condition (Scenario D) is experimentally feasible.

The $E_B(CH_3)$ in the crystals ranges from 0.1 to 5 kcal mol^{-1} (50–2500 K, 0.004–0.21 eV, 35–1750 cm^{-1}) [220]. At 4.2 K, the tunneling frequency of CH_3 rotors is ~ 300 KHz for even-carbon number *n*-alkanes including *n*-$C_{12}H_{26}$, and 340 KHz for odd-carbon number *n*-alkanes, including *n*-$C_{13}H_{28}$ [220,232–234]. The two frequencies correspond to $E_{A–E}$ ~ (1.3–1.4) × 10^{-9} eV with $E_B(CH_3)$ ~ 2.8 kcal mol^{-1}. On the other hand, the rotational frequency of $E_B(CH_3)$ directly attached to the main chain of PMMA, which is known as γ–relaxation, is only ~1 KHz (4×10^{-12} eV) below 120 K. The corresponding $E_B(CH_3)$ values in isotactic- and syndiotactic-PMMA are evaluated to be 3.3 kcal mol^{-1} and 6.7 kcal mol^{-1}, respectively [220,240,242].

The liquid *n*-alkanes containing PDBS in the range of −10 °C and 110 °C are likely to obey the $E_{A–E}$–E_B correlation curves in Figure 9c,d. When $E_B(CH_3) \gtrsim 3.8$ kcal mol^{-1}, the $E_{A–E}$ approaches the predicted E_{PV} value of 10^{-10} eV, and when $E_B(CH_3) \gtrsim$ 6.4–7.3 kcal mol^{-1}, the $E_{A–E}$ approaches the E_{PV} value of 10^{-13} eV, as shown by the blue zone in Figure 9d and the green zone in Figure 9c. The rotational frequency of CH_3 rotors in *n*-butyl pendants becomes very small and $E_B(CH_3)$ is likely to be $\gtrsim$ 6 kcal mol^{-1}, which is considerably higher than $E_B(CH_3)$ ~ 2.8 kcal mol^{-1} of *n*-alkanes. Even with a higher $E_B(CH_3)$, the CH_3 rotors of *n*-alkanes and *n*-butyl groups might feel the handed E_{PV} force embedded in the non-Arrhenius law hopping process.

3.6. Are n-Alkanes Optically Active? VCD and IR Spectra of n-$C_{12}H_{26}$, n-$C_{12}D_{26}$, and Other n-Alkanes

3.6.1. Detecting the Gauche Bonds in *n*-Alkanes

The quantum tunneling of CH_3 hinders the rotor in *TP n*-alkanes in the solid state, which is a dominant process at cryogenic temperatures. The CH_3 rotation in odd-number carbon *n*-alkanes (carbon number from 9 to 29) results in non-*TP* conformers involving one and multiple g^+ and g^- bonds above their melting points and liquid states [220,232–234]. As discussed in Section 3.3, our calculated E_B values from *t*- to one/two *g*-bonds of *n*-$C_{12}H_{26}$ are on the order of 3.24 to 5.74 kcal mol^{-1} (Table S1, Supplementary Materials). The production of single, double, and kink g^+ and/or g^--bonds are experimentally detectable by IR and Raman spectroscopy [178,193–198,200–209]. For example, using IR spectroscopy, several characteristic bands, i.e., 873/975/1078/1164/1341 cm^{-1} for end-*g* bonds, 1353 cm^{-1}

for *gg*-bonds, and 1306/1366 cm^{-1} for *g*-*t*-*g** (kinks), respectively, can be recognized when compared to 1378 cm^{-1} for the CH_3 group [178,201–209].

3.6.2. CD/UV Background Spectra of Liquid *n*-$C_{12}H_{26}$

In recent years, Ozaki et al. investigated the electronic transition states of *n*-C_5H_{10} to *n*-$C_{14}H_{30}$ using attenuated total reflection far-ultraviolet (ATR-FUV) spectroscopy and TD-DFT/SAC-CI calculations [245–247]. They assigned several fundamental FUV bands of *TP n*-alkanes: the strongest FUV band around 145 nm was a mixture of HOMO → Rydberg 3*p* and HOMO-1 → Rydberg 3*s* transitions, and the weak shoulder FUV band around 165 nm was assigned to HOMO → Rydberg 3*s*. The major 145 nm and shoulder 165 nm bands should tail to the near-UV region in the range of 250–400 nm, which is seen as a structureless background (Figure S6a, Supplementary Materials). When *n*-alkanes are involved in a non-mirror-symmetric g^+ or g^- geometry, the 165 nm band tails more strongly in the CD/UV region. In fact, *n*-$C_{12}H_{26}$ showed weak temperature-dependent CD and UV spectra even after subtracting the instrumental background at −5 °C, 50 °C, and 100 °C (Figure S6b, Supplementary Materials).

3.6.3. VCD/IR Spectra of *n*-Alkanes

Assuming $g^+ > g^-$ due to the E_{PV} of RH-*GH* in *n*-$C_{11}H_{24}$ [191,192], the CH_3 rotor then has a unique handedness, which is responsible for the transfer of solvent chirality to *n*-butyl pendants and hence the Si main chain. When *n*-$C_{12}H_{26}$ is between −10 °C and T_{C2}, the [(g^+)-$(t)_9$] conformer showing (+)-sign CD as the dominant species strongly induces 300 nm RH-helicity and (+)-sign CD in PDBS. Conversely, when *n*-$C_{12}H_{26}$ is between T_{C2} and T_{C1}, [$(g^+)_2$-$(t)_7$] and [(g^+)-$(t)_9$] as the dominant species induce (−)-sign CD helicity. When *n*-$C_{12}H_{26}$ is above T_{C1}, mutual cancellation between the (+)-and (−)-sign CD in g^+-rotamers results in a lack of any induced MPV effects.

Inspired by the symmetry breakings proposed by Clough [227], if *n*-alkanes without point chirality adopt chiral conformers, VCD and ROA spectroscopy should detect several optically active vibration bands characteristic of the handedness of stretching, bending, rocking, and torsion modes of the CH_3 group, and stretching, bending, and twisting modes for CH_2. The VCD and IR spectra datasets of liquid *n*-$C_{12}H_{26}$ and *n*-$C_{12}D_{26}$ at 10 °C (below T_{C2}), 25 °C (~T_{C2}), and 40 °C (above T_{C2}) are shown in Figure 10a–d and Figures S15 and S16, Supplementary Materials.

Several (−)-sign VCD signals of *n*-$C_{12}H_{26}$ and *n*-$C_{12}D_{26}$ are observed. The VCD spectral profiles are independent of temperature, as shown in Figures S15 and S16 (Supplementary Materials). In line with the handbooks of IR/Raman spectroscopies [248,249], a previous IR study of liquid and solid *n*-$C_{12}H_{26}$ [178,201,250] assigned three major characteristic IR bands at 1466 cm^{-1}, 1456 cm^{-1}, and 1382 cm^{-1}, respectively, to CH_2 (scissoring), CH_3 (asym, bending), and CH_3 (sym, bending or "umbrella"). The *t*- and *g*-bonds in the C–C skeletal IR bands are observed at 1133 cm^{-1} and 1076 cm^{-1}, respectively (Figure 10a). The (−)-sign VCD band at 1088 cm^{-1} (a handed *g*-bond) is rather weak, and the VCD band of the *t*-bond is even less obvious. Although a sharper (−)-sign VCD band characteristic of CH_3 (rocking) is observed at 930 cm^{-1}, the corresponding IR bands around 929 cm^{-1} are very weak. The combination band of CH_3 torsion and CH_2 rocking modes at 1184 cm^{-1} is weak, and the corresponding IR bands are also not obvious.

The (−)-sign VCD band of *n*-$C_{12}H_{26}$ at 1456 cm^{-1}, which is coincident with the 1456-cm^{-1} CH_2 bending IR band, is observed as a shoulder of the 1466-cm^{-1} CH_2 scissoring IR band (Figure 10c). The dissymmetry ratio of the vibration at 1456 cm^{-1}, $g = \Delta Abs/Abs = -1.6 \times 10^{-4}$, could be evidence of the unidirectional CH_3 rotation in *n*-$C_{12}H_{26}$, for example, from the A*-state at $\nu = 0$ to the E_b* (or E_a*)-state at $\nu = 1$. The

multiple (−)-sign VCD bands around 1470 cm^{-1} at the 1456-cm^{-1} CH_2 scissoring IR band and the (−)-sign VCD and IR bands of the *g*-bond at 1088-cm^{-1} are related to the preference of g^+ over g^- bonds.

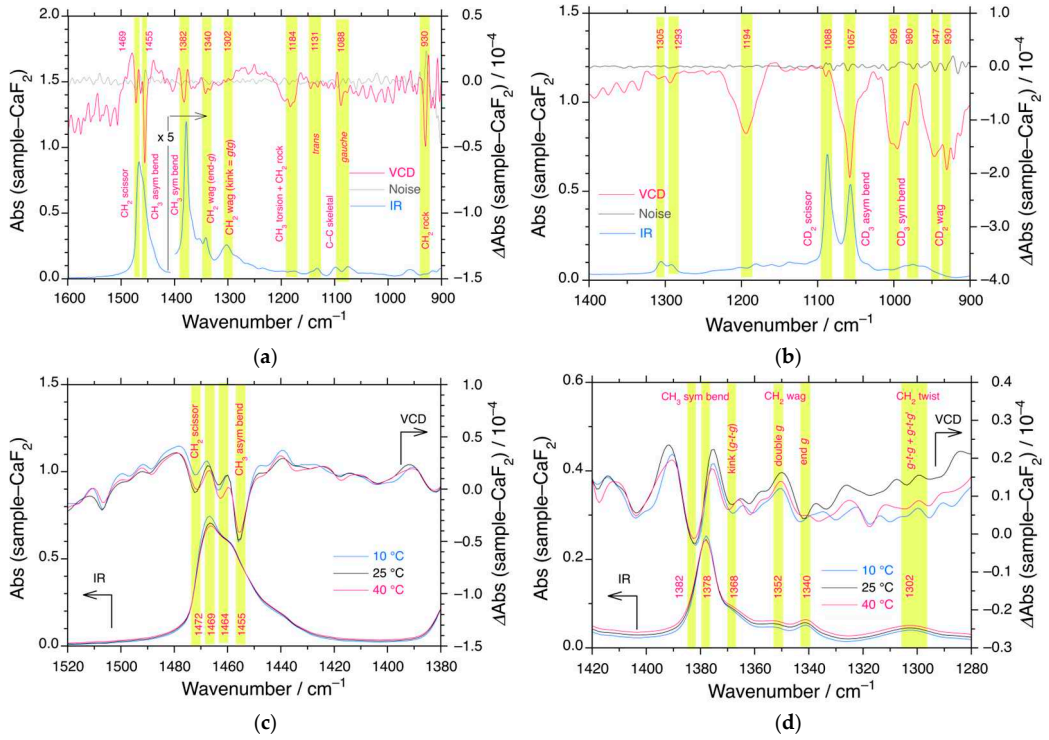

Figure 10. VCD (red) and IR (blue) spectra and VCD background noise (black) (CaF_2 windows) of (**a**) *n*-$C_{12}H_{26}$ at 25 °C in the range of 900 cm^{-1} and 1600 cm^{-1} and (**b**) *n*-$C_{12}D_{26}$ at 25 °C in the range of 900 cm^{-1} and 1400 cm^{-1}. The zoomed-in VCD (red) and IR (blue) spectra of *n*-$C_{12}H_{26}$ at 10 °C (blue), 25 °C (black), and 40 °C (red) (**c**) in the range of 1380 cm^{-1} and 1520 cm^{-1}, and (**d**) 1280 cm^{-1} and 1420 cm^{-1}. The VCD and IR spectra were subtracted from the corresponding raw VCD and IR spectra of the CaF_2 substrate, respectively. For *n*-$C_{12}H_{26}$, the VCD/IR bands at 1469 cm^{-1}, 1455 cm^{-1}, and 1382/1378 cm^{-1} were assigned to CH_2 (scissoring), CH_3 (asym, bending), and CH_3 (sym, bending, "umbrella") modes, respectively. The VCD/IR bands at 1368 cm^{-1}, 1352 cm^{-1}, 1341 cm^{-1}, and 1302 cm^{-1} were assigned to CH_2 wagging (*g*-*t*-*g*, double *g*, end *g*) and CH_2 twisting (*g*-*t*-*g* + *g*-*t*-*g*′), respectively. For *n*-$C_{12}D_{26}$, the VCD/IR bands at 1088 cm^{-1}, 1057 cm^{-1}, 996/980, and 947/930 cm^{-1}, respectively, are assignable to CD_2 (scissoring), CD_3 (asym, bending), CD_3 (sym, bending), and CD_2 (twisting) modes. The yellow areas in (**a**–**d**) indicate the detectable VCD signals relating to the corresponding IR bands, that are the region of interest discussed in the main text.

The VCD and IR spectra of liquid *n*-$C_{12}D_{26}$ can be observed more clearly, as shown in Figure 10b and Figure S16 (Supplementary Materials). Three major IR bands of *n*-$C_{12}D_{26}$ at 1088 cm^{-1}, 1057 cm^{-1}, and 975 cm^{-1} were assigned to the CD_2 (scissoring), CD_3 (asym, bending), and CD_3 (sym, bending, 'umbrella') modes. Notably, the clear (−)-sign VCD band at 1057 cm^{-1} is coincident with the 1057-cm^{-1} CD_3 IR band. The value of $g = -4.0 \times 10^{-4}$ at 1057 cm^{-1} is ~ two times larger than the corresponding 1456-cm^{-1} VCD/IR bands of CH_3 in *n*-$C_{12}H_{26}$. This is evidence of the handed CD_3 rotor in *n*-$C_{12}D_{26}$ being in the same direction as the CH_3 rotor. At the shoulders of several broad IR bands centered at 980 cm^{-1}, three (−)-sign VCD bands centered at 996 cm^{-1} accompanied by several (−)-sign VCD bands centered at 930 cm^{-1} are observed, suggesting the inequality of the CD_3 bending modes. However, the VCD band at the CD_2 (scissoring) IR band at 1088 cm^{-1} is less obvious, indicating no preference between g^+ and g^- bonds.

Similarly, the other five liquids, *n*-C_8H_{18}, *n*-$C_{10}H_{22}$, *n*-$C_{13}H_{28}$, *n*-$C_{14}H_{30}$, and *n*-$C_{16}H_{34}$, at 25 °C revealed several (−)-sign VCD bands in the range 900–1600 cm^{-1},

as shown in Figure S17a–e (Supplementary Materials). Several characteristic VCD/IR bands of CH_2 at 1464–1472 cm^{-1} (scissoring), CH_3 at 1455–1466 cm^{-1} (asym, bending), CH_3 1377–1380 cm^{-1} and 1360–1361 cm^{-1} (sym, bending), and the handed *g*-bonds at 1086–1088 cm^{-1}, respectively, can be seen. The VCD bands due to CH_2 around 1300 cm^{-1} (twisting) and the *t*-bonds in the C–C skeletal IR bands at 1131–1135 cm^{-1} were less obvious. Likewise, the combination band of CH_3 torsion and CH_2 rocking modes at 1172–1184 cm^{-1} was weak, and the corresponding IR bands were less obvious.

3.6.4. VCD, ROA, and Near-IR CD Spectroscopy

The detection of several VCD/ROA bands and high-resolution IENS signals as torsional modes (from $\nu = 0$ to $\nu = 1$) in Figure 9b in the range of 1–350 cm^{-1} might constitute direct evidence of MPV. The asymmetric (~2960 cm^{-1}) and symmetric (~2870 cm^{-1}) stretching modes of the CH_3 group and the asymmetric (~2960 cm^{-1}) and symmetric (~2850 cm^{-1}) modes of the CH_2 group provide additional evidence. Further, several overtones and combination bands, such as the first overtone CH_3 (torsion) at ~620 cm^{-1}, CH_3 (torsion) + CH_3 (asym, bending) at ~1800 cm^{-1}, and CH_3 (torsion) + CH_2/CH_3 (stretching) at ~3300 cm^{-1}, are useful [244].

A near-IR CD spectropolarimeter with an InGaAs detector covering ~1600 nm (~1.29 eV, ~6250 cm^{-1}) allowed the detection of optical activity in the second, third, and fourth overtones of C–H stretching, bending, and their combination bands as liquids as a function of temperature by choosing several path lengths in the range of 10–200 mm and subtracting the background spectra of the cuvette and window glass. The near-IR CD spectra of the CD_3 and CD_2 groups can be compared to those of the third and fourth overtone frequencies, which are reduced by ~$1/\sqrt{2}$.

3.7. Possible Scenarios for the MPV Effects of PDBS with n-Alkanes

Based on the above results and discussion, a possible scenario for the dual mirror-symmetry breaking of PDBS in *n*-dodecane is proposed. As mentioned in the Introduction, pyrromethenes 597 and 546, carrying three CH_3 groups (Chart S1, Supplementary Materials), showed clear (−)-CD spectra in solution at 25 °C [114]. From the temperature-independent (−)-sign VCD spectra of liquid *n*-alkanes, the CH_3 rotor consisting of three ^1H atoms (Q_W = –0.108 × 3 = –0.324) is likely to function as a unidirectional hindered rotor mediated by E_{PV}. The rotor characteristics obey the non-Arrhenius law of hopping at higher temperatures and quantum tunneling at lower temperatures, although there is no critical border and the transition between the two mechanisms is continuous as the temperature changes (Figure 9c,d, and Figure S12, Supplementary Materials). Similarly, the CD_3 rotor consisting of three ^2H atoms prefers CW rotation because of the same (−)-sign VCD bands and a similar magnitude of $g \sim -10^{-4}$ for the symmetric bending modes of CH_3 at 1456 cm^{-1} and CD_3 at 1057 cm^{-1}.

According to the MPV theory for *GH n*-alkanes, the RH helix consisting of all-g^+ bonds is more stable than the LH helix with all-g^- bonds, suggesting that the CH_3 rotor prefers CW rotation. The enantiomeric pairs between the g^+ and g^- bonds and between the g^+g^+ and g^-g^- bonds are energetically unequal. The g^+ and g^+g^+ bonds are in excess of the corresponding g^- and g^-g bonds. The CW-CH_3 rotor generates end-g^+, other g^+, and g^+g^+ bonds in *TP n*-alkanes and *TP n*-butyl pendants. Non-*TP n*-alkanes involving one and multiple g^+ bonds and g^+g^+ bonds thus become optically active chiral solvents, enabling the induction of handed helicity in mirror-symmetrical 7_3-helical PDBS via intermolecular chirality transfer interactions.

To explain the notable H/D isotope effect of T_{C1} evident in the g_{abs}–T curves in Figures 2a and 3b, the relative ratio of θ_D and $\theta_D{}^{rel}$ between *n*-$C_{12}D_{26}$ and *n*-$C_{12}H_{26}$ was

obtained from the asymmetric bending modes of CD_3 (1057 cm^{-1}) and CH_3 (1456 cm^{-1}), yielding $\theta_D{}^{rel}$ = 0.726. $\theta_D{}^{rel}$ predicted a T_{C1} of 274 K (1 °C) for *n*-$C_{12}D_{26}$ when a T_{C1} of 378 K for *n*-$C_{12}H_{26}$ was chosen. Similarly, the ratios of the highest asymmetric/symmetric stretching frequencies between CD_3 (2216/2073 cm^{-1}) and CH_3 (2959/2875 cm^{-1}) [251,252] led to $\theta_D{}^{rel}$ = 0.748/0.721, corresponding to T_{C1} of 282 K (9 °C) and 273 K (0 °C), respectively. The fundamental vibrational modes of these solvent molecules account for T_{C1} as an observable MPV effect. These simple evaluations agree with $T_c \propto \theta_D$ predicted by Salam's theory. In contrast, the (−)-sign Q_w of ^1H and (+)-sign Q_w of ^2H as solvent molecules induced opposite helicity in PDBS below T_{C1} and T_{C2}. The difference in $|g_{abs}|$ is ascribed to the inherent difference in I_{rot} and B between CH_3 and CD_3 rotors, as indicated by the marked reductions in E_{A-E} by two to three orders of magnitude [220,222,235–239].

From Table S1, Supplementary Materials, it is interesting to note that the end g^+ bond, $(g^+)_1$-$(t)_8$, and middle g^+ bond, $(t)_2$-$(g^+)_1$-(t)6, show (+)-sign CD spectra at λ_{ext} of *n*-$C_{12}H_{26}$, whereas the g^+g^+ bond, $(g^+)_2$-$(t)_7$, and other g^+ bonds, like $(t)_1$-$(g^+)_1$-$(t)_7$, show (−)-sign CD effects.

First, intramolecular chirality transfer was considered. (a) When $T < T_{C2}$, the ^{29}Si-driven torque overcomes the CH_3 torque, leading to a (+)-CD Si–Si bond helix in the presence of *n*-$C_{12}D_{26}$; conversely, when $T_{C2} < T < T_{C1}$, the CH_3-rotor driven torque overcomes that of ^{29}Si, leading to a (−)-CD Si–Si bond helix (Figure 11a). On the other hand, below T_{C2}, the CW-CH_3 hindered rotor generates the $(g^+)_1$-$(t)_8$ bond in *n*-$C_{12}H_{26}$ with (−)-sign CD (Figure 11b). When $T_{C2} < T < T_{C1}$, the CW-CH_3 hindered rotor induced $(t)_1$-$(g^+)_1$-$(t)_7$ and $(g^+)_2$-$(t)_7$ rotamers with (−)-sign CD (Figure 11b). Next, intermolecular chirality transfer between *n*-$C_{12}H_{26}$ and PDBS was considered. When $T < T_{C2}$, the $(g^+)_1$-$(t)_8$ rotamer induces a (−)-CD Si–Si helix. In contrast, when $T_{C2} < T < T_{C1}$, the $(t)_1$-$(g^+)_1$-$(t)_7$ and $(g^+)_2$-$(t)_7$ rotamers induced the formation of a (+)-CD Si–Si helix. Another explanation for the observed optical activity of PDBS in *n*-$C_{12}H_{26}$ and *n*-$C_{12}D_{26}$ arises from the opposite Q_w values between the three ^1H isotopes in the CH_3 rotor ($Q_w = -0.108 \times 3 = -0.324$) and the three ^2H isotopes in the CD_3 rotor ($Q_w = +0.892 \times 3 = +2.772$).

Two different CH_3 rotors (I = 3/2, $\mu_N = +2.79 \times 3 = +8.37$) of *n*-$C_{12}H_{26}$ and *n*-butyl of PDBS are schematically illustrated in Figure 11. Because the tunneling frequency and splitting of the CD_3 rotor markedly diminish relative to those of the CH_3 rotor [220,222,235–239], the helix preference of the PDBS in *n*-$C_{12}D_{26}$ is dominantly determined by the relative magnitude and direction of the rotational torques between the two CH_3 rotors and the 4.7% ^{29}Si (I = 1/2, μ_N = –0.55). From NMR experiments, it is known that ^1H and ^{13}C isotopes prefer α-spin (↑), and conversely, ^{29}Si prefers β-spin (↓) by Zeeman splitting under an external magnetic field (H_0). It is possible that ^1H and ^{29}Si induce opposite rotational torque in the absence of H_0.

3.8. Added in Proof—Other Oligo- and Polysilanes for the MPV Validation

To validate the calculated results of the PESs (Figure 8 and Figure S13c–f, Supplementary Materials) experimentally, the CD/UV spectra of permethyldecasilane (PMDS) and poly(diethylsilane) (PDES) (Chart S1, Supplementary Materials) were measured under static conditions. PMDS in *n*-propanol did not exhibit CD effects because of the lower E_B in the tetra-wells (Figure S18a, Supplementary Materials). In contrast, PDES in *n*-propanol, *n*-butanol, and *n*-hexanol showed weak (+)-sign CD effects at longer λ_{ext} values relative to the corresponding UV spectra at shorter λ_{max} values (Figure S18b–d, Supplementary Materials); it is evident that the CD spectral profiles did not match the corresponding UV profiles. The (+)-sign g_{abs} of PDES in *n*-propanol as a function of temperature indicated T_{C1} ~ 30 °C (Figure S18e, Supplementary Materials).

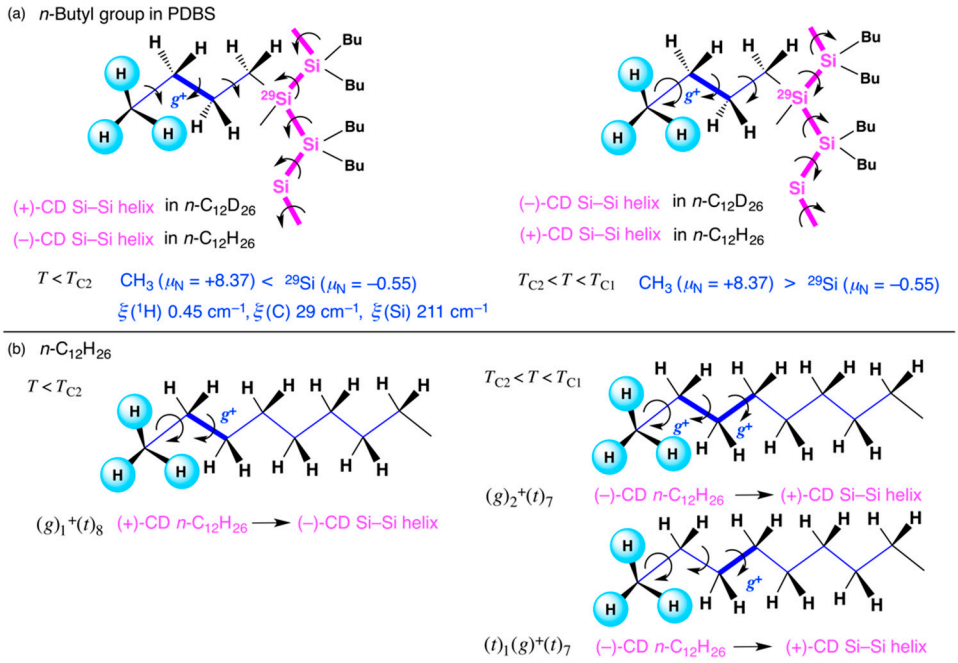

Figure 11. A proposed rationale for nuclear-spin dependent intra- and inter-molecular chirality transfer between two types of CH_3 rotors at the *n*-$C_{12}H_{26}$ and *n*-butyl pendants of PDBS and ^{29}Si isotope of PDBS. The CD_3 rotor in *n*-$C_{12}D_{26}$ diminishes the ability of the hindered rotor relative to that of CH_3 as a result of the heavier isotopes of the three ENSs. First, with respect to intramolecular chirality transfer, (**a**) in the presence of *n*-$C_{12}D_{26}$, when $T < T_{C2}$, the ^{29}Si-driven torque overcomes the CH_3 torque, leading to a (+)-CD Si–Si bond helix; conversely, when $T_{C2} < T < T_{C1}$, the CH_3-rotor driven torque overcomes the ^{29}Si torque, leading to a (−)-CD Si–Si bond helix (**a**). On the other hand, in liquid *n*-$C_{12}H_{26}$, below T_{C2}, the CW-CH_3 hindered rotor generates a $(g^+)_1$-$(t)_8$ bond in *n*-$C_{12}H_{26}$ with (−)-sign CD (**b**). When $T_{C2} < T < T_{C1}$, the CW-CH_3 hindered rotor induces $(t)_1$-$(g^+)_1$-$(t)_7$ and $(g^+)_2$-$(t)_7$ rotamers with (−)-sign CD *n*-$C_{12}H_{26}$ (**b**). Next, intermolecular chirality transfer between *n*-$C_{12}H_{26}$ and PDBS was considered. When $T < T_{C2}$, the $(g^+)_1$-$(t)_8$ rotamer induces a (−)-CD Si–Si helix. In contrast, when $T_{C2} < T < T_{C1}$, the $(t)_1$-$(g^+)_1$-$(t)_7$ and $(g^+)_2$-$(t)_7$ rotamers induced formation of a (+)-CD Si–Si helix.

Prior to the VT-CD/UV spectral measurements of PDBS, PDES, and PMDS in *n*-alkanes, M.F. and J.R.K. at NTT Basic Research Labs in the 1980s and the 1990s were aware of the (−)-sign CD spectra of poly{bis-(*p*-*t*-butylphenyl)silane) (PB*t*BPS) (Chart S1, Supplementary Materials) in tetrahydrofuran (THF) at −10 °C, 25 °C, and 50 °C (Figure S19a, Supplementary Materials), in addition to the weak (−)-sign CD effects of poly(*n*-hexyl-2-methylpropylsilane) (PH2MPS) (Chart S1, Supplementary Materials) in isooctane at 0 °C (Figure S19b, Supplementary Materials). Importantly, the CD spectral profiles at shorter λ_{ext} values do not match the corresponding UV spectra.

In 2018, T.M., M.F., and Dr. Ayako Nakao working at NAIST recognized that PDBS-H in a mixture of *n*-$C_{12}H_{26}$ 98.3%/THF 1.7% (*v*/*v*) under static conditions reveals opposite signed temperature dependent CD spectra in *n*-$C_{12}H_{26}$ at 0 °C, 20 °C, and 45 °C when a small amount (50 μL) of 10^{-3} M THF solution of PDBS-H was added to 2.95 mL of *n*-$C_{12}H_{26}$ (Figure S19c, Supplementary Materials). However, the PDBS-H in pure THF did not exhibit any detectable CD effects at −10 °C. The oxygen atoms of a trace amount of THF coordinate to the Si 3*d* or Si σ* orbitals, resulting in intermolecular C–H/O interactions with the *n*-butyl pendants.

Interestingly, poly(*n*-hexyl-2-ethylbutylsilane) (PH2EBS) (Chart S1, Supplementary Materials) exhibited noticeable solvent and temperature dependence of the CD/UV spectra. The CD spectra of PH2EBS in *n*-$C_{12}H_{26}$ under static conditions are completely opposite to

those in *n*-octanol at the three temperatures (Figure S19d,e, Supplementary Materials). The g_{abs} values at 310 nm as a function of temperature are shown in Figure S19f, Supplementary Materials. Clearly, PH2EBS undergoes a second-order helix–helix transition at T_{C2} ~ 30 °C, which is associated with the oppositely signed CD signals in *n*-$C_{12}H_{26}$ and *n*-octanol. The CD spectrum of PH2EBS in *n*-octanol almost disappears at T_{C1} ~ 110 °C and recovers mirror-symmetric 7_3-helices absorbing at 320 nm. The oxygen atom of *n*-octanol coordinates to the 3*d* orbital or Si σ* of the Si atom and/or stimulates the intermolecular C–H/O interactions with alkyl pendants.

Five other poly(dialkylsilane)s, including poly(methyl-*n*-propylsilane), poly(*n*-pentyl-*n*-propylsilane), poly(di-*n*-pentylsilane), and poly(di-*n*-hexylsilane) (Chart S1, Supplementary Materials), did not induce clear CD spectra in *n*-alkanes, *n*-alkanols, THF, and $CHCl_3$ at 0 °C. However, the authors found very clear CD and CPL spectra for several new polysilanes carrying designed achiral pendants in homogeneous solutions of *n*-alkanols, *n*-alkanes, and *p*-dioxane under static conditions. These results will be submitted elsewhere.

3.9. Other MPV-Related Experimental Studies

Most MPV scientists have sought possible answers to the issue of the origin of homochirality on Earth for the past 150 years: why and how have D-sugars and L-amino acids become the building blocks of our lives? And which deterministic or by-chance mechanism is the origin [1–30]? From the viewpoint of *P*-symmetry violation and *CP*-symmetry invariance in physics, true antipodes of D-sugars and L-amino acids are (L-sugars)* and (D-amino acids)* made up of anti-atoms [11,13,21–24]. The anti-atoms are comprised of anti-*p*, anti-*n*, and e^+, whereas anti-*p* and anti-*n*, respectively, are made of anti-*u* and anti-*d* quarks [11,13,24]. Only e^+ are manifested daily in regulated laboratories and hospitals utilizing short-half-life radioisotopes.

In recent years, synthetic biology, in designing mirror-image enzymes and pharmaceutics by producing non-natural DNA/RNA made up of L-sugars and non-natural proteins building-up D-amino acids, has received considerable attention in biotechnology and life science [253–258]. However, it remains unclear whether natural D- and non-natural L-sugars and natural L- and non-natural D-amino acids and their corresponding oligomers and macromolecules rigorously preserve mirror-image relationships in their structures and functionalities.

A few structural biologists are aware of noticeable differences between non-natural L- and natural D-RNA oligomers [259–262]. Single-strand RNA is classified as a floppy macromolecular rotamer with rotational and flip-flop freedom along C–C/C–O/C–N single bonds. When it produces a double-strand, there is a concomitant loss of freedom. In 2004, Betzel et al. reported clear dissimilarity between L- and D-RNA duplexes by crystallographic analysis: L-RNA adopts two types of helical duplexes with head-to-tail packing; conversely, D-RNA adopts a Watson–Crick type with an end-to-end duplex with a wobble-like pair. The discrepancy is ascribed to inherent differences in nature between D-ribose and L-ribose based on MPV calculations of D-ribose [259–262]. Subsequently, they reported other evidence, namely the different intensities of two Raman bands, at 1000 cm^{-1} and 1700 cm^{-1}, between D- and L-RNA. The differences in intensity are ascribed to differences in the electronic levels between the D- and L-RNAs. Rypniewski et al. and Bolik et al. stated that the notable dissimilarity between D- and L-RNA crystals originates from the PVED-WNC of DL-ribose [259–262]. As an alternative explanation, phosphate $O{=}PO_3^-$ with one HINS ^{31}P atom (natural abundance: 100%) has a very large ξ = 475 cm^{-1} [= P (247 cm^{-1}) + 4 × O (57 cm^{-1})] and works as a unidirectional rotor along P–O–C bonds, leading to dissimilarity between the D-/L-RNA.

Compared to D-/L-RNA, the MPV effect of L-/D-amino acids has a long history. In 1973, Garay et al. were the first to report the differences in positronium (Ps) annihilation characteristics between five kinds of L- and D-amino acids using e^+ as a probe [263]. Note that Ps generates two e^+-e^- species of singlet (I = 0, *para*-Ps) with a shorter half-life ($\tau_s \sim 2{\cdot}10^{-10}$ s) and triplet (I = 1, *ortho*-Ps) with a longer half-life ($\tau_t \sim (5–40){\cdot}10^{-9}$ s) in a 1-to-3 statistical ratio. The population of *ortho*-Ps relative to *para*-Ps is directly related to the annihilation intensity of *ortho*-Ps. Among the five DL pairs of amino acids, the annihilation intensity of *ortho*-Ps in L-amino acids was 6–33% weaker than that of the corresponding D-amino acids. D-Amino acids have greater free volumes and lower specific densities than L-amino acids. Although further clarification is needed, this astonishing result implies violations of *CP*- and *P*-symmetries between natural L- and non-natural D-*α*-amino acids. This means a violation of *T*-symmetry invariance between L- and D-*α*-amino acids.

Inspired by Salam's hypothesis [107,108], in the early 2000s, Wang et al. reported differences between D-L-*α*-alanine crystals using VT solid-state ^{13}C-/^{1}H-NMR, Raman spectroscopy, magnetic susceptibility, and DSC from room temperature to cryogenic temperatures [96,97]. An independent research team, however, did not observe such significant differences and ascribed the differences to unresolved impurities imbedded in non-natural D-alanine [264]. If Wang's results are correct, IENS tunneling spectroscopy will detect differences in the CH_3 rotor between D- and L-*α*-alanine crystals at 4 K because the D-L chirality is unchanged. Recently, Bordallo et al. reported dissimilarity between crystalline L- and D-*α*-alanine by VT-polarized Raman spectroscopy and neutron diffraction [265] but had many debates regarding their results [266,267].

In 2021, Koralewski et al. reported that H_2O commonly shows (+)-sign-specific Verde constants at 546.1 nm in magneto-optical rotatory dispersion (MORD) spectroscopy at 291 K [268]. However, they ascribed the unexpected results to metal ion contamination, although L-*α*-threonine (CH_3) and L-*α*-leucine (isobutyl) had particularly large (−)-sign specific Verde constants. The anomaly can be connected to the handed CH_3 rotor action, although the handedness will depend on the solution temperature, pH, *ortho*-/*para*-H_2O ratio, and H_2O/D_2O ratio.

In 2006 and 2013, Romalis et al. reported nuclear-spin-induced optical rotation (NSOR) with (+)-sign rotation of 1–13 μrad·cm^{-1}·M^{-1} (0.06–0.7 mdeg·cm^{-1}·M^{-1}) at 405 nm under B_0 = 5 G of achiral molecular liquids carrying CH_3 and $C^{19}F_3$ rotors, i.e., methanol, ethanol, *n*-propanol, isopropanol, *n*-hexane, *n*-hexene, and perfluoro-*n*-hexane when the liquids were placed in a 0.85 T permanent magnet based on the early work with ^{129}Xe [144,145]. Interestingly, even H_2O exhibits a weak NSOR. The results suggest a nuclear-spin-dependent *PV*-MAM phenomenon because the organic molecules adopt chiral and/or helical geometries owing to the rotors. An enantiomeric pair of liquid molecules carrying CH_3 and $C^{19}F_3$ revealed clear differences in absolute magnitude with the same or opposite signs of NSOR signals.

In 2015, Pandey et al. reported non-mirror-symmetric Cu^{2+} metal organic framework (MOF) crystals coordinated to D- and L-leucine derivatives [269]. The D- and L-homochiral Cu^{2+}-MOFs revealed structurally distinct crystal packing, leading to notable difference in proton conductivity: the L-MOF showed significantly higher conductivity than the D-MOF. The D- and L-leucine residues induce mirror-symmetry-breaking MOFs differently, presumably leading to observable MPV functionality. The handedness of multiple CH_3 rotors due to the isopropyl groups of the D-L-leucine residues is responsible for the non-mirror MOF crystals.

Recently, to validate Salam's hypothesis [107,108], Kozlova et al. designed a new MOF crystal incorporating diamagnetic Zn^{2+}, diazabizyclooctane (DABCO), and terephthalate. DABCO, a two-fold symmetric hindered rotor, can exist as a mixture of LH and RH ge-

ometries [109–112]. The DABCO-Zn^{2+} MOF revealed three second-order phase transitions at 130 K (terephthalate), 60 K (DABCO), and 14 K (DABCO) from specific heats using adiabatic calorimetry and the solid-state ^{1}H-NMR T_1 value. The two transitions at 60 K and 14 K are ascribed to the structural transition of DABCO due to the dynamic Jahn–Teller effect of DABCO, whereas the transition at 130 K arises from the structural transition of BDC^{2-}. A LH–RH preference at 60 K and 14 K of the MOF is not characterized because neither the calorimeter nor ^{1}H-NMR are chiroptical approaches [109–112]. It is interesting to note that the existence of two transitions of the MOF is very similar to that of T_{C1} and T_{C2} of PDBS in *n*-alkanes.

3.10. Perspectives

3.10.1. Is Parity Conserved Under the Gravitational Force?

From the non-mirror CD spectra of PDBS in *n*-alkanes in the CW and CCW flow, it is unclear whether the *P*-symmetry of GF is rigorously preserved. In materials science, CW and CCW flow under the GF has recently been recognized as a local *PC*-EMF event enforced by mirror-symmetrical hydrodynamics [3,169–175]. The hypersensitive hydrodynamic force under the GF is likely to break *P*-symmetry in response to a tiny local *PV* advantage factor and nuclear spin frustration beyond the *P*-symmetric Coriolis force [3,169–175]. To account for the non-mirror characteristics of the CW and CCW flow experiments, the authors came across a research community of *PV*-GF.

The general relativity theory of GF formulated by Albert Einstein in the early 20th century relies on a uniformly accelerated reference frame that conserves *P*-symmetry [270–291]. Since 1964, many researchers have theoretically discussed *PV*-GF: do LH- and RH-chiral objects placed in curved spacetime follow equally geodesic trajectories [274–276]? The possibility of theoretical and experimental breakthroughs in gravitational wave theory owing to differences between LH and RH polarization modes has prompted several experiments to validate the *PV*-GF hypothesis.

For *PV*-GF testing, researchers often use the Eötvös ratio, $\eta = 2{\cdot}(a_A - a_B)/(a_A + a_B) \simeq (m_g/m_i)_A - (m_g/m_i)_B = \Delta(A, B)$, which is similar to Kuhn's dissymmetry ratios, g_{abs} and g_{lum}, where a_A and a_B are the accelerations of two free-falling bodies *A* and *B*, and m_g and m_i are their gravitational and inertial masses, respectively [272]. Similar to the subtle E_{PV} of MPV theories, a tiny Eötvös ratio, η, in the *PV*-GF is estimated to be $\eta = 10^{-15}$–10^{-21} eV and the spin-gravity coupling constant is $|A_{sg}| = 10^{-18}$–10^{-22} eV [272]. To validate the *PV*-GF hypothesis on Earth, a precision rotational torsion pendulum under magnetic shielding at cryogenic temperature has been designed [270–273]. Carefully designed experiments to search for *PV*-GF have been proposed utilizing spin-particles, such as polarized e^- [277–279], a pair of HINS isotopes and a pair of HINS-INS isotopes (i.e., ^{85}Rb-^{87}Rb, ^{39}K-^{87}Rb, ^{87}Sr-^{88}Sr, ^{129}X-^{131}Xe) [280–284], different masses and densities in Ti-Pt alloys [285,286], *l*- and *d*-quartz [287], nuclear-spin-induced chiral molecules [88,288,289], and nuclear-spin-independent chiral CHBrClF and helical H_2X_2 (X = O, S, Se, Te, Po) [290,291]. From his essay, it seems that Shinitzky might have been aware that subtle but detectable differences in density (specific gravity) and optical rotation between L- and D-molecular liquids and between L- and D-$NaClO_3$ crystals, stem from the handedness of the spatiotemporal galaxy and universe [103].

In 2008, 2015, and 2024, Bargueño et al. discussed the importance of nuclear spin dependence when enantiomers experienced *PV*-GF [88,288,289]. Molecules possessing CH_3 rotors are candidates to investigate the magnitude of the *PV*-GF on Earth. The role of the CH_3 rotor in the CW and CCW flow of *n*-alkanes on a macroscopic scale is to dynamically drive the CH_3 rotor and generate $g^+ > g^-$ (or $g^+ < g^-$) bonds by chirally sheared intra- and

intermolecular interactions between *n*-alkane molecules. PDBS is a chiroptical probe that responds to the dynamic behavior of *n*-alkanes. The external hydrodynamic CW and CCW flow at 400–800 rpm (7–15 Hz) results in non-mirror-image CD spectra of PDBS in *n*-alkanes. Organic solvents with CH_3 rotors are likely to feel sensitively the coupling between the EMF and GF. Enantiomeric pairs of terpenes with multiple CH_3 rotors, such as limonene, pinene, carvone, and camphor, are thus candidates as rotating torsional pendulum chemical probes. Actually, noticeable non-mirror-image CD spectra under CW and CCW stirring were found when two optically active aggregates of π-conjugated polymers were stirred in the presence of (*S*)- and (*R*)-limonene carrying two CH_3 rotors [292,293].

3.10.2. Olfactory Receptors Discriminate Between CH_3 and CD_3 Groups of Molecules

One might be aware of the fact that the CH_3 group is ubiquitous in homochiral biomolecules such as lipids, L-amino acids (alanine, threonine, cysteine, valine, leucine, isoleucine, methionine), and thymine. In contrast, no CD_3-containing natural compounds have been detected. Actually, it was demonstrated that olfactory receptor proteins (ORPs) of fruit flies (*Drosophila melanogaster*) at 25 °C and honeybees (*Apis mellifera*) favor acetophenone-h_8 and *n*-octanol-h_{17} but disfavor acetophenone-d_3 (Me), -d_5 (Ph), -d_8 (Me and Ph), and *n*-octanol-d_{18} [294,295]. Interestingly, the fruit flies could not discriminate between benzaldehyde-h_8 and -d_8, presumably because of the lack of a CH_3 group. These odorants might therefore exist as racemic mixtures of rotamers due to the lack of rigid chirality.

To explain the discrimination capability of H-D isotopomers, a molecular vibration theory of olfaction has been proposed in addition to the traditional molecular shape theory of fitting odorant molecules in pocket-shaped ORPs, which belongs to classical biology [296]. However, the vibration theory neglects the CH_3 rotor dynamics of achiral odorants. Recently, quantum smell theories for ORPs have been proposed in quantum biology in terms of the asymmetric DWP and MPV of enantiomeric odorants [297,298]. Sensing odorant chirality is influenced by quantum tunneling between enantiomers in double-well potential. This theory led to the conjecture that the handed CH_3 rotor dynamics of odorants are crucial to ORPs. The hidden handedness of the CH_3 and CD_3 rotors and the handed intermolecular chirality transfer affect the discrimination capability of ORPs. The MPV hypothesis thus shines a light on a new horizon in quantum biology [299].

3.10.3. Candidates of the Handed Rotors

Non-radioactive non-rare molecules containing HINS isotopes, e.g., ^{1}H (I = 1/2), ^{11}B (I = 3/2), ^{13}C (I = 1/2), ^{15}N (I = 1/2), ^{17}O (I = 5/2), ^{19}F (I = 1/2), ^{31}P (I = 1/2), ^{29}Si (I = 1/2), ^{33}S (I = 3/2), $^{35/37}$Cl (I = 3/2), $^{79/81}$Br (I = 3/2) and ^{127}I (I = 5/2), can be utilized to investigate nuclear-spin-dependent MPV and *PV*-GF hypotheses in odd-number wells. Several three-fold rotors, that is, CH_3, CF_3, NH_3^+, and SO_3^- as pendants and BF_4^-, NH_4^+, and $O{=}PO_3^{3-}$ as counter ions, can be introduced into various chromophores/luminophores and solvents. VCD/IR [300], ROA/Raman [300], THz (microwave) CD [301–303], and cavity-ring-down ORD/CD spectroscopy [304,305] allows the characterization of the simplest molecules with C_{3v} symmetry, i.e., CH_3X (X = CN, NC, ^{2}H, ^{19}F, $^{35/37}$Cl, $^{79/81}$Br, ^{127}I) and CHX_3 (X = ^{19}F, $^{35/37}$Cl, $^{79/81}$Br, ^{127}I), by probing the C–H stretching and bending bands in CHX_3 and the asymmetric and symmetric bending bands of CH_3 in CH_3X [306–314]. When the NH_3^+ group in zwitterionic species of L-amino acids acts as a handed rotor in *ortho*- and/or *para*-H_2O, L- and D-amino acids are no longer enantiomeric, which could provide a possible answer to biomolecular handedness on Earth. To our knowledge, time-dependent MPV theories that treat HINS isotopomers in odd-number wells, including three-, five-, seven-, and nine-wells, are rare or have not yet been reported because most MPV theories deal with even-number wells, typically DWP, in the ground state.

Simpler small molecules containing three-fold symmetric rotors in the absence of rigid chemical chirality, that is, methanol, ethanol, *n*-propanol, isopropanol, di-*n*-propyl ether, *n*-butane (a minimal *g*-bond), methylcyclohexane, zwitterions (glycine, *β*-alanine, and choline), acetaldehyde, acetone, diacetyl, *t*-butyl methyl ether, acetic acid, toluene, *p*-cymene, *o*-/*m*-/*p*-xylenes, several terpenes (i.e., geraniol, nerol, *α*-terpinene, *γ*-terpinene), and, for comparison, their ^{2}H, ^{13}C, and ^{15}N isotopomers are commercially available candidates.

Particularly, it is vital to validate the generality of whether other three-fold symmetric rotors, such as $C^{19}F_3$ in *n*-C_4F_{10}, *n*-C_6F_{14}, *n*-C_8F_{18}, 2,3,3,3-tetrafluoropropene, and fluorinated myristic acid generate non-mirror molecules and vibrational spectra [315–320]. The VCD/IR spectra of *n*-C_6F_{14} and *n*-C_8F_{18}, which are molecular models of 13_6- and 15_7-helical poly(tetrafluoroethylene) [321–323], are shown in Figure S20a,b (Supplementary Materials), respectively. Hence, (−)-sign VCD signals due to the CF_3 symmetric stretching modes at 1335 cm^{-1} (*n*-C_6F_{14}) and 1347 cm^{-1} (*n*-C_8F_{18}) can be observed. Additionally, several (−)-sign VCD signals due to the CF_2 asymmetric and symmetric stretching modes are observed in the range of 1265–1150 cm^{-1}.

The nuclear-spin-dependent VCD/IR spectra of the methyl groups in C_{3v} symmetric CH_3CN and CD_3CN are compared in Figure S20c,d (Supplementary Materials), respectively. The VCD/IR spectra of CH_3CN clearly show several broader VCD bands due to the CH_3 group around ~1400 cm^{-1} including sharper asymmetric bending (ν_6) at 1442 cm^{-1} and symmetric bending (ν_3) at 1378 cm^{-1} [307,324]. The broad VCD/IR bands are ascribed to anti-parallel dimers, tetramers, hexamers, and octamers [307,324]. However, CD_3CN showed less obvious VCD signals in the CD_3 group. Further, the VCD/IR spectra of monomeric CH_3CN/CD_3CN species in the gas phase and/or in a dilute solution in $C^{35/37}Cl_4$ will provide direct evidence of intermolecular hindered rotation transfer with handedness.

Another example is the comparison between toluene-h_8 and toluene-d_8, which are the simplest methyl-substituted aromatics. The nuclear-spin-dependent VCD/IR spectra are shown in Figure S20e,f (Supplementary Materials), respectively. Previously, polycrystalline samples of partially and fully deuterated toluene ($C_6D_5CH_3$ and $C_6D_5CD_3$) at cryogenic temperatures clearly showed INS spectra and well-resolved Raman scattering (<140 cm^{-1}) due to the hindered rotation of methyl groups in the TWP [220,325,326]. The (−)-sign VCD band of the C=C stretching mode at 1494 cm^{-1} of toluene-h_8 is obvious, although the VCD bands of CH_3 bending modes (1456 and 1378 cm^{-1}) are weak, as is evident in Figure S20e (Supplementary Materials). Two intense (−)-sign VCD signals (1941 and 1858 cm^{-1}) at four weaker IR bands (1941, 1858, 1800, and 1731 cm^{-1}), which are unique overtone characteristics of monosubstituted benzene derivatives, are clearly observed [249,325,326]. However, the corresponding VCD signals of toluene-d_8 in the range of 1300–1400 cm^{-1} range are very weak (Figure S20f, Supplementary Materials). The VCD-active IR modes are likely to be enhanced as overtones due to effective coupling of the two fundamental vibrational modes of toluene-h_8 [326].

Notably, *p*-cymene (4-isopropyltoluene), which is an aromatic monoterpene, exhibited clear VCD signals in the corresponding IR spectra (Figure S20g–i, Supplementary Materials). The two intense (−)-sign VCD signals (1941 and 1800 cm^{-1}) at two weaker IR bands (1941 and 1800 cm^{-1}), are overtones characteristic of 1,4-substituted benzene derivatives [249]. Conversely, a number of intense (+)-sign VCD signals at the corresponding IR bands in the range of 1000–1550 cm^{-1} are clearly detected, i.e., C–H(CH_3) wagging mode at 1514 cm^{-1}, isopropyl symmetric and asymmetric bending modes (1382 and 1363 cm^{-1}) and *p*-substituted skeletal mode (1057 cm^{-1}) [327]. Because *p*-cymene is often used as a ligand

in various ruthenium complexes, its optically active vibrational modes may be crucial for catalytic activity.

The calculated results can be readily validated using commercial and homemade VCD, ROA, and near-IR CD spectrometers. A theoretical and experimental understanding of the generality of the handedness of perpetual molecular rotors will allow the synthesis of both RH- and LH-chiral molecules and/or helical polymers without chiral catalysts with minimal energy, time, and cost in the near future.

4. Conclusions

Since the 1960s, many theorists have argued that the electroweak force (EWF) induces a parity-violating energy difference (E_{PV}) on the order of 10^{-10}–10^{-21} eV between mirror-image molecules induced by the handedness of the weak neutral electron current (WNC). The six major theoretical scenarios are as follows: (i) linear amplification model ($E_{PV} \propto N$), (ii) $E_{PV} \propto Z^5$ (Z: atomic number), (iii) nonlinear amplification model, (iv) tuning $\Delta E_{\pm}$ to adjust E_{PV}, (v) $E_{PV} \propto \Delta E_{ST}$, and (vi) nuclear-spin-induced anapole moment. In 1991/1992, Salam predicted that non-natural D-amino acids should undergo an EWF-origin *P*-symmetry violating second-order phase transition at 250 K (–23 °C) but that natural L-amino acids would not.

Inspired by Salam's hypothesis and other theoretical MPV approaches, the present work investigates the detailed CD and CPL spectroscopic characteristics of rod-like poly(di-*n*-butylsilane) (PDBS) in homogeneous solutions of *n*-alkanes and isooctane ranging from −10 °C to 110 °C under static conditions, and, for comparison, under clockwise (CW) and counterclockwise (CCW) stirring conditions. PDBS adopts mirror-symmetric 7_3-helices in *n*-hexane and in the solid state.

This paper reports the serendipitous finding of dual mirror-symmetry breaking in PDBS: second-order phase transitions as a result of chiroptical generation at T_{C1} ~ 105 °C, and chiroptical inversion due to a helix–helix transition at T_{C2} ~ 28 °C. In particular, the solvent *n*-dodecane-h_{26} induced a gigantic enhancement in the CD and CPL spectra of PDBS. A (−)-sign CD band newly emerged at a shorter λ_{max} (300 nm) below T_{C1}, followed by a helix–helix transition at T_{C2}, and eventually exhibited g_{abs} = +1.3 × 10^{-2} at −10 °C. In a similar manner, (−)-sign CPL at 60 °C exhibited g_{lum} = –0.7 × 10^{-2} at λ_{em} 340 nm but was inverted to (+)-CPL with g_{lum} = +2.0 × 10^{-2} at 0 °C. Notably, in *n*-dodecane-d_{26}, these g_{abs} values are weaker by an order of magnitude at the lower T_{C1} and associated with opposite CD signs.

The notable H/D effects between *n*-dodecane-h_{26} and -d_{26} led to the proposal that the three-fold symmetrical CH_3 groups of *n*-dodecane and the *n*-butyl pendants of PDBS work cooperatively as a unidirectional perpetual hindered rotor with handedness owing to three non-vanishing nuclear spin-1/2 systems in a triple-well potential. The CD_3 group is an inefficient hindered rotor compared to the CH_3 group because of the inherent difference in the moments of inertia and rotational constants between the CD_3 and CH_3 rotors. Several (−)-sign VCD signals characteristic of the asymmetric and symmetric bending modes of CH_3/CD_3, scissoring and twisting modes of CH_2/CD_2, and *gauche*-bonds of *n*-dodecane-h_{26} were detected.

More interestingly, CW and CCW stirring in several *n*-alkanes at 0–40 °C induced completely non-mirror-image CD spectra of PDBS, which is consistent with the coupling of EWF with gravitational force, and which causes apparent *P*-symmetry breaking on Earth. The handedness of the CH_3 rotor may provide a possible answer to the issue of the missing link of handedness at all hierarchical levels, ranging from LH–ν_e, LH quarks, optically active atoms, biological proteins, DNA/RNA, homochiral living biospheres, and cosmological dextrorotatory rotation. Several handed molecular rotors of three identical

nuclear spin-1/2 atoms in a triple-well potential could allow the future synthesis of RH- and LH-chiral molecules and/or helical polymers by optimizing achiral solvents at specific temperatures in the absence of conventional chemical chirality.

Several experimental studies that may provide evidence for the MPV hypothesis have been introduced and briefly discussed. A dozen of the simplest molecules carrying handed rotors without point chirality were proposed to verify the MPV hypothesis.

The term "chirogenesis" in the title was coined by Victor Borovkov and Yoshihisa Inoue in supramolecular chemistry and materials chemistry, based on the nuclear-spin-independent *PC*-EMF [328–331]. Nuclear-spin-dependent chirogenesis may be widely applicable to *PV*-EWF in general chemistry, a range of spectroscopy, molecular dynamics and molecular mechanics, materials science, quantum dynamics and quantum mechanics, particle physics, atomic physics, molecular physics, biology, astronomy, gravity theory, and cosmology.

5. Experimental Section

The synthesis and characterization of the monomers and polymers are summarized in the Supplementary Materials. All solvents were used as received. Instrumentation and analysis of NMR (^{1}H, ^{13}C, ^{29}Si), VT-CD/UV, VT-CPL/PL, VT-VCD/IR spectroscopic data, and Gaussian 09 calculations obtained with PM3MM, DFT (B3LYP with 6-31G(d) basis set), and TD-DFT(B3LYP with 6-31G(d) basis set) are described in the Supplementary Materials. PB*t*BPS was synthesized by Wurtz-coupling of the corresponding diaryldichlorosilane [332]. PH2MPS and PH2EBS were synthesized by Wurtz-coupling of *n*-hexyl-2-methylpropyldichlorosilane and *n*-hexyl-2-ethylbutyldichlorosilane, respectively [106,333].

Supplementary Materials: The following supporting information can be downloaded at: https://www.mdpi.com/article/10.3390/sym17030433/s1, Chart S1: The chemical structures of nine polysilanes, one oligosilane, and pyrromethenes 546 and 597; Chart S2: Three tridecasilane derivatives, tridecagermane derivative, and *n*-dodecane were studied theoretically using Gaussian 09; Figure S1: ^{1}H-, ^{13}C-, and ^{29}Si-NMR spectra of PDBS-H in $CDCl_3$; Figure S2: ^{1}H-, ^{13}C-, and ^{29}Si-NMR spectra of PDBS-L in $CDCl_3$; Figure S3: ^{1}H-NMR spectrum of PMDS and PDES in $CDCl_3$; Figure S4: GPC chart of PH2EBS, ^{13}C-NMR spectrum of *n*-hexyl-2-ethybutyldichlorosilane in $CDCl_3$, ^{29}Si-NMR spectrum of *n*-hexyl-2-ethybutyldichlorosilane in $CDCl_3$, ^{13}C-NMR spectrum of PH2EBS in $CDCl_3$, and ^{29}Si-NMR spectrum of PH2EBS in $CDCl_3$; Figure S5: CD and UV spectra of PDBS-L in isooctane, *n*-C_8H_{18}, *n*-$C_{10}H_{22}$, *n*-$C_{12}H_{26}$, *n*-$C_{14}H_{30}$, and *n*-$C_{16}H_{34}$ at 0 °C, 20 °C, and 40 °C, and the g_{abs} value at 300 nm as a function of the carbon number of *n*-alkanes at 0 °C, 20 °C, and 40 °C; Figure S6: Raw CD and UV spectra of PDBS-H in *n*-$C_{12}H_{26}$ at three temperatures under static condition, including sample solution with a quartz cuvette subtracted from J-820 instrumental background, neat solvent with quartz cuvette subtracted from J-820 instrumental background, subtracted spectra, and a CD baseline of zero at 400 nm; Figure S7: CD and UV spectra of PDBS-H in *n*-$C_{11}H_{24}$ at 0 °C, 20 °C, and 40 °C and *n*-$C_{14}H_{30}$ at 7 °C, 40 °C, and 60 °C under static conditions; Figure S8: Specific volumes ($cm^3 \cdot g^{-1}$) of *n*-$C_{11}H_{24}$ and *n*-$C_{12}H_{26}$ as a function of temperature; Figure S9: Histograms of eight and three independent CPL measurements of PDBS-H excited at 300 nm in *n*-$C_{12}H_{26}$ at 25 °C (~T_{C2}) and 60 °C (>T_{C2}), respectively; Figure S10: CD/UV spectra of PDBS-L under static and CW, and CCW stirring conditions in *n*-$C_{12}H_{26}$ at 20 °C, *n*-$C_{13}H_{28}$ at 20 °C, *n*-$C_{13}H_{28}$ at 40 °C, *n*-$C_{14}H_{30}$ at 20 °C, *n*-$C_{14}H_{30}$ at 40 °C, *n*-$C_{16}H_{34}$ at 20 °C, and *n*-$C_{16}H_{34}$ at 40 °C; Figure S11: CD/UV spectra of PDBS-L in *n*-$C_{12}H_{26}$ at 0 °C (<T_{C2}), 20 °C (~T_{C2}), and 40 °C (>T_{C2}) under static, CW, and CCW stirring at 1200 rpm; Figure S12: Schematic diagrams of racemization time in T_{rac} as a function of E_B; Figure S13: Potential energy surfaces as a function of the main chain dihedral angle obtained using PM3MM and DFT (B3LYP with 631Gd basis set, including H-$(SiH_2)_{13}$-H, Me-$(SiMe_2)_{13}$-Me, Et-$(GeEt_2)_{13}$-Et, and *n*-$C_{12}H_{26}$; Figure S14: Simulated CD and UV spectra including three singlet and three triplet states,

dipole moments, and graphical geometries of ten conformations of *n*-$C_{12}H_{26}$; Figure S15: VCD and IR spectra of *n*-$C_{12}H_{26}$ at 10 °C, 25 °C, and 40 °C; Figure S16: VCD and IR spectra of *n*-$C_{12}D_{26}$ at 10 °C, 25 °C, and 40 °C; Figure S17: VCD and IR spectra at 25 °C of *n*-C_8H_{18}, *n*-$C_{10}H_{22}$, *n*-$C_{13}H_{28}$, *n*-$C_{14}H_{30}$, and *n*-$C_{16}H_{34}$; Figure S18: CD and UV spectra of PMDS in *n*-propanol at –10 °C, PDES in *n*-propanol at −10 °C, 10 °C, and 30 °C, PDES in *n*-butanol at 0 °C and 20 °C, PDES in *n*-hexanol at –10°C and 0°C, g_{abs} at 315–319 nm of PDES in *n*-propanol as a function of temperature; Figure S19: CD and UV spectra of PB*t*BPS in THF at −10 °C, 25 °C, and 50 °C, PH2MPS in isooctane at 0 °C, PDBS-H in a mixture of *n*-$C_{12}H_{26}$ 2.95 mL and THF 0.05 mL at 0 °C, 20 °C, and 45 °C, PH2EBS in *n*-dodecane at 20 °C, 30 °C, and 105 °C, PH2EBS in *n*-octanol at 0 °C, 20 °C, and 45 °C, g_{abs} at 310 nm of PH2EBS in *n*-$C_{12}H_{26}$ and *n*-octanol as a function of temperature; Figure S20: VCD and IR spectra at 25 °C of *n*-C_6F_{13}, *n*-C_8F_{17}, CH_3CN, CD_3CN, toluene-h_8, toluene-d_8, and *p*-cymene (4-isopropyltoluene); Table S1: Comparisons of relative energy, dipole moment, and CD sign at λ_{ext} of ten rotamers in *n*-$C_{12}H_{26}$.

Author Contributions: Conceptualization, M.F.; methodology, M.F.; validation, M.F., T.M., and M.M.A.; formal analysis, M.F., T.M., and M.M.A.; investigation, T.M., M.F., J.R.K., and M.M.A.; resources, M.F., J.R.K., and T.M.; data curation, M.F. and T.M.; writing—original draft preparation, M.F.; writing—review and editing, J.R.K., M.F., and M.M.A.; visualization, T.M. and M.F.; supervision, M.F.; project administration, M.F.; funding acquisition, M.F. All authors have read and agreed to the published version of the manuscript.

Funding: This work was supported by Japan Society for the Promotion of Science (JSPS)–KAKENHI Grants-in-Aid for Scientific Research [16655046 (FY2003–2005) and 22350052 (FY2010–2013)], the Sekisui Integrated Research Co. (SRI) (non-traditional design of helical polymers learning from the origin of homochirality, FY2009), the NAIST Foundation (FY2009), Japan Science and Technology Agency (JST): CREST program (design of hyperhelical polymers and understanding of structure-property-functionality relationship, FY1998–2003), and an in-house proposal at NTT Basic Research Laboratory (FY1994–1998).

Data Availability Statement: The data presented in this study are available on reasonable request from the corresponding author.

Acknowledgments: The authors are grateful to the respected scholars, researchers, and students listed in the acknowledgements of refs. [113,114], particularly Masaaki Ishikawa, Anubhav Saxena, Yoshihiro Kimura, Fumiko Ichiyanagi, Yasuko Nakamura, Yoko Nakano, Makoto Taguchi, Ayako Nakao, Nozomu Suzuki, Puhup Puneet, Nanami Ogata, and Seiko Amazumi in their days as students and researchers (FY 2002–2019) when they joined the MPV validation projects at NAIST. M.M.A. and M.F. thank Kotohiro Nomura (Tokyo Metropolitan University) for fruitful discussion and valuable comments. M.F. is thankful to Takashi Takakuwa, Yoshirou Kondo, Koushi Nagamori, and Nobuyuki Sakayanagi at JASCO for technical advice over three decades. Special thanks are given to Yasuo Nakanishi and Yoshio Morikage at JASCO Engineering Service (Osaka, Japan), who maintained the chiroptical spectrometers for many years. M.F. and J.R.K. express their gratitude to the late Hideki Sakurai (1931–2024, Tohoku University) and the late Robert West (1928–2022, University of Wisconsin–Madison) for stimulating comments and discussion around the helical polysilane projects over many years. M.F. is grateful to the late Meir Shinitzky (1939–2015, Weizmann Institute of Science) for sharing the MPV hypothesis.

Conflicts of Interest: The authors declare no conflicts of interest.

References

1. Hegstrom, R.A.; Kondepudi, D.K. The handedness of the universe. *Sci. Am.* **1990**, *262*, 108–115. [CrossRef]
2. Morozov, L.L.; Kuz'min, V.V.; Goldanskii, V.I. Comparative analysis of the role of statistical fluctuations and factor of advantage (parity nonconservation) in the origins of optical activity. *Orig. Life* **1983**, *13*, 119–138. [CrossRef]
3. Avetisov, V.A.; Goldanskii, V.I.; Kuz'min, V.V. Handedness, Origin of life and evolution. *Phys. Today* **1991**, *44*, 33–41. [CrossRef] [PubMed]
4. Mason, S.F. Chapter 11: Chiral energy discrimination. In *Molecular Optical Activity and the Chiral Discriminations*; Cambridge University Press: Cambridge, UK, 1982; ISBN 978-0521105637.

5. Mason, S.F.; Tranter, G.E. The parity-violating energy difference between enantiomeric molecules. *Mol. Phys.* **1984**, *53*, 1091–1111. [CrossRef]
6. Mason, S.F.; Tranter, G.E. The electroweak origin of biomolecular handedness. *Proc. R. Soc. A Math. Phys. Sci.* **1985**, *397*, 45–65. [CrossRef]
7. Mason, S.F. Biomolecular homochirality. *Chem. Soc. Rev.* **1988**, *17*, 347–359. [CrossRef]
8. Mason, S.F. *Chemical Evolution: Origin of the Elements, Molecules, and Living Systems*; Clarendon: Oxford, UK, 1991; ISBN 978-0198552727.
9. Latal, H. Chapter 1: Parity violation in atomic physics. In *Chirality: From Weak Bosons to the α–Helix*; Janoschek, R., Ed.; Springer: Berlin/Heidelberg, Germany, 1991; pp. 1–17. ISBN 978-3642765711. [CrossRef]
10. Janoschek, R. Chapter 2: Theories on the origin of biomolecular homochirality. In *Chirality: From Weak Bosons to the α–Helix*; Janoschek, R., Ed.; Springer: Berlin/Heidelberg, Germany, 1991; pp. 18–33. ISBN 978-3642765711. [CrossRef]
11. Gardner, M. *The New Ambidextrous Universe: Symmetry and Asymmetry from Mirror Reflections to Superstrings*, 3rd ed.; Dover: Mineola, NY, USA, 1995; ISBN 978-0716720935.
12. Compton, R.N.; Pagni, R.M. The chirality of biomolecules. *Adv. Atom. Mol. Opt. Phys.* **2002**, *48*, 219–261. [CrossRef]
13. Barron, L. *Molecular Light Scattering and Optical Activity*, 2nd ed.; Cambridge University Press: Cambridge, UK, 2004; ISBN 978-0521121378.
14. Wagnière, G.H. *On Chirality and the Universal Asymmetry: Reflections on Image and Mirror Image*; Wiley-VCH: Weinheim, GE, USA, 2007; ISBN 978-3906390383.
15. Guijarro, A.; Yus, M. *The Origin of Chirality in the Molecules of Life: A Revision from Awareness to the Current Theories and Perspectives of this Unsolved Problem*; RSC: Cambridge, UK, 2008; ISBN 978-0854041565.
16. Quack, M. On the measurement of the parity violating energy difference between enantiomers. *Chem. Phys. Lett.* **1986**, *132*, 147–153. [CrossRef]
17. Quack, M. How important is parity violation for molecular and biomolecular chirality? *Angew. Chem. Int. Ed.* **2002**, *41*, 4618–4630. [CrossRef]
18. Quack, M.; Stohner, J.; Willeke, M. High-resolution spectroscopic studies and theory of parity violation in chiral molecules. *Annu. Rev. Phys. Chem.* **2008**, *59*, 741–769. [CrossRef]
19. Quack, M.; Seyfang, M.G.; Wichmann, G. Perspectives on parity violation in chiral molecules: Theory, spectroscopic experiment and biomolecular homochirality. *Chem. Sci.* **2022**, *13*, 10598–10643. [CrossRef] [PubMed]
20. Sallembien, Q.; Bouteiller, L.; Crassous, J.; Raynal, M. Possible chemical and physical scenarios towards biological homochirality. *Chem. Soc. Rev.* **2022**, *51*, 3436–3476. [CrossRef]
21. Fujiki, M. Experimental tests of parity violation at helical polysilylene level. *Macromol. Rapid Commun.* **2001**, *22*, 669–674. [CrossRef]
22. Fujiki, M. Mirror symmetry breaking of silicon polymers—From weak bosons to artificial helix. *Chem. Rec.* **2009**, *9*, 271–298. [CrossRef]
23. Fujiki, M. Mirror symmetry breaking in helical polysilanes: Preference between left and right of chemical and physical origin. *Symmetry* **2010**, *2*, 1625–1652. [CrossRef]
24. Fujiki, M. Chapter 1: Chirogenesis in parity violation and weak forces. In *Chirogenesis in Chemical Science*; Borovkov, V., Aav, R., Eds.; World Scientific: Singapore, 2023; pp. 1–68. ISBN 978-9811259210. [CrossRef]
25. Seljuk, U. Measuring polarization in the cosmic microwave background. *Atrophys. J.* **1997**, *482*, 6–16. [CrossRef]
26. Kovac, J.M.; Leitch, E.M.; Pryke, C.; Carlstrom, J.E.; Halverson, N.W.; Holzapfel, W.L. Detection of polarization in the cosmic microwave background using DASI. *Nature* **2002**, *420*, 772–787. [CrossRef] [PubMed]
27. National Research Council; Division on Engineering, Physical Sciences; Board on Physics; Committee on the Physics of the Universe. *Connecting Quarks with the Cosmos: Eleven Science Questions for the New Century*; National Academic Press: Washington, DC, USA, 2003; ISBN 978-0309074063.
28. Minami, Y.; Komatsu, E. New extraction of the cosmic birefringence from the Planck 2018 polarization Data. *Phys. Rev. Lett.* **2020**, *125*, 221301. [CrossRef]
29. Komatsu, E. New physics from the polarised light of the cosmic microwave background. *Nat. Rev. Phys.* **2022**, *4*, 452–469. [CrossRef]
30. Hou, J.; Slepian, Z.; Cahn, R.N. Measurement of parity-odd modes in the large-scale 4-point correlation function of Sloan digital survey baryon oscillation spectroscopic survey twelfth data release CMASS and LOWZ galaxies. *Mon. Not. R. Astron. Soc.* **2023**, *522*, 5701–5739. [CrossRef]
31. Standard Model. Available online: https://en.wikipedia.org/wiki/Standard_Model (accessed on 20 January 2025).
32. Particle Physics. Available online: https://en.wikipedia.org/wiki/Particle_physics (accessed on 8 January 2025).
33. Beta Decay. Available online: https://en.wikipedia.org/wiki/Beta_decay (accessed on 19 January 2025).

34. Sgouros, G.; Bodei, L.; McDevitt, M.R.; Nedrow, J.R. Radiopharmaceutical therapy in cancer: Clinical advances and challenges. *Nat. Rev. Drug Discov.* **2020**, *19*, 589–608. [CrossRef]
35. Hasert, F.J.; Kabe, S.; Krenz, W.; Von Krogh, J.; Lanske, D.; Morfin, J.; Schultze, K.; Weerts, H.; Bertrand-Coremans, G.; Sacton, J.; et al. Observation of neutrino-like interactions without muon or electron in the Gargamelle neutrino experiment. *Nucl. Phys. B* **1974**, *73*, 1–22. [CrossRef]
36. Haidt, D. Chapter 7: The discovery of weak neutral currents. In *60 Years of CERN Experiments and Discovery*; Schopper, H., Di Lella, L., Eds.; World Scientific: Singapore, 2015; pp. 165–183. ISBN 978-9814644143. [CrossRef]
37. Bagnaia, P.; Banner, M.; Battiston, R.; Bloch, P.; Bonaudi, F.; Borer, K.; Borghini, M.; Chollet, J.-C.; Clark, A.G.; Conta, C.; et al. (The UA2 Collaboration). Evidence for $Z^0 \to e^+e^-$ at the CERN *pp* collider. *Phys. Lett. B* **1983**, *129*, 130–140. [CrossRef]
38. Arnison, G.T.; Astbury, A.; Aubert, B.; Bacci, C.; Bauer, G.; Bezaguet, A.; Böck, R.; Bowcock, T.J.V.; Calvetti, M.; Catz, P.; et al. (The UA2 Collaboration). Experimental observation of lepton pairs of invariant mass around 95 GeV/c^2 at the CERN SPS collider. *Phys. Lett. B* **1983**, *126*, 398–410. [CrossRef]
39. Di Lella, L.; Rubbia, C. Chapter 6: The discovery of the W and Z particles. In *60 Years of CERN Experiments and Discovery*; Schopper, H., Di Lella, L., Eds.; World Scientific: Singapore, 2015; pp. 137–163. ISBN 978-9814644143. [CrossRef]
40. Zel'dovich, Y.B. Electromagnetic interaction with parity violation. *Sov. Phys. JETP* **1958**, *6*, 1184–1186. Available online: http://www.jetp.ras.ru/cgi-bin/dn/e_006_06_1184.pdf (accessed on 7 March 2025).
41. Zel'dovich, Y.B. Parity nonconservation in the first order in the weak-interaction constant in electron scattering and other effects. *Sov. Phys. JETP Lett.* **1959**, *9*, 682–683. Available online: www.jetp.ras.ru/cgi-bin/dn/e_009_03_0682.pdf (accessed on 7 March 2025).
42. Zel'dovich, Y.B.; Perelomov, A.M. The effect of weak interaction on the electromagnetic properties of particles. *Sov. Phys. JETP* **1961**, *12*, 777–784. Available online: https://www.osti.gov/biblio/4097351 (accessed on 7 March 2025).
43. Michel, F.C. Parity nonconservation in nuclei. *Phys. Rev.* **1964**, *133*, B329–B349. [CrossRef]
44. Stodolsky, L. Neutron optics and weak currents. *Phys. Lett. B* **1974**, *50*, 352–356. [CrossRef]
45. Stodolsky, L. Parity violation in threshold neutron scattering. *Nucl. Phys. B* **1982**, *197*, 213–227. [CrossRef]
46. Bouchiat, M.A.; Bouchiat, C. Weak neutral currents in atomic physics. *Phys. Lett. B* **1974**, *48*, 111–114. [CrossRef]
47. Bouchiat, M.A.; Bouchiat, C.I. Parity violation induced by weak neutral currents in atomic physics. *J. Phys.* **1974**, *35*, 899–927. [CrossRef]
48. Bouchiat, M.A.; Bouchiat, C. Parity violation induced by weak neutral currents in atomic physics. Part II. *J. Phys.* **1975**, *36*, 493–509. [CrossRef]
49. Bouchiat, M.-A.; Bouchiat, C. *Parity Violation in Atoms and Polarized Electron Scattering*; Atomic parity violation: An overview; Frois, B., Bouchiat, M.-A., Eds.; World Scientific: Singapore, 1999; pp. 191–243. ISBN 978-9810237318.
50. Hegstrom, R.A.; Chamberlain, J.P.; Seto, K.; Watson, R.G. Mapping the weak chirality of atoms. *Am. J. Phys.* **1988**, *56*, 1086–1091. [CrossRef]
51. Baird, P.E.G.; Brimicombe, M.W.S.M.; Roberts, G.J.; Sandars, P.G.H.; Soreide, D.C.; Fortson, E.N.; Lewis, L.L.; Lindahl, E.G.; Soreide, D.C. Search for parity non-conserving optical rotation in atomic bismuth. *Nature* **1976**, *264*, 528–529. [CrossRef]
52. Fortson, E.N.; Wilets, L. Parity nonconservation in atoms: Status of theory and experiment. *Adv. Atom. Mol. Phys.* **1980**, *16*, 319–373. [CrossRef]
53. Bouchiat, M.A.; Guena, J.; Hunter, L.; Pottier, L. Observation of a parity violation in cesium. *Phys. Lett. B* **1982**, *117*, 358–364. [CrossRef]
54. Fortson, E.N.; Lewis, L.L. Atomic parity nonconservation experiments. *Phys. Rep.* **1984**, *113*, 289–344. [CrossRef]
55. Bouchiat, M.-A.; Bouchiat, C. Parity violation in atoms. *Rep. Prog. Phys.* **1997**, *60*, 1351–1396. [CrossRef]
56. Forte, M.; Heckle, B.R.; Ramsey, N.F.; Green, K.; Ramsey, G.L.; Byrne, J.; Pendlebury, J.M. First measurement of parity-nonconserving neutron-spin rotation: The tin isotopes. *Phys. Rev. Lett.* **1980**, *45*, 2088–2091. [CrossRef]
57. Alfimenkov, V.P.; Borzakov, S.B.; Van Thuan, V.; Mareev, Y.D.; Pikelner, L.B.; Khrykin, A.S.; Sharapov, E.I. Parity nonconservation in neutron resonances. *Nucl. Phys. A* **1983**, *398*, 93–106. [CrossRef]
58. Yuan, V.W.; Bowman, C.D.; Bowman, J.D.; Bush, J.E.; Delheij, P.P.J.; Frankle, C.M.; Gould, C.R.; Haase, D.G.; Knundson, J.N.; Mitchell, G.E.; et al. Parity nonconservation in polarized-neutron transmission through ^{139}La. *Phys. Rev. C* **1991**, *44*, 2187–2194. [CrossRef] [PubMed]
59. Crawford, B.E.; Bowman, J.D.; Bowman, C.D.; Bush, J.E.; Delheij, P.P.J.; Frankle, C.M.; Gould, C.R.; Haase, D.G.; Knudson, J.; Mitchell, G.E.; et al. Parity nonconservation for neutron resonances in ^{238}U. *Phys. Rev. Lett.* **1990**, *65*, 1192–1195. [CrossRef]
60. Mitchell, G.E.; Bowman, J.D.; Weidenmüller, H.A. Parity violation in the compound nucleus. *Rev. Mod. Phys.* **1999**, *71*, 445–457. [CrossRef]
61. Smith, D.A.; Bowman, D.; Crawford, B.E.; Grossmann, C.A.; Haseyama, T.; Johnson, M.B.; Masaike, A.; Matsuda, Y.; Mitchell, G.E.; Nazarenko, V.A.; et al. Parity violation in neutron resonances of ^{117}Sn. *Phys. Rev. C* **2001**, *64*, 015502. [CrossRef]
62. Yamagata, Y. A hypothesis for the asymmetric appearance of biomolecules on Earth. *J. Theor. Biol.* **1966**, *11*, 495–498. [CrossRef]

63. Rein, D.W. Some remarks on parity violating effects of intramolecular interactions. *J. Mol. Evol.* **1974**, *4*, 15–22. [CrossRef]
64. Letokhov, V.S. On difference of energy levels of left and right molecules due to weak interactions. *Phys. Lett. A* **1975**, *53*, 275–276. [CrossRef]
65. Zel'dovich, Y.B.; Saakyan, D.B.; Sobel'Man, I.I. Energy difference between right–hand and left-hand molecules, due to parity nonconservation in weak interactions of electrons with nuclei. *Sov. Phys. JETP Lett.* **1977**, *25*, 94–97. Available online: http://jetpletters.ru/ps/1388/article_21066.pdf (accessed on 7 March 2025).
66. Keszthelyi, L. Origin of the asymmetry of biomolecules and weak interaction. *Orig. Life* **1977**, *8*, 299–340. [CrossRef]
67. Harris, R.A.; Stodolsky, L. Quantum beats in optical activity and weak interactions. *Phys. Lett. B* **1978**, *78*, 313–317. [CrossRef]
68. Rein, D.W.; Hegstrom, R.A.; Sandars, P.G.H. Parity non-conserving energy difference between mirror image molecules. *Phys. Lett. A* **1979**, *71*, 499–502. [CrossRef]
69. Thiemann, W.; Darge, W. Experimental attempts for the study of the origin of optical activity on earth. *Orig. Life* **1974**, *5*, 263–283. [CrossRef] [PubMed]
70. Hegstrom, R.A.; Rein, D.W.; Sandars, P.G.H. Calculation of the parity nonconverging energy difference between mirror-image molecules. *J. Chem. Phys.* **1980**, *73*, 2329–2341. [CrossRef]
71. Mason, S.F.; Tranter, G.E. Energy inequivalence of peptide enantiomers from parity non-conservation. *J. Chem. Soc. Chem. Commun.* **1983**, 117–119. [CrossRef]
72. Tranter, G.E. Preferential stabilization of the D-sugar series by the parity-violating weak interactions. *J. Chem. Soc. Chem. Commun.* **1986**, 60–61. [CrossRef]
73. Wiesenfeld, L. Effect of atomic number on parity-violating energy differences between enantiomers. *Mol. Phys.* **1988**, *64*, 739–745. [CrossRef]
74. Laerdahl, J.K.; Wesendrup, R.; Schwerdtfeger, P. D- or L-alanine: That is the question. *ChemPhysChem* **2000**, 60–62. [CrossRef]
75. Schwerdtfeger, P.; Gierlich, J.; Bollwein, T. Large parity-violation effects in heavy-metal-containing chiral compounds. *Angew. Chem. Int. Ed.* **2003**, *42*, 1293–1296. [CrossRef]
76. Crassous, J.; Chardonnet, C.; Saue, T.; Schwerdtfeger, P. Recent experimental and theoretical developments towards the observation of parity violation (PV) effects in molecules by spectroscopy. *Org. Biomol. Chem.* **2005**, *3*, 2218–2224. [CrossRef]
77. Fiechter, M.R.; Haase, P.A.B.; Saleh, N.; Soulard, P.; Tremblay, B.; Havenith, R.W.A.; Timmermans, R.G.E.; Schwerdtfeger, P.; Crassous, J.; Darquié, B.; et al. Toward detection of the molecular parity violation in chiral $Ru(acac)_3$ and $Os(acac)_3$. *J. Phys. Chem. Lett.* **2022**, *13*, 10011–10017. [CrossRef]
78. Pagni, R.M.; Compton, R.N. Asymmetric synthesis of optically active sodium chlorate and bromate crystals. *Cryst. Grow. Des.* **2002**, *2*, 249–253. [CrossRef]
79. Macdermott, A.J.; Tranter, G.E. The search for large parity-violating energy differences between enantiomers. *Chem. Phys. Lett.* **1989**, *163*, 1–4. [CrossRef]
80. MacDermott, A.J.; Hegstrom, R.A. A proposed experiment to measure the parity-violating energy difference between enantiomers from the optical rotation of chiral ammonia-like "cat" molecules. *Chem. Phys.* **2004**, *305*, 55–68. [CrossRef]
81. Macdermott, A.J. Chiroptical signatures of life and fundamental physics. *Chirality* **2012**, *24*, 764–769. [CrossRef]
82. Zanasi, R.; Lazzeretti, P. On the stabilization of natural L-enantiomers of α-amino acids via parity-violating effects. *Chem. Phys. Lett.* **1998**, *286*, 240–242. [CrossRef]
83. Zanasi, R.; Lazzeretti, P.; Ligabue, A.; Soncini, A. Theoretical results which strengthen the hypothesis of electroweak bioenantioselection. *Phys. Rev. E* **1999**, *59*, 3382–3385. [CrossRef]
84. Bargueño, P.; Gonzalo, I.; de Tudela, R.P. Detection of parity violation in chiral molecules by external tuning of electroweak optical activity. *Phys. Rev. A* **2009**, *80*, 012110. [CrossRef]
85. Gonzalo, I.; Bargueño, P.; de Tudela, R.P.; Miret-Artés, S. Towards the detection of parity symmetry breaking in chiral molecules. *Chem. Phys. Lett.* **2010**, *489*, 127–129. [CrossRef]
86. Bargueño, P.; de Tudela, R.P.; Miret-Artés, S.; Gonzalo, I. An alternative route to detect parity violating energy differences through Bose–Einstein condensation of chiral molecules. *Phys. Chem. Chem. Phys.* **2011**, *13*, 806–810. [CrossRef]
87. Dorta-Urra, A.; Peñate-Rodríguez, H.C.; Bargueño, P.; Rojas-Lorenzo, G.; Miret-Artés, S. Dissipative geometric phase and decoherence in parity-violating chiral molecules. *J. Chem. Phys.* **2012**, *136*, 174505. [CrossRef] [PubMed]
88. Martínez-Gil, D.; Bargueño, P.; Miret-Artés, S. The interplay between tunneling and parity violation in chiral molecules. *Entropy* **2024**, *26*, 456. [CrossRef] [PubMed]
89. Eills, J.; Blanchard, J.W.; Bougas, L.; Kozlov, M.G.; Pines, A.; Budker, D. Measuring molecular parity nonconservation using nuclear-magnetic-resonance spectroscopy. *Phys. Rev. A* **2017**, *96*, 042119. [CrossRef]
90. Blanchard, J.W.; King, J.P.; Sjolander, T.F.; Kozlov, M.G.; Budker, D. Molecular parity nonconservation in nuclear spin couplings. *Phys. Rev. Res.* **2020**, *2*, 023258. [CrossRef]
91. Wilen, S.H.; Eliel, E.L.; Mander, L.N. *Stereochemistry of Organic Compounds*; Wiley-Interscience: New York, NY, USA, 1994; ISBN 978-0471016700.

92. Mislow, K. *Introduction to Stereochemistry*; Dover: Mineola, NY, USA, 2003; ISBN 978-0486425306.
93. Berova, N.; Polavarapu, P.; Nakanishi, K.; Woody, R.W. *Comprehensive Chiroptical Spectroscopy, Volume 1: Instrumentation, Methodologies, and Theoretical Simulations*; Wiley: Hoboken, NJ, USA, 2012; ISBN 978-1118012932.
94. Berova, N.; Polavarapu, P.; Nakanishi, K.; Woody, R.W. *Comprehensive Chiroptical Spectroscopy, Volume 2: Applications in Stereochemical Analysis of Synthetic Compounds, Natural Products, and Biomolecules*; Wiley: Hoboken, NJ, USA, 2012; ISBN 978-1118012925.
95. Szabó-Nagy, A.; Keszthelyi, L. Demonstration of the parity-violating energy difference between enantiomers. *Proc. Natl. Acad. Sci. USA* **1999**, *96*, 4252–4255. [CrossRef]
96. Wang, W.; Yi, F.; Ni, Y.; Zhao, Z.; Jin, X.; Tang, Y. Parity violation of electroweak force in phase transitions of single crystals of D-and L-alanine and valine. *J. Biol. Phys.* **2000**, *26*, 51–65. [CrossRef]
97. Wang, W.-Q.; Min, W.; Liang, Z.; Wang, L.-Y.; Chen, L.; Deng, F. NMR and parity violation: Low-temperature dependence in ^{1}H CRAMPS and ^{13}C CP/MAS ssNMR spectra of alanine enantiomer. *Biophys. Chem.* **2003**, *103*, 289–298. [CrossRef]
98. Shinitzky, M.; Haimovitz, R. Chiral surfaces in micelles of enantiomeric *N*-palmitoyl- and *N*-stearoylserine. *J. Am. Chem. Soc.* **1993**, *115*, 12545–12549. [CrossRef]
99. Shinitzky, M.; Nudelman, F.; Barda, Y.; Haimovitz, R.; Chen, E.; Deamer, D.W. Unexpected differences between D-and L-tyrosine lead to chiral enhancement in racemic mixtures. *Orig. Life Evol. Biosph.* **2002**, *32*, 285–297. [CrossRef]
100. Scolnik, Y.; Portnaya, I.; Cogan, U.; Tal, S.; Haimovitz, R.; Fridkin, M.; Elitzur, A.C.; Deamer, D.W.; Shinitzky, M. Subtle differences in structural transitions between poly-L- and poly-D-amino acids of equal length in water. *Phys. Chem. Chem. Phys.* **2006**, *8*, 333–339. [CrossRef]
101. Shinitzky, M.; Elitzure, A.C. *Ortho–para* spin isomers of the protons in the methylene group—Possible implications for protein structure. *Chirality* **2006**, *18*, 754–756. [CrossRef] [PubMed]
102. Deamer, D.W.; Dick, R.; Thiemann, W.; Shinitzky, M. Intrinsic asymmetries of amino acid enantiomers and their peptides: A possible role in the origin of biochirality. *Chirality* **2007**, *19*, 751–763. [CrossRef] [PubMed]
103. Shinitzky, M. Space asymmetry as a possible global feature. *Chirality* **2013**, *25*, 308–311. [CrossRef] [PubMed]
104. Shinitzky, M. Information storage in liquids with ordered molecular assemblies. *Entropy* **2011**, *13*, 1–10. [CrossRef]
105. Kodona, E.K.; Alexopoulos, C.; Panou-Pomonis, E.; Pomonis, P.J. Chirality and helix stability of polyglutamic acid enantiomers. *J. Colloid Interface. Sci.* **2008**, *319*, 72–80. [CrossRef]
106. Fujiki, M.; Okazaki, S.; Rahim, N.A.A.; Yamada, T.; Nomura, K. Synchronization in non-mirror-symmetrical chirogenesis: Non-helical π–conjugated polymers with helical polysilane copolymers in co-colloids. *Symmetry* **2021**, *13*, 594. [CrossRef]
107. Salam, A. The role of chirality in the origin of life. *J. Mol. Evol.* **1991**, *33*, 105–113. [CrossRef]
108. Salam, A. Chirality, phase transitions and their induction in amino acids. *Phys. Lett. B* **1992**, *288*, 153–160. [CrossRef]
109. Gabuda, S.P.; Kozlova, S.G. Abnormal difference between the mobilities of left- and right-twisted conformations of $C_6H_{12}N_2$ roto-symmetrical molecules at very low temperatures. *J. Chem. Phys.* **2015**, *142*, 234302. [CrossRef]
110. Kozlova, S.G.; Mirzaeva, I.V.; Ryzhikov, M.R. DABCO molecule in the $M_2(C_8H_4O_4)_2{\cdot}C_6H_{12}N_2$ (M = Co, Ni, Cu, Zn) metal-organic frameworks. *Coord. Chem. Rev.* **2018**, *376*, 62–74. [CrossRef]
111. Kozlova, S.G.; Gabuda, S.P. Thermal properties of $Zn_2(C_8H_4O_4)_2{\cdot}C_6H_{12}N_2$ metalorganic framework compound and mirror symmetry violation of dabco molecules. *Sci. Rep.* **2017**, *7*, 11505. [CrossRef] [PubMed]
112. Kozlova, S.; Ryzhikov, M.; Pishchur, D.; Mirzaeva, I. Overview of low-temperature heat capacity data for $Zn_2(C_8H_4O_4)_2{\cdot}C_6H_{12}N_2$ and the Salam hypothesis. *Symmetry* **2019**, *11*, 657. [CrossRef]
113. Fujiki, M.; Koe, J.R.; Mori, T.; Kimura, Y. Questions of mirror symmetry at the photoexcited and ground states of non-rigid luminophores raised by circularly polarized luminescence and circular dichroism spectroscopy: Part 1. Oligofluorenes, oligophenylenes, binaphthyls and fused aromatics. *Molecules* **2018**, *23*, 2606. [CrossRef]
114. Fujiki, M.; Koe, J.R.; Amazumi, S. Questions of mirror symmetry at the photoexcited and ground states of non-rigid luminophores raised by circularly polarized luminescence and circular dichroism spectroscopy. Part 2: Perylenes, BODIPYs, molecular scintillators, coumarins, rhodamine B, and DCM. *Symmetry* **2019**, *11*, 363. [CrossRef]
115. Puneet, P.; Singh, S.; Fujiki, M.; Nandan, B. Handed mirror symmetry breaking at the photo-excited state of π-conjugated rotamers in solutions. *Symmetry* **2021**, *13*, 272. [CrossRef]
116. McGlynn, S.P.; Azumi, T.; Kinoshita, M. *Molecular Spectroscopy of The Triplet State*; Prentice-Hall: Englewood Coffs, NJ, USA, 1969; ISBN 978-0135996621.
117. Turro, N.J. *Modern Molecular Photochemistry*; University Science Books: Sausalito, CA, USA, 1991; ISBN 978-0935702712.
118. Matin, W.C. Table of spin-orbit energies for *p*-electrons in neutral atomic (core) *np* configurations. *J. Res. Natl. Bur. Stand. A Phys. Chem.* **1971**, *75*, 109–111. [CrossRef]
119. Stone, N.J. Table of nuclear magnetic dipole and electric quadruple moments. *At. Data Nucl. Data Tables* **2014**, *90*, 75–176. [CrossRef]
120. Flambaum, V.V.; Khriplovich, I.B. P-odd nuclear force—A source of parity violation in atoms. *Sov. Phys. JETP* **1980**, *52*, 835–839. Available online: http://jetp.ras.ru/cgi-bin/dn/e_052_05_0835.pdf (accessed on 7 March 2025).

121. Sushkov, O.P.; Flambaum, V.V.; Khriplovich, I.B. Possibility of investigating P- and T-odd nuclear forces in atomic and molecular experiments. *Sov. Phys. JETP* **1984**, *60*, 873–883. Available online: http://www.jetp.ras.ru/cgi-bin/dn/e_060_05_0873.pdf (accessed on 7 March 2025).
122. Khriplovich, I.B. P-odd difference of hyperfine structure constants in optical isomers. *Z. Phys. A* **1985**, *322*, 507–509. [CrossRef]
123. Khriplovich, I.B.; Pospelov, M.E. Anapole moment of a chiral molecule. *Z. Phys.* **1990**, *47*, 81–84. [CrossRef]
124. Roberts, B.M.; Dzuba, V.A.; Flambaum, V.V. Parity and time-reversal violation in atomic systems. *Annu. Rev. Nucl. Part. Sci.* **2015**, *65*, 63–86. [CrossRef]
125. Wood, C.S.; Bennett, S.C.; Cho, D.; Masterson, B.P.; Roberts, J.L.; Tanner, C.E.; Wieman, C.E. Measurement of parity nonconservation and an anapole moment in cesium. *Science* **1997**, *275*, 1759–1763. [CrossRef]
126. Haxton, W.C.; Wieman, C.E. Atomic parity violation and nuclear anapole moments. *Annu. Rev. Nucl. Part. Sci.* **2001**, *51*, 261–293. [CrossRef]
127. Barra, A.L.; Robert, J.B.; Wiesenfeld, L. Possible observation of parity nonconservation by high-resolution NMR. *Europhys. Lett.* **1988**, *5*, 217–222. [CrossRef]
128. Kozlov, M.G.; Labzowsky, L.N. Parity Violation effects in diatomics. *J. Phys. B At. Mol. Opt. Phys.* **1995**, *28*, 1933–1961. [CrossRef]
129. DeMille, D.; Cahn, S.B.; Murphree, D.; Rahmlow, D.A.; Kozlov, M.G. Using molecules to measure nuclear spin-dependent parity violation. *Phys. Rev. Lett.* **2008**, *100*, 023003. [CrossRef]
130. Altuntaş, E.; Ammon, J.; Cahn, S.B.; DeMille, D. Demonstration of a sensitive method to measure nuclear-spin-dependent parity violation. *Phys. Rev. A* **2018**, *120*, 142501. [CrossRef] [PubMed]
131. Hao, Y.; Navrátil, P.; Norrgard, E.B.; Iliaš, M.; Eliav, E.; Timmermans, R.G.E.; Flambaum, V.V.; Borschevsky, A. Nuclear spin-dependent parity-violating effects in light polyatomic molecules. *Phys. Rev. A* **2020**, *102*, 052828. [CrossRef]
132. Laerdahl, J.K.; Schwerdtfeger, P. Fully relativistic ab initio calculations of the energies of chiral molecules including parity-violating weak interactions. *Phys. Rev. A* **1999**, *60*, 4439–4453. [CrossRef]
133. Aucar, I.A.; Borschevsky, A. Relativistic study of parity-violating nuclear spin-rotation tensors. *J. Chem. Phys.* **2021**, *155*, 134307. [CrossRef] [PubMed]
134. Aucar, A.; Jofré, M.T.C.; Aucar, G.A. Relativistic relationship between nuclear-spin-dependent parity-violating NMR shielding and nuclear spin-rotation tensors. *J. Chem. Phys.* **2023**, *152*, 094306. [CrossRef] [PubMed]
135. Fabian, H.; Berger, R.; Stohner, J. Investigation of parity violation in nuclear spin-rotation interaction of fluorooxirane. *Mol. Phys.* **2013**, *111*, 2345–2362. [CrossRef]
136. Rauhut, G.; Schwerdtfeger, P. Parity-violation effects in the vibrational spectra of CHFClBr and CDFClBr. *Phys. Rev. A* **2021**, *103*, 042819. [CrossRef]
137. Aucar, I.A.; Chamorro, Y.; Borschevsky, A. Parity-violating contributions to nuclear spin-rotation interactions and to NMR shielding constants in tetrahedral molecules. *Phys. Rev. A* **2022**, *106*, 062802. [CrossRef]
138. Fukuyama, T.; Momose, T.; Nomura, D. Anapole moment of a chiral molecule revisited. *Eur. Phys. J. D* **2015**, *69*, 264. [CrossRef]
139. Zarycz, N.; Provasi, P.F.; Pagola, G.I.; Ferraro, M.B.; Pelloni, S.; Lazzeretti, P. Computational study of basis set and electron correlation effects on anapole magnetizabilities of chiral molecules. *J. Comput. Chem.* **2016**, *37*, 1552–1558. [CrossRef]
140. Norrgard, E.B.; Barker, D.S.; Eckel, S.; Fedchak, J.A.; Klimov, N.N.; Scherschligt, J. Nuclear-spin dependent parity violation in optically trapped polyatomic molecules. *Commun. Phys.* **2019**, *2*, 77. [CrossRef]
141. Kaelberer, T.; Fedotov, V.A.; Papasimakis, N.; Tsai, D.P.; Zheludev, N.I. Toroidal dipolar response in a metamaterial. *Science* **2010**, *330*, 1510–1512. [CrossRef]
142. Ungur, L.; Lin, S.-Y.; Tang, J.; Chibotaru, L.F. Single-molecule toroics in Ising-type lanthanide molecular clusters. *Chem. Soc. Rev.* **2014**, *43*, 6894–6905. [CrossRef]
143. Miroshnichenko, A.E.; Evlyukhin, A.B.; Yu, Y.F.; Bakker, R.M.; Chipouline, A.; Kuznetsov, A.I.; Luk'yanchuk, B.; Chichkov, B.N.; Kivshar, Y.S. Nonradiating anapole modes in dielectric nanoparticles. *Nat. Commun.* **2015**, *6*, 8069. [CrossRef] [PubMed]
144. Savukov, I.M.; Lee, S.-K.; Romalis, M.V. Optical detection of liquid-state NMR. *Nature* **2006**, *442*, 1021–1024. [CrossRef]
145. Shi, J.; Ikäläinen, S.; Vaara, J.; Romalis, M.V. Observation of optical chemical shift by precision nuclear spin optical rotation measurements and calculations. *J. Phys. Chem. Lett.* **2013**, *4*, 437–441. [CrossRef]
146. Vaara, J.; Rizzo, A.; Kauczor, J.; Norman, P.; Coriani, S. Nuclear spin circular dichroism. *J. Chem. Phys.* **2014**, *140*, 134103. [CrossRef] [PubMed]
147. Kipping, F.S.; Pope, W.J. LXXXVIIL—Racemism and pseudoracemism. *J. Chem. Soc. Trans.* **1897**, *71*, 989–1001. [CrossRef]
148. Kipping, F.S.; Pope, W.J. LXIIL—Enantiomorphism. *J. Chem. Soc. Trans.* **1898**, *73*, 606–617. [CrossRef]
149. Mishima, K.; Kaji, D.; Fujiki, M.; Imai, Y. Remarkable effects of external magnetic field on circularly polarized luminescence of $Eu^{III}(hfa)_3$ with phosphine chirality. *ChemPhysChem* **2021**, *22*, 1728–1737. [CrossRef]
150. Dzuba, V.A.; Flambaum, V.V.; Khriplovich, I.B. Enhancement of P- and T-nonconserving effects in rare-earth atoms. *Z. Phys. D* **1986**, *1*, 243–245. [CrossRef]

151. Labzowsky, L.N.; Nefiodov, A.V.; Plunien, G.; Soff, G.; Marrus, R.; Liesen, D. Parity-violation effect in heliumlike gadolinium and europium. *Phys. Rev. A* **2001**, *63*, 054105. [CrossRef]
152. Sasanuma, Y.; Kato, H.; Kaito, A. Conformational analysis of poly(di-*n*-butylsilane), poly(di-*n*-hexylsilane), and poly(methyl-*n*-propylsilane) by a rotational isomeric state scheme with molecular dynamics simulations. *J. Phys. Chem. B* **2003**, *107*, 11852–11860. [CrossRef]
153. Kato, H.; Sasanuma, Y.; Kaito, A.; Tanigaki, N.; Tanabe, Y.; Kinugasa, S. Unperturbed chain dimensions of poly(di-*n*-hexylsilane), poly(methyl-*n*-propylsilane), and poly(di-*n*-butylsilane). *Macromolecules* **2001**, *34*, 262–268. [CrossRef]
154. Schilling, F.C.; Lovinger, A.J.; Zeigler, J.M.; Davis, D.D.; Bovey, F.A. Solid-state structures and thermochromism of poly(di-*n*-butylsilylene) and poly(di-*n*-pentylsilylene). *Macromolecules* **1989**, *22*, 3055–3063. [CrossRef]
155. Schweizer, K.S.; Harrah, L.A.; Zeigler, J.M. Chapter 22: Order-disorder transitions and thermochromism of polysilylenes in solution. In *Silicon-Based Polymer Science: A Comprehensive Resource*; Zeigler, J.M., Fearon, F.G., Eds.; ACS: Washington, DC, USA, 1989; pp. 379–395. ISBN 978-0841215467.
156. Miller, R.D.; Michl, J. Polysilane high polymers. *Chem. Rev.* **1989**, *89*, 1359–1410. [CrossRef]
157. Teramae, H.; Takeda, K. Ab initio studies on silicon compounds. 2. On the gauche structure of the parent polysilane. *J. Am. Chem. Soc.* **1989**, *111*, 1281–1285. [CrossRef]
158. Tachibana, H.; Matsumoto, M.; Tokura, Y.; Moritomo, Y.; Yamaguchi, A.; Koshihara, S.; Miller, R.D.; Abe, S. Spectra of one-dimensional excitons in polysilanes with various backbone conformations. *Phys. Rev. B* **1993**, *47*, 4363–4371. [CrossRef]
159. Fujiki, M. Effect of main chain length in the exciton spectra of helical-rod polysilanes as a model of a 5 Å wide quantum wire. *Appl. Phys. Lett.* **1994**, *65*, 3251–3253. [CrossRef]
160. Fujiki, M. Optically active polysilylenes: State-of-the-art chiroptical polymers. *Macromol. Rapid Commun.* **2001**, *22*, 539–563. [CrossRef]
161. Seki, S.; Terashima, Y.; Kunimi, Y.; Kawamori, T.; Tashiro, M.; Honda, Y.; Tagawa, S. The effects of free volumes on charge carrier transport in polysilanes probed by positron annihilation. *Rad. Phys. Chem.* **2003**, *68*, 501–505. [CrossRef]
162. Seki, S.; Koizumi, Y.; Kawaguchi, T.; Habara, H.; Tagawa, S. Dynamics of positive charge carriers on Si chains of polysilanes. *J. Am. Chem. Soc.* **2004**, *126*, 3521–3528. [CrossRef]
163. Kitao, T.; Bracco, S.; Comotti, A.; Sozzani, P.; Naito, M.; Seki, S.; Uemura, T.; Kitagawa, S. Confinement of single polysilane chains in coordination nanospaces. *J. Am. Chem. Soc.* **2015**, *137*, 5231–5238. [CrossRef]
164. Neumann, F.; Teramae, H.; Downing, J.W.; Michl, J. Gauche, ortho, and anti conformations of saturated A_4X_{10} chains: When will all six conformers exist? *J. Am. Chem. Soc.* **1998**, *120*, 573–582. [CrossRef]
165. Michl, J.; West, R. Conformations of linear chains. Systematics and suggestions for nomenclature. *Acc. Chem. Res.* **2000**, *33*, 821–823. [CrossRef] [PubMed]
166. Fogarty, H.A.; Ottosson, C.-H.; Michl, J. The five favored backbone conformations of *n*-Si_4Et_{10}: Cisoid, gauche, ortho, deviant, and transoid. *J. Mol. Struct. Theochem.* **2000**, *506*, 243–255. [CrossRef]
167. Fujiki, M. Helix magic. Thermo-driven chiroptical switching and screw-sense inversion of flexible rod helical polysilylenes. *J. Am. Chem. Soc.* **2000**, *122*, 3336–3343. [CrossRef]
168. Fujiki, M.; Koe, J.R.; Motonaga, M.; Nakashima, H.; Terao, K.; Teramoto, A. Computing handedness: Quantized and superposed switch and dynamic memory of helical polysilylene. *J. Am. Chem. Soc.* **2001**, *123*, 6253–6261. [CrossRef] [PubMed]
169. Ohno, O.; Kaizu, Y.; Kobayashi, H. J-aggregate formation of a water-soluble porphyrin in acidic aqueous media. *J. Chem. Phys.* **1993**, *99*, 4128–4139. [CrossRef]
170. Ribó, J.M.; Crusats, J.; Sagués, F.; Claret, J.; Rubires, R. Chiral sign induction by vortices during the formation of mesophases in stirred solutions. *Science* **2001**, *292*, 2063–2066. [CrossRef]
171. Crusats, J.; El-Hachemi, E.; Ribó, J.M. Hydrodynamic effects on chiral induction. *Chem. Soc. Rev.* **2010**, *39*, 569–577. [CrossRef]
172. Okano, K.; Taguchi, M.; Fujiki, M.; Yamashita, T. Circularly polarized luminescence of rhodamine B in a supramolecular chiral medium formed by a vortex flow. *Angew. Chem. Int. Ed.* **2011**, *50*, 12474–12477. [CrossRef]
173. Tang, X.; Ji, X.; Li, Y.; Li, B.; Yang, Y. Achiral polydialkylsilane aggregates that record stirring direction. *Chem. Asian J.* **2016**, *11*, 852–857. [CrossRef]
174. Sun, J.; Li, Y.; Yan, F.; Liu, C.; Sang, Y.; Tian, F.; Feng, Q.; Duan, P.; Zhang, L.; Shi, X.; et al. Control over the emerging chirality in supramolecular gels and solutions by chiral microvortices in milliseconds. *Nat. Commun.* **2018**, *9*, 2599. [CrossRef] [PubMed]
175. Kuroha, M.; Nambu, S.; Hattori, S.; Kitagawa, Y.; Niimura, K.; Mizuno, Y.; Hamba, F.; Ishii, K. Chiral Supramolecular nanoarchitectures from macroscopic mechanical rotations: Effects on enantioselective aggregation behavior of phthalocyanines. *Angew. Chem. Int. Ed.* **2019**, *58*, 18454–18459. [CrossRef] [PubMed]
176. Landau, R.; Würflinger, A. PVT-daten von acetonitril, undecan und dodecan bis 3 kbar und –50 °C. druckabhangigkeit der umwandlungsvolumina, -enthalpien und -entropien. *Ber. Bunsenges. Phys. Chem.* **1980**, *84*, 895–902. [CrossRef]
177. Laib, P.; Mittleman, D.M. Temperature-dependent terahertz spectroscopy of liquid *n*-alkanes. *J. Infrared Millim. Terahertz Waves* **2010**, *31*, 1015–1021. [CrossRef]

178. Naidu, S.V.; Smith, F.A. Defects in the rotator and liquid phases of *n*-alkanes: A study using FTIR and positron annihilation. *J. Phys. Cond. Matter* **1994**, *6*, 3865–3878. [CrossRef]
179. Anderson, P.W. More is different—Broken symmetry and the nature of the hierarchical structure of science. *Science* **1972**, *177*, 393. [CrossRef] [PubMed]
180. Cooper, L.N. Bound electron pairs in a degenerate fermi gas. *Phys. Rev.* **1956**, *104*, 1189–1190. [CrossRef]
181. Bardeen, J.; Cooper, L.N.; Schrieffer, J.R. Theory of superconductivity. *Phys. Rev.* **1957**, *108*, 1175–1204. [CrossRef]
182. Maxwell, E. Isotope effect in the superconductivity of mercury. *Phys. Rev.* **1950**, *78*, 477. [CrossRef]
183. Reynolds, C.A.; Serin, B.; Wright, W.H.; Nesbitt, L.B. Superconductivity of isotopes of mercury. *Phys. Rev.* **1950**, *78*, 487. [CrossRef]
184. Garland, J.W., Jr. Isotope effect in superconductivity. *Phys. Rev. Lett.* **1963**, *11*, 114–119. [CrossRef]
185. Power, P.P. Silicon, germanium, tin and lead analogues of acetylenes. *Chem. Commun.* **2003**, 2091–2101. [CrossRef] [PubMed]
186. Frisch, M.J.; Trucks, G.W.; Schlegel, H.B.; Scuseria, G.E.; Robb, M.A.; Cheeseman, J.R.; Scalmani, G.; Barone, V.; Mennucci, B.; Petersson, G.A.; et al. *Gaussian09 (Rev.D.01)*; Gaussian, Inc.: Wallingford, CT, USA, 2013.
187. Narayanamurtic, V.; Pohl, R.O. Tunneling states of defects in solids. *Rev. Mod. Phys.* **1970**, *42*, 201–236. [CrossRef]
188. Merzbacher, E. The early history of quantum tunneling. *Phys. Today* **2002**, *55*, 44–49. [CrossRef]
189. Fujiki, M.; Jalilah, A.J.; Koe, J.R.; Nomura, K.; Suzuki, N.; Rahim, N.A.A.; Zhang, W. Chapter 17: Ultraweak intermolecular interactions in chirogenesis from noncharged CPL-/CD-silent molecules, oligomers, and polymers endowed with noncharged chiral terpenes, mono-/polysaccharides, and helical polysilanes. In *Chiral Luminescence: From Molecules to Materials and Devices*; Akagi, K., Ed.; Wiley-VCH: Weinheim, Germany, 2024; pp. 381–415. ISBN 978-3527351800. [CrossRef]
190. Leggett, A.J. Bose-Einstein condensation in the alkali gases: Some fundamental concepts. *Rev. Mod. Phys.* **2001**, *73*, 307–356. [CrossRef]
191. Kikuchi, O.; Kiyonaga, H. Parity-violating energy shift of helical *n*-alkanes. *J. Mol. Struct. Theochem.* **1994**, *312*, 271–274. [CrossRef]
192. Kiyonaga, H.; Morihashi, K.; Kikuchi, O. Calculation of contributions of one- and two-electron spin-orbit coupling terms to the parity-violating energy shifts for amino acids and helical alkanes. *J. Chem. Phys.* **1998**, *108*, 2041–2043. [CrossRef]
193. Scherer, J.R.; Snyder, R.G. Raman spectra of liquid *n*-alkanes. II. Longitudinal acoustic modes and the gauche-trans energy difference. *J. Chem. Phys.* **1980**, *72*, 5798–5808. [CrossRef]
194. Snyder, R.G. The structure of chain molecules in the liquid state: Low frequency Raman spectra of *n*-alkanes and perfluoro-*n*-alkanes. *J. Chem. Phys.* **1982**, *76*, 3921–3927. [CrossRef]
195. Snyder, R.G.; Kim, Y. Conformation and low-frequency isotropic Raman spectra of the liquid *n*-alkanes C_4–C_9. *J. Phys. Chem.* **1991**, *95*, 602–610. [CrossRef]
196. Snyder, R.G. Chain conformation from the direct calculation of the Raman spectra of the liquid *n*-alkanes C_{12}–C_{20}. *J. Chem. Soc. Faraday Trans.* **1992**, *88*, 1823–1833. [CrossRef]
197. Thomas, L.L.; Christakis, T.J.; Jorgensen, W.L. Conformation of alkanes in the gas phase and pure liquids. *J. Phys. Chem. B* **2006**, *110*, 21198–21204. [CrossRef] [PubMed]
198. Sěbek, J.; Pele, L.; Potma, E.O.; Gerber, R.B. Raman spectra of long chain hydrocarbons: Anharmonic calculations, experiment and implications for imaging of biomembranes. *Phys. Chem. Chem. Phys.* **2011**, *13*, 12724–12733. [CrossRef] [PubMed]
199. Vansteenkiste, P.; van Speybroeck, V.; Marin, G.B.; Waroquier, M. Ab initio calculation of entropy and heat capacity of gas-phase *n*-alkanes using internal rotations. *J. Phys. Chem. A* **2003**, *107*, 3139–3145. [CrossRef]
200. Smith, G.D.; Jaffe, R.L. Quantum chemistry study of conformational energies and rotational energy barriers in *n*-alkanes. *J. Phys. Chem.* **1996**, *100*, 18718–18724. [CrossRef]
201. Snyder, R.G. Vibrational study of the chain conformation of the liquid *n*-paraffins and molten polyethylene. *J. Chem. Phys.* **1967**, *47*, 1316–1360. [CrossRef]
202. Maroncelli, M.; Strauss, H.L.; Snyder, R.G. The distribution of conformational disorder in the high-temperature phases of the crystalline *n*-alkanes. *J. Chem. Phys.* **1980**, *82*, 2811–2827. [CrossRef]
203. Maroncelli, M.; Qi, S.P.; Strauss, H.L.; Snyder, R.G. Nonplanar conformers and the phase behavior of solid *n*-alkanes. *J. Am. Chem. Soc.* **1982**, *104*, 6237–6247. [CrossRef]
204. Brown, K.G.; Bicknell-Brown, E.; Ladjadj, M. Raman-active bands sensitive to motion and conformation at the chain termini and backbones of alkanes and lipids. *J. Phys. Chem.* **1987**, *91*, 3436–3442. [CrossRef]
205. Menger, F.M.; D'Angelo, L.L. Does the conformation of hydrocarbon chains depend on solvation? *J. Am. Chem. Soc.* **1988**, *110*, 8241–8242. [CrossRef]
206. Lüttschwager, N.O.B.; Suhm, M.A. Stretching and folding of 2-nanometer hydrocarbon rods. *Soft Matter* **2014**, *10*, 4885–4901. [CrossRef] [PubMed]
207. Stumper, U. Dielectric absorption of liquid normal alkanes in the microwave and far infrared regions. *Adv. Mol. Relax. Proc.* **1975**, *7*, 189–208. [CrossRef]
208. Hermiz, N.A.; Hasted, J.B.; Rosenberg, C. Microwave dielectric losses of *n*-alkanes. *J. Chem. Soc. Faraday Trans.* **1982**, *78*, 147–161. [CrossRef]

209. Vij, J.K. Microwave and far-infra-red dielectric absorption in *n*-alkanes. *II Nuovo Cimento D* **1983**, *2*, 751–762. [CrossRef]
210. Weinberg angle. Available online: https://en.wikipedia.org/wiki/Weinberg_angle (accessed on 9 March 2025).
211. Koehler, J.S.; Dennison, D.M. Hindered rotation in methyl alcohol. *Phys. Rev.* **1940**, *57*, 1006–1021. [CrossRef]
212. Hilt, R.; Hubbard, P.S. Nuclear magnetic relaxation of three spin systems undergoing hindered rotations. *Phys. Rev.* **1964**, *134*, A392–A398. [CrossRef]
213. Runnels, L.K. Nuclear spin-lattice relaxation in three-spin molecules. *Phys. Rev.* **1964**, *134*, A28–A36. [CrossRef]
214. Gabay, M.; Toulouse, G. Coexistence of spin-glass and ferromagnetic orderings. *Phys. Rev. Lett.* **1981**, *47*, 201–203. [CrossRef]
215. Khan, O. Competing spin interactions and degenerate frustration for discrete molecular species. *Chem. Phys. Lett.* **1997**, *265*, 109–114. [CrossRef]
216. Schnack, J. Effects of frustration on magnetic molecules: A survey from Olivier Kahn till today. *Dalton Trans.* **2010**, *39*, 4677–4686. [CrossRef]
217. Balents, L. Spin liquids in frustrated magnets. *Nature* **2010**, *464*, 199–208. [CrossRef] [PubMed]
218. Wu, Y.; Krzyaniak, M.D.; Stoddart, J.F.; Wasielewski, M.R. Spin frustration in the triradical trianion of a naphthalenediimide, molecular triangle. *J. Am. Chem. Soc.* **2017**, *139*, 2948–2951. [CrossRef] [PubMed]
219. Tang, S.; Wang, X. Spin frustration in organic radicals. *Angew. Chem. Int. Ed.* **2024**, *63*, e202310147. [CrossRef]
220. Prager, M.A. Heidemann. Rotational tunneling and neutron spectroscopy: A compilation. *Chem. Rev.* **1997**, *97*, 2933–2966. [CrossRef]
221. Horsewill, A.J. Rotational tunneling in organic molecules. *Spectrochim. Acta A* **1992**, *48*, 379–403. [CrossRef]
222. Horsewill, A.J. Quantum tunnelling aspects of methyl group rotation studied by NMR. *Prog. Nucl. Magn. Res. Spectrosc.* **1999**, *35*, 359–389. [CrossRef]
223. Zachariou, A.; Hawkins, A.P.; Collier, P.; Howe, R.F.; Lennon, D.; Parker, S.F. The methyl torsion in unsaturated compounds. *ACS Omega* **2020**, *5*, 2755–2765. [CrossRef]
224. Clough, S.; Heidemann, A.; Horsewill, A.J.; Lewis, J.D.; Paley, M.N.J. The correlation of methyl tunnelling and thermally activated reorientation. *J. Phys. C* **1981**, *14*, L525–L529. [CrossRef]
225. Clough, S.; McDonald, P.J. The correlation of methyl tunnelling and thermally activated reorientation: II. *J. Phys. C* **1982**, *15*, L1039–L1042. [CrossRef]
226. Clough, S.; Heidemann, A.; Horsewill, A.J.; Lewis, J.D.; Paley, M.N.J. The rate of thermally activated methyl group rotation in solids. *J. Phys. C* **1982**, *15*, 2495–2508. [CrossRef]
227. Clough, S. The tunnelling methyl group: A probe of the quantum classical transition. *Sci. Progr. Oxford* **1991**, *75*, 121–139. Available online: https://www.jstor.org/stable/43421264 (accessed on 7 March 2025).
228. Montjoie, A.-S.; Müller-Warmuth, W. CH_3 rotational tunnelling in alkali acetates and correlation between NMR spin-lattice relaxation and neutron scattering Data. *Z. Naturforsch. A* **1985**, *40*, 596–601. [CrossRef]
229. Plazanet, M.; Neumann, M.A.; Trommsdorff, H.P. Methyl group rotational tunneling in vibrational spectra of crystals at low temperatures. *Chem. Phys. Lett.* **2000**, *320*, 651–657. [CrossRef]
230. Perras, F.A.; Matsuki, Y.; Southern, S.A.; Dubroca, T.; Flesariu, D.F.; Van Tol, J.; Constantinides, C.P.; Koutentis, P.A. Mechanistic origins of methyl-driven Overhauser DNP. *J. Chem. Phys.* **2023**, *158*, 154201. [CrossRef]
231. Jescheke, G. Rotational coupling in methyl-tunneling electron spin echo envelope modulation. *Appl. Magn. Reson.* **2022**, *53*, 635–651. [CrossRef] [PubMed]
232. Abed, K.J.; Clough, S. Methyl tunneling rotation in the *n*-alkanes. *Chem. Phys. Lett.* **1987**, *142*, 209–212. [CrossRef]
233. Tomkinson, J.; Parker, S.F.; Bradeny, D.A.; Hudson, B.S. Inelastic neutron scattering spectra of the transverse acoustic modes of the normal alkanes. *Phys. Chem. Chem. Phys.* **2002**, *4*, 716–772. [CrossRef]
234. Neumann, M.A.; Johnson, M.R.; Radaelli, P.G. The low temperature phase transition in octane and its possible generalization to other *n*-alkanes. *Chem. Phys.* **2011**, *266*, 53–68. [CrossRef]
235. Soulard, L.; Fillaux, F.; Braathen, G.; Le Calve, N.; Pasquier, B. Rotational dynamics of the methyl group in the 4-methyl pyridine crystal. *Chem. Phys. Lett.* **1986**, *125*, 41–46. [CrossRef]
236. Diezemann, G.; Häusler, W. Symmetry-species conversion in CD_3 systems. *J. Phys. Cond. Matter* **1993**, *5*, 6121–6138. [CrossRef]
237. Orth, K.; Rohlfing, F.; Friedrich, J. Rotational tunneling dynamics of methyl groups in *n*-alkane host lattices: An optical investigation and external isotope effect. *Z. Phys. B* **1994**, *95*, 493–501. [CrossRef]
238. Takeda, S.; Kataoka, H.; Ikeda, S.; Yamaguchi, K. Rotational tunneling of methyl groups of $Sc(CH_3COO)_3$ and $Sc(CD_3COO)_3$. *Phys. B* **1996**, *226*, 174–177. [CrossRef]
239. Somoza, M.M.; Friedrich, J. The physics of rotational tunneling: Hole-burning spectroscopy of methyl groups. *Low Temp. Phys.* **2006**, *32*, 1020–1027. [CrossRef]
240. Williams, J.; Eisenberg, A. Methyl group tunneling and viscoelastic relaxation in poly(methyl methacrylate). *Macromolecules* **1978**, *11*, 700–707. [CrossRef]

241. Gabryi, B.; Higgins, J.S.; Ma, K.T.; Roots, J.E. Rotational motion of the ester methyl group in stereoregular poly(methyl methacrylate): A neutron scattering study. *Macromolecules* **1984**, *17*, 560–566. [CrossRef]
242. Colmenero, J.; Mukhopadhyay, R.; Alegría, A.; Frick, B. Quantum rotational tunneling of methyl groups in polymers. *Phys. Rev. Lett.* **1998**, *80*, 2350–2353. [CrossRef]
243. Colmenero, J.; Moreno, A.J.; Alegría, A. Neutron scattering investigations on methyl group dynamics in polymers. *Prog. Polym. Sci.* **2005**, *30*, 1147–1184. [CrossRef]
244. Adams, M.A.; Gabrys, B.J.; Zajac, W.M.; Peiffer, D.G. High-resolution incoherent inelastic neutron scattering spectra of polyisobutylene and polyisoprene. *Macromolecules* **2005**, *38*, 160–166. [CrossRef]
245. Tachibana, S.; Morisawa, Y.; Ikehata, A.; Sato, H.; Higashi, N.; Ozaki, Y. Far-Ultraviolet spectra of *n*-alkanes and branched alkanes in the liquid phase observed using an attenuated total reflection-far ultraviolet (ATR-FUV) spectrometer. *Appl. Spectrosc.* **2011**, *65*, 221–226. [CrossRef]
246. Morisawa, Y.; Tachibana, S.; Ehara, M.; Ozaki, Y. Elucidating electronic transitions from σ orbitals of liquid *n*- and branched alkanes by far-ultraviolet spectroscopy and quantum chemical calculations. *J. Phys. Chem. A* **2012**, *116*, 11957–11964. [CrossRef]
247. Ozaki, Y.; Morisawa, Y.; Tanabe, I.; Beć, K. ATR-far-ultraviolet spectroscopy in the condensed phase—The present status and future perspectives. *Spectrochim. Acta Part A Mol. Biomol. Spectrosc.* **2021**, *253*, 119549. [CrossRef] [PubMed]
248. Lin-Vien, D.; Colthup, N.B.; Fateley, W.G.; Grasselli, J.G. Chapter 2: Alkanes. In *The Handbook of Infrared and Raman Characteristic Frequencies of Organic Molecules*; Elsevier: Amsterdam, The Netherlands, 1991; ISBN 978-0124511606.
249. Socrates, G. Chapter 2: Alkane Group Residue: C–H Group. In *Infrared and Raman Characteristic Group Frequencies: Tables and Charts*, 3rd ed.; Wiley: Chichester, UK, 2001; ISBN 978-0470093078.
250. Gorai, K.K.; Shastri, A.; Singh, P.J.; Jha, S.N. Experimental and theoretical studies on the absorption spectra of *n*-dodecane in the IR and VUV regions. *J. Quant. Spectrosc. Radiat. Transf.* **2019**, *236*, 106582. [CrossRef]
251. Knapp, D.; Brunschwig, B.S.; Lewis, N.S. Transmission infrared spectra of CH_3, CD_3, and $C_{10}H_{21}$-Ge(111) surfaces. *J. Phys. Chem. C* **2011**, *115*, 16389–163970. [CrossRef]
252. Tyrode, E.; Hedberg, J. A comparative study of the CD and CH stretching spectral regions of typical surfactants systems using VSFS: Orientation analysis of the terminal CH_3 and CD_3 groups. *J. Phys. Chem. C* **2012**, *116*, 1080–1091. [CrossRef]
253. Urata, H.; Shinohara, K.; Ogura, E.; Ueda, Y.; Akagi, M. Mirror-image DNA. *J. Am. Chem. Soc.* **1993**, *113*, 8174–8175. [CrossRef]
254. Milton, R.C.D.L.; Miton, S.C.F.; Kent, S.B.H. Total chemical synthesis of a D-enzyme: The Enantiomers of HIV-1 protease show demonstration of reciprocal chiral substrate specificity. *Science* **1992**, *256*, 1445–1448. [CrossRef]
255. Zawadzke, L.E.; Berg, J.M. A racemic protein. *J. Am. Chem. Soc.* **1992**, *114*, 4002–4003. [CrossRef]
256. Weinstock, M.T.; Jacobsen, M.T.; Kay, M.S. Synthesis and folding of a mirror-image enzyme reveals ambidextrous chaperone activity. *Proc. Natl. Acad. Sci. USA* **2014**, *111*, 11679–11684. [CrossRef]
257. Wang, Z.; Xu, W.; Liu, L.; Zhu, T.F. A synthetic molecular system capable of mirror-image genetic replication and transcription. *Nat. Chem.* **2016**, *8*, 698–704. [CrossRef]
258. Fan, C.; Deng, Q.; Zhu, T.F. Bioorthogonal information storage in L-DNA with a high-fidelity mirror-image *Pfu* DNA polymerase. *Nat. Biotechnol.* **2021**, *39*, 1548–1555. [CrossRef]
259. Vallazza, M.; Perbandt, M.; Klussmann, S.; Rypniewski, W.; Einspahr, H.M.; Erdmann, V.A.; Betzel, C. First look at RNA in L-configuration. *Acta Cryst. D* **2004**, *60*, 1–7. [CrossRef] [PubMed]
260. Bolik, S.; Rübhausen, M.; Binder, S.; Schulz, B.; Perbandt, M.; Genov, N.; Erdmann, V.; Klussmann, S.; Betzel, C. First experimental evidence for the preferential stabilization of the natural D- over the nonnatural L-configuration in nucleic acids. *RNA* **2007**, *13*, 1877–1880. [CrossRef] [PubMed]
261. Kiliszek, A.; Błaszczyk, L.; Bejger, M.; Rypniewski, W. Broken symmetry between RNA enantiomers in a crystal lattice. *Nucleic Acids Res.* **2021**, *49*, 12535–12539. [CrossRef] [PubMed]
262. Kiliszek, A.; Rypniewski, W. The emergence of biological homochirality. *Acta Biochim. Pol.* **2023**, *70*, 481–485. [CrossRef]
263. Garay, A.S.; Keszthelyi, L.; Demeter, I.; Hraskó, P. Differences in the annihilation of positrons in optical isomers. *Chem. Phys. Lett.* **1973**, *23*, 549–552. [CrossRef]
264. Sullivan, R.; Pyda, M.; Pak, J.; Wunderlich, B.; Thompson, J.R.; Pagni, R.; Barnes, C.; Schwerdtfeger, P.; Compton, R. Search for electroweak interactions in amino acid crystals. II. The Salam hypothesis. *J. Phys. Chem. A* **2003**, *107*, 6674–6680. [CrossRef]
265. Belo, E.A.; Pereira, J.E.; Freire, P.T.; Argyriou, D.N.; Eckert, J.; Bordallo, H.N. Hydrogen bonds in crystalline D-alanine: Diffraction and spectroscopic evidence for differences between enantiomers. *IUCrJ* **2018**, *5*, 6–12. [CrossRef]
266. Bürgia, H.-B.; Macchi, P. Comments on 'Hydrogen bonds in crystalline D-alanine: Diffraction and spectroscopic evidence for differences between enantiomers'. *IUCrJ* **2018**, *5*, 654–657. [CrossRef]
267. Belo, E.A.; Pereira, J.E.; Freire, P.T.; Argyriou, D.N.; Eckert, J.; Bordallo, H.N. Response to comment on 'Hydrogen bonds in crystalline D-alanine: Diffraction and spectroscopic evidence for differences between enantiomers'. *IUCrJ* **2018**, *5*, 658–659. [CrossRef]

268. Koralewski, M.; Baranowski, M.; Ryzner, A. Probing physical invariance between enantiomers: The magnetooptical and refractive properties of the simplest chiral amino acid—Alanine. *J. Mol. Liq.* **2021**, *339*, 117279. [CrossRef]
269. Dubey, M.; Kumar, A.; Dhavale, V.M.; Kurungot, S.; Pandey, D.S. Can enantiomer ligands produce structurally distinct homochiral MOFs? *CrystEngComm* **2015**, *17*, 8202–8206. [CrossRef]
270. Adelberger, E.G.; Gundlach, J.H.; Heckel, B.R.; Hoedl, S.; Schlamminger, S. Torsion balance experiments: A low-energy frontier of particle physics. *Prog. Part. Nucl. Phys.* **2009**, *62*, 102–134. [CrossRef]
271. Ni, W.-T. Searches for the role of spin and polarization in gravity: A five-year update. *Int. J. Mod. Phys. Conf. Ser.* **2016**, *40*, 1660010. [CrossRef]
272. Safronova, M.S.; Budker, D.; DeMille, D.; Kimball, D.F.J.; Derevianko, A.; Clark, C.W. Search for new physics with atoms and molecules. *Rev. Mod. Phys.* **2018**, *90*, 025008. [CrossRef]
273. Qiao, J.; Li, Z.; Zhu, T.; Ji, R.; Li, G.; Zhao, W. Testing parity symmetry of gravity with gravitational waves. *Front. Astron. Space Sci.* **2023**, *9*, 1109086. [CrossRef]
274. Leitner, J.; Okubo, S. Parity, charge conjugation, and time reversal in the gravitational interaction. *Phys. Rev.* **1964**, *136*, B1542–B1546. [CrossRef]
275. Dass, N.D.H. Test for C, P, and T nonconservation in gravitation. *Phys. Rev. Lett.* **1976**, *36*, 393–395. [CrossRef]
276. Anandan, J. Tests of parity and time-reversal noninvariance using neutron Interference. *Phys. Rev. Lett.* **1982**, *48*, 1660–1663. [CrossRef]
277. Hou, L.-S.; Ni, W.-T.; Li, Y.-C.M. Test of cosmic spatial isotropy for polarized electrons using a rotatable torsion balance. *Phys. Rev. Lett.* **2003**, *90*, 201101. [CrossRef]
278. Heckel, B.R.; Cramer, C.E.; Cook, T.S.; Adelberger, E.G.; Schlamminger, S.; Schmidt, U. New *CP*-violation and preferred-frame tests with polarized electrons. *Phys. Rev. Lett.* **2006**, *97*, 021603. [CrossRef]
279. Terrano, W.A.; Adelberger, E.G.; Lee, J.G.; Heckel, B.R. Short-range, spin-dependent interactions of electrons: A probe for exotic pseudo-Goldstone bosons. *Phys. Rev. Lett.* **2015**, *115*, 201801. [CrossRef]
280. Fray, S.; Diez, C.A.; Hänsch, T.W.; Weitz, M. Atomic interferometer with amplitude gratings of light and its applications to atom based tests of the equivalence principle. *Phys. Rev. Lett.* **2004**, *93*, 240404. [CrossRef]
281. Tarallo, M.G.; Mazzoni, T.; Poli, N.; Sutyrin, D.V.; Zhang, X.; Tino, G.M. Test of Einstein equivalence principle for 0-Spin and half-integer-spin atoms: Search for spin-gravity coupling effects. *Phys. Rev. Lett.* **2014**, *113*, 023005. [CrossRef] [PubMed]
282. Rosi, G.; D'Amico, G.; Cacciapuoti, L.; Sorrentino, F.; Prevedelli, M.; Zych, M.; Brukner, Č.; Tino, G.M. Quantum test of the equivalence principle for atoms in coherent superposition of internal energy states. *Nat. Commun.* **2016**, *8*, 15529. [CrossRef]
283. Duan, X.-C.; Deng, X.-B.; Zhou, M.-K.; Zhang, K.; Xu, W.-J.; Xiong, F.; Xu, Y.-Y.; Shao, C.-G.; Luo, J.; Hu, Z.-K. Test of the universality of free fall with atoms in different spin orientations. *Phys. Rev. Lett.* **2016**, *117*, 023001. [CrossRef] [PubMed]
284. Zhang, S.-B.; Ba, Z.-L.; Ning, D.-H.; Zhai, N.-F.; Lu, Z.-T.; Sheng, D. Search for spin-dependent gravitational interactions at earth range. *Phys. Rev. Lett.* **2023**, *130*, 201401. [CrossRef] [PubMed]
285. Touboul, P.; Métris, G.; Rodrigues, M.; André, Y.; Baghi, Q.; Bergé, J.; Boulanger, D.; Bremer, S.; Carle, P.; Chhun, R.; et al. *MICROSCOPE* mission: First results of a space test of the equivalence principle. *Phys. Rev. Lett.* **2017**, *119*, 231101. [CrossRef]
286. Touboul, P.; Métris, G.; Rodrigues, M.; Bergé, J.; Robert, A.; Baghi, Q.; André, Y.; Bedouet, J.; Boulanger, D.; Bremer, S.; et al. *MICROSCOPE* mission: Final results of the test of the equivalence principle. *Phys. Rev. Lett.* **2022**, *129*, 121102. [CrossRef]
287. Zhu, L.; Liu, Q.; Zhao, H.-H.; Gong, Q.-L.; Yang, S.-Q.; Luo, P.; Shao, C.-G.; Wang, Q.-L.; Tu, L.-C.; Luo, J. Test of the equivalence principle with chiral masses using a rotating torsion pendulum. *Phys. Rev. Lett.* **2018**, *121*, 261101. [CrossRef]
288. Bargueño, P.; de Tudela, R.P. Constraining long-range parity violation in gravitation using high resolution spectroscopy of chiral molecules. *Phys. Rev. D* **2008**, *78*, 102004. [CrossRef]
289. Bargueño, P. Chirality and gravitational parity violation. *Chirality* **2015**, *27*, 375–381. [CrossRef] [PubMed]
290. Gaul, K.; Kozlov, M.G.; Isaev, T.A.; Berger, R. Chiral molecules as sensitive probes for direct detection of P-odd cosmic fields. *Phys. Rev. Lett.* **2020**, *125*, 123004. [CrossRef]
291. Gaul, K.; Kozlov, M.G.; Isaev, T.A.; Berger, R. Parity-nonconserving interactions of electrons in chiral molecules with cosmic fields. *Phys. Rev. A* **2020**, *102*, 032816. [CrossRef]
292. Kawagoe, Y.; Fujiki, M.; Nakano, Y. Limonene magic: Noncovalent molecular chirality transfer leading to ambidextrous circularly polarised luminescent *p*-conjugated polymers. *New J. Chem.* **2010**, *34*, 637–647. [CrossRef]
293. Fujiki, M.; Kawagoe, Y.; Nakano, Y.; Nakao, A. Mirror-symmetry-breaking in poly[(9,9-di-*n*-octylfluorenyl-2,7-diyl)-*alt*-biphenyl] (PF8P2) is susceptible to terpene chirality, achiral solvents, and mechanical stirring. *Molecules* **2013**, *18*, 7035–7057. [CrossRef] [PubMed]
294. Franco, M.I.; Turin, L.; Mershin, A.; Skoulakis, E.M.C. Molecular vibration-sensing component in Drosophila melanogaster olfaction. *Proc. Natl. Acad. Sci. USA* **2011**, *108*, 3797–3802. [CrossRef]

295. Gronenberg, W.; Raikhelkar, A.; Abshire, E.; Stevens, J.; Epstein, E.; Loyola, K.; Rauscher, M.; Buchmann, S. Honeybees (Apis mellifera) learn to discriminate the smell of organic compounds from their respective deuterated isotopomers. *Proc. Roy. Soc. B* **2014**, *281*, 20133089. [CrossRef]
296. Turin, L. A Spectroscopic mechanism for primary olfactory reception. *Chem. Sens.* **1996**, *21*, 773–791. [CrossRef] [PubMed]
297. Tirandaz, A.; Ghahramani, F.T.; Shafiee, A. Dissipative vibrational model for chiral recognition in olfaction. *Phys. Rev. E* **2015**, *92*, 032724. [CrossRef]
298. Asogwa, C. Quantum biology: Can we explain olfaction using quantum phenomenon? *arXiv* **2019**, arXiv:1911.02529. [CrossRef]
299. Mokhtari, M.; Khoshbakht, S.; Ziyaei, K.; Akbari, M.E.; Moravveji, S.S. New classifications for quantum bioinformatics: Q-bioinformatics, QCt-bioinformatics, QCg-bioinformatics, and QCr-bioinformatics. *Brief. Bioinform.* **2024**, *25*, bbae074. [CrossRef]
300. Nafie, L.A. *Vibrational Optical Activity—Principles and Applications*; Wiley: Chichester, UK, 2011; ISBN 978-0470032480.
301. Xu, J.; Ramian, G.J.; Galan, J.F.; Savvidis, P.G.; Scopatz, A.M.; Birge, R.R.; Allen, S.J.; Plaxco, K.W. Terahertz circular dichroism spectroscopy: A potential approach to the in situ detection of life's metabolic and genetic machinery. *Astrobiology* **2003**, *3*, 489–504. [CrossRef] [PubMed]
302. Choi, W.J.; Lee, S.H.; Park, B.C.; Kotov, N.A. Terahertz circular dichroism spectroscopy of molecular assemblies, and nanostructures. *J. Am. Chem. Soc.* **2022**, *144*, 22789–22804. [CrossRef] [PubMed]
303. Zhang, T.; Liu, J.; Shi, W.; Fan, F.; Chang, S. Enhancing terahertz circular dichroism spectrum of amino acid chiral enantiomers by all-dielectric metasurface. *Sens. Actuat. A* **2022**, *348*, 114001. [CrossRef]
304. Müller, T.; Wiberg, K.B.; Vaccaro, P.H. Cavity ring-down polarimetry (CRDP): A new scheme for probing circular birefringence and circular dichroism in the gas phase. *J. Phys. Chem. A* **2000**, *104*, 5959–5968. [CrossRef]
305. Bougas, L.; Katsoprinakis, G.E.; von Klitzing, W.; Rakitzis, T.P. Fundamentals of cavity-enhanced polarimetry for parity-nonconserving optical rotation measurements: Application to Xe, Hg, and I. *Phys. Rev. A* **2014**, *89*, 052127. [CrossRef]
306. Prager, M.; Stanislawski, J.; Häusler, W. Inelastic incoherent neutron scattering study of the methyl rotation in various methyl halides. *J. Chem. Phys.* **1987**, *86*, 2563–2575. [CrossRef]
307. Kosower, E.M.; Markovich, G.; Borz, G. Thin-film infrared spectroscopy of acetonitrile. *ChemPhysChem* **2007**, *8*, 2513–2519. [CrossRef] [PubMed]
308. Wong, J.S.; Green, W.H., Jr.; Cheng, C.-k.; Moore, C.B. Coupling of CH stretching and bending vibration of trihalomethanes. *J. Chem. Phys.* **1987**, *86*, 5994–5999. [CrossRef]
309. Nishida, J.; Shigeto, S.; Yabumoto, S.; Hamaguchi, H. Anharmonic coupling of the CH-stretch and CH-bend vibrations of chloroform as studied by near-infrared electroabsorption spectroscopy. *J. Chem. Phys.* **2012**, *137*, 234501. [CrossRef]
310. Nolasco, M.M.; Coimbra, M.M.; Parker, S.F.; Vaz, P.D.; Ribeiro-Claro, P.J. Structural dynamics of chloromethanes through computational spectroscopy: Combining INS and DFT. *Molecules* **2022**, *27*, 7661. [CrossRef] [PubMed]
311. Ratcliffe, C.I.; Waddington, T.C. Internal torsional modes in methyl halogenocarbons studied by inelastic neutron scattering. *J. Chem. Soc. Faraday Trans. 2 Mol. Chem. Phys.* **1976**, *72*, 1821–1839. [CrossRef]
312. Macleod, N.A.; Lawley, K.P.; Donovan, R.J. Internal rotation of the CF_3 group in the (trifluoromethyl)anilines: A zero-kinetic-energy pulsed-field-ionization study. *J. Phys. Chem. A* **2001**, *105*, 5646–5654. [CrossRef]
313. Beckmann, P.A.; Rosenberg, J.; Nordstrom, K.; Mallory, C.W.; Mallory, F.B. CF_3 rotation in 3-(trifluoromethyl)phenanthrene: Solid state ^{19}F and ^{1}H NMR relaxation and Bloch-Wangsness-Redfield theory. *J. Phys. Chem. A* **2006**, *110*, 3947–3953. [CrossRef]
314. Beckmann, P.A.; Rheingold, A.L. ^{1}H and ^{19}F spin-lattice relaxation and CH_3 or CF_3 reorientation in molecular solids containing both H and F atoms. *J. Chem. Phys.* **2016**, *144*, 154308. [CrossRef]
315. Charmet, A.P.; Bizzocchi, L.; Giuliano, B.M.; Caselli, P.; Craig, N.C.; Krasnoshchekov, S. Disentangling the IR spectra of 2,3,3,3-tetrafluoropropene using an ab initio description of vibrational polyads by means of canonical van Vleck perturbation theory. *J. Quant. Spectrosc. Radia. Transfer.* **2019**, *239*, 106656. [CrossRef]
316. Campos-Vallette, M.; Rey-Lafon, M. Molecular structure of the rotational isomers in short chain *n*-perfluoroalkanes. *J. Mol. Struct.* **1984**, *118*, 245–255. [CrossRef]
317. Kim, C.S.; Mowrey, C.; Butler, J.E.; Russell, J.N., Jr. Photochemical attachment of fluorobutyl moieties on a diamond (110)-oriented surface: A multiple internal reflection infrared spectroscopic (MIRIRS) investigation. *J. Phys. Chem. B* **1998**, *102*, 9290–9296. [CrossRef]
318. Jang, S.S.; Blanco, M.; Goddard, W.A., III; Caldwell, G.; Ross, R.B. The source of helicity in perfluorinated *N*-alkanes. *Macromolecules* **2003**, *36*, 5331–5341. [CrossRef]
319. Hasegawa, T.; Shimoaka, T.; Tanaka, Y.; Shioya, N.; Morita, K.; Sonoyama, M.; Amii, H.; Takagi, T.; Kanamori, T. An origin of complicated infrared spectra of perfluoroalkyl compounds involving a normal alkyl group. *Chem. Lett.* **2015**, *44*, 834–836. [CrossRef]
320. Shimoaka, T.; Sonoyama, M.; Amii, H.; Takagi, T.; Kanamori, T.; Hasegawa, T. Raman optical activity on a solid sample: Identification of atropisomers of perfluoroalkyl chains having a helical conformation and no chiral center. *J. Phys. Chem. A* **2019**, *123*, 3985–3991. [CrossRef] [PubMed]

321. Zerbi, G.; Sacchi, M. Dynamics of polymers as structurally disordered systems. Vibrational spectrum and structure of poly(tetrafluoroethylene). *Macromolecules* **1973**, *6*, 692–698. [CrossRef]
322. Starkweather, H.W., Jr.; Ferguson, R.C.; Chase, D.B.; Minor, J.M. Infrared spectra of amorphous and crystalline poly(tetrafluoroethylene). *Macromolecules* **1985**, *18*, 1684–1686. [CrossRef]
323. Dixon, D.A.; Van-Cadedge, F.A. A molecular model for the helicity of polytetrafluoroethylene (Tefloin®). *Int. J. Supercomput. Appl.* **1988**, *2*, 62–81.
324. Mathieu, D.; Defranceschi, M.; Delhalle, J. Ab initio study of the influence of aggregation on the infrared spectrum of acetonitrile. *Int. J. Quantum Chem.* **1993**, *45*, 735–746. [CrossRef]
325. Cavagnat, D.; Lascombe, J.; Lassegues, J.C.; Horsewill, A.J.; Heidemann, A.; Suck, J.B. Neutron and Raman scattering studies of the methyl dynamics in solid toluene and nitromethane. *J. Phys.* **1984**, *45*, 97–105. [CrossRef]
326. Wilmshurst, J.K.; Bernstein, H.J. The infrared and Raman spectra of toluene, toluene-α-d_3, *m*-xylene, and *m*-xylene-$\alpha\alpha'$-d_6. *Can. J. Chem.* **1957**, *35*, 911–925. [CrossRef]
327. Valderrama, A.C.S.; De, G.C.R. Traceability of active compounds of essential oils in antimicrobial food packaging using a chemometric method by ATR-FTIR. *Am. J. Anal. Chem.* **2017**, *8*, 726–741. [CrossRef]
328. Borovkov, V.V.; Hembury, G.A.; Inoue, Y. The origin of solvent-controlled supramolecular chirality switching in a bis(zinc porphyrin) system. *Angew. Chem. Int. Ed.* **2003**, *42*, 5310–5314. [CrossRef]
329. Borovkov, V.V.; Hembury, G.A.; Inoue, Y. Origin, control, and application of supramolecular chirogenesis in bisporphyrin-based systems. *Acc. Chem. Res.* **2004**, *37*, 449–459. [CrossRef]
330. Hembury, G.A.; Borovkov, V.V.; Inoue, Y. Chirality-sensing supramolecular systems. *Chem. Rev.* **2008**, *108*, 1–73. [CrossRef] [PubMed]
331. Borovkov, V.V. Effective supramolecular chirogenesis in ethane-bridged bis-porphyrinoids. *Symmetry* **2010**, *2*, 184–200. [CrossRef]
332. Fujiki, M.; Yoshida, K.; Suzuki, N.; Rahim, N.A.A.; Jalil, J.A. Tempo-spatial chirogenesis. Limonene-induced mirror symmetry breaking of Si–Si bond polymers during aggregation in chiral fluidic media. *J. Photochem. Photobiol. A Chem.* **2016**, *331*, 120–129. [CrossRef]
333. Nakano, Y.; Ichiyanagi, F.; Naito, M.; Yang, Y.; Fujiki, M. Chiroptical generation and inversion during the mirror-symmetry-breaking aggregation of dialkylpolysilanes due to limonene chirality. *Chem. Commun.* **2012**, *48*, 6636–6638. [CrossRef] [PubMed]